A CONTINENTAL SHELF BOTTOM BOUNDARY LAYER MODEL: THE EFFECTS OF WAVES, CURRENTS, AND A MOVEABLE BED

by

SCOTT MICHAEL GLENN

B.S., University of Rochester
(1978)

SUBMITTED IN PARTIAL FULFILLMENT OF THE
REQUIREMENTS FOR THE DEGREE OF

DOCTOR OF SCIENCE

at the

MASSACHUSETTS INSTITUTE OF TECHNOLOGY

and the

WOODS HOLE OCEANOGRAPHIC INSTITUTION

January 1983

Signature of Author_____
Joint Program in Oceanographic Engineering
Massachusetts Institute of Technology
Woods Hole Oceanographic Institution
January 7, 1983

Certified by____
_____
William D. Grant
Thesis Supervisor

Accepted by__
_____
Arthur B. Baggeroer
Chairman, Joint Committee for Oceanographic Engineering

A CONTINENTAL SHELF BOTTOM BOUNDARY LAYER MODEL: THE EFFECTS OF WAVES, CURRENTS, AND A MOVEABLE BED

by

SCOTT MICHAEL GLENN

Submitted to the Massachusetts Institute of Technology -
Woods Hole Oceanographic Institution
Joint Program In Oceanographic Engineering
on January 7, 1983 in partial fulfullment of the
requirements for the Degree of Doctor of Science

ABSTRACT

A simple model for the bottom boundary layer on the continental shelf is presented. The governing equations are developed for a stratified, turbulent Ekman layer in a combined wave and current flow over a moveable sediment bed. An eddy diffusivity closure scheme that includes the effect of suspended sediment, temperature, and salinity induced stratification on the vertical turbulent diffusion of mass and momentum couples the resulting unsteady conservation equations for fluid momentum, fluid mass, and suspended sediment mass. The wave velocity, current velocity, and suspended sediment concentration profiles predicted by the simultaneous solution of the conservation equations require the physical bottom roughness and a sediment reference concentration to be specified as boundary conditions. The physical bottom roughness associated with biologically generated bedforms, wave generated ripples, and near bed sediment transport are calculated as functions of the flow and sediment conditions. Using expressions for the height of sediment transporting layer and the sediment velocity, an expression for the sediment reference concentration is developed by matching laboratory measurements of sediment transport rates in oscillatory flow. The model predicts that the bottom flow field is highly dependent on (1) the nonlinear wave and current interaction, which increases the boundary shear stress and enhances vertical turbulent diffusion, (2) the effect of the boundary shear stress on a moveable sediment bed, which determines the physical bottom roughness and the amount of sediment in suspension, and (3) the effect of stable stratification, which inhibits vertical turbulent transport and couples the flow to the suspended sediment and fluid density profiles. The validity of the theoretical approach is supported by model predictions that are in excellent agreement with high quality data collected during two continental shelf bottom boundary layer experiments for a wide range of flow and bottom conditions.

Thesis Supervisor: Dr. William D. Grant

Title: Associate Scientist
Woods Hole Oceanographic Institution

ACKNOWLEDGEMENTS

Funding for the work resulting in this Thesis has been provided by the American Gas Association (Project No. PR-153-126), the National Science Foundation (Grant No. OCE-8014930), and NOAA-Sea Grant (NA-79AA-D-00101; NA 79AA-D-00102).

Bill Grant conceived and supervised the work presented here. Bill's enthusiasm as a scientist, dedication to students, and enjoyable attitude outside the classroom were strong inspirations in my education. I feel fortunate to have been Bill's student and thank him for the friendship and support I have enjoyed for four and one half years.

Ole Madsen also was an inspiring teacher whose insightful advice and work with Bill Grant have considerably influenced this Thesis. I thank Dave Aubrey for his advice and for the useful field experience gained under his supervision. Bob Beardsley, Earl Hays and Nick Newman also read and commented on this Thesis.

Sandy Williams and Chris Dunn were key figures involved in the CODE-I data acquisition. Dave Cacchione and Dave Drake generously provided the CODE Winter Storm data. Paul Dragos developed many of the computer programs used for the data analysis, suggested and helped implement the numerical solution technique described in Appendix A.1.2, and patiently answered countless computer related questions. Jim Newman, Cindy Pilskaln and Larry Sanford also contributed significantly to the data analysis. Gretchen McManamin diligently typed this Thesis. I thank Gretchen for maintaining her patience, dedication, and good nature despite the trying circumstances. Betsey Pratt kindly drafted the figures on short notice.

I finally wish to thank the members and friends of the WHMC for sponsoring the party and for their continuing friendship.

TABLE OF CONTENTS

Page

APPENDICES

LIST OF FIGURES

LIST OF FIGURES (cont.)

LIST OF FIGURES (cont.)

LIST OF TABLES

LIST OF PRINCIPAL SYMBOLS

a	=	wave amplitude
A_b	=	wave bottom excursion amplitude
C	=	instantaneous concentration, fluid
C_m	=	mean concentration, fluid
C_p	=	periodic concentration, fluid
C'	=	turbulent concentration, fluid
C_n	=	instantaneous concentration, sediment class n
C_{nm}	=	mean concentration, sediment class n
C_{np}	=	periodic concentration, sediment class n
C'_n	=	turbulent concentration, sediment class n
C_{nb}	=	bed concentration, sediment class n
$C_n\ (z_o)$	=	instantaneous reference concentration, sediment class n
$C_{nm}\ (z_o)$	=	mean reference concentration, sediment class n
$C_{np}\ (z_o)$	=	periodic reference concentration, sediment class n
C_T	=	instantaneous sediment concentration in near bed transport layer
C_D	=	drag coefficient
c_w	=	wave phase velocity
d	=	sediment grain diameter

LIST OF PRINCIPAL SYMBOLS (cont.)

F	=	function that modulates linear eddy viscosity profile in the Ekman layer
f	=	Coriolis parameter
f_{cw}	=	combined wave and current friction factor
f'_{cw}	=	combined wave and current skin friction factor
g	=	acceleration of gravity
h	=	water depth
h_T	=	instantaneous height of near bed transport layer
h_{Tm}	=	maximum height of near bed transport layer
i	=	$(-1)^{1/2}$
k	=	wave number
k_x	=	x-component of wave number
k_y	=	y-component of wave number
$\hat{k}$	=	vertical unit vector
k_b	=	physical bottom roughness
k_{bN}	=	Nikuradse roughness
k_{bB}	=	roughness associated with bedforms
k_{bT}	=	roughness associated with near bed transport
k_{bc}	=	apparent bottom roughness
k_h	=	bedform height
k_w	=	bedform cross-stream width

LIST OF PRINCIPAL SYMBOLS (cont.)

k_l	=	bedform streamwise length
k_W	=	cross-stream width of bed associated with bedform
k_L	=	streamwise length of bed associated with bedform
N	=	Brunt-Vaisala frequency
L	=	Monin-Obukov length
L_c	=	Monin-Obukov length, $z > \delta_w$
L_{cw}	=	Monin-Obukov length, $z < \delta_w$
l_c	=	Ekman layer scale height
l_{cw}	=	wave boundary layer scale height
p	=	instantaneous pressure
p_c	=	current pressure
p_w	=	wave pressure
p'	=	turbulent pressure
Q_s	=	total dry weight of sediment transported
q_s	=	average volumetric sediment transport rate
R	=	parameter in stability parameter definition
r	=	regression coefficient
R_f	=	Richardson flux number
s	=	relative sediment density
S_*	=	dimensionless sediment parameter

LIST OF PRINCIPAL SYMBOLS (cont.)

S'_n	=	normalized excess skin friction, sediment class n
T	=	wave period
t	=	time
u	=	x-component of velocity
u_g	=	x-component of geostrophic velocity
u_{100}	=	current speed 1 meter above the bottom
$\vec{u}$	=	instantaneous horizontal velocity
$\vec{u}_c$	=	current horizontal velocity
$\vec{u}_w$	=	wave horizontal velocity
$\vec{u}'$	=	turbulent horizontal velocity
$\vec{u}_a$	=	current velocity used to define boundary shear stress
$\vec{u}_b$	=	maximum wave bottom velocity from linear wave theory
$\vec{u}_n$	=	instantaneous horizontal velocity, sediment class n
$\vec{u}_r$	=	specified reference current velocity
$\vec{u}_*$	=	shear velocity
$\vec{u}_{*c}$	=	shear velocity derived from average boundary shear stress

LIST OF PRINCIPAL SYMBOLS (cont.)

$\vec{u}_{*cw}$	=	shear velocity derived from maximum boundary shear stress
u_T	=	instantaneous particle velocity in near bed transport layer
u_{Tm}	=	maximum particle velocity in near bed transport layer
v	=	y-component of velocity
v_g	=	y-component of geostrophic velocity
V_2	=	parameter in average boundary shear stress definition
w	=	z-component of velocity
w_n	=	z-component of velocity, sediment class n
w_{fn}	=	particle fall velocity, sediment class n
w_w	=	wave vertical velocity
x	=	horizontal Cartesian coordinate
y	=	horizontal Cartesian coordinate
z	=	vertical Cartesian coordinate
z_r	=	height of specified reference current velocity
z/L	=	constant stress layer stability parameter
z_o	=	physical bottom
z_{oc}	=	apparent bottom
α	=	parameter in maximum shear stress definition

LIST OF PRINCIPAL SYMBOLS (cont.)

β	=	constant in nondimensional velocity gradient
γ	=	constant in nondimensional sediment gradient
γ_o	=	reference concentration constant
δ_c	=	current boundary layer height
δ_w	=	wave boundary layer height
δ_D	=	displacement thickness
ζ	=	dimensionless vertical coordinate for the wave boundary layer
ζ_o	=	dimensionless z_o
ζ_c	=	generalized stability parameter, $z > \delta_w$
ζ_{cw}	=	generalized stability parameter, $z < \delta_w$
η	=	ripple height
θ	=	wave phase angle
θ_g	=	geostrophic velocity turning angle
κ	=	von Karman's constant
λ	=	ripple length
λ_w	=	surface wave length
ν	=	kinematic viscosity
ν_t	=	neutral eddy viscosity
ν_{tc}	=	neutral eddy viscosity, $z > \delta_w$
ν_{tcw}	=	neutral eddy viscosity, $z < \delta_w$
ν_{tm}	=	stratified eddy diffusivity of momentum

LIST OF PRINCIPAL SYMBOLS (cont.)

ν_{ts}	=	stratified eddy diffusivity of sediment mass
ν_{tf}	=	stratified eddy diffusivity of fluid mass
ξ	=	dimensionless vertical coordinate for the Ekman layer
ξ_c	=	dimensionless height of Ekman layer
ξ_w	=	dimensionless height of wave boundary layer
ρ	=	fluid density
ρ_b	=	bottom fluid density
ρ_m	=	mean fluid density
ρ_p	=	periodic fluid density
ρ'	=	turbulent fluid density
ρ_s	=	sediment density
ρ_T	=	total density of fluid-sediment suspension
$\overline{\rho_T}$	=	Reynolds averaged total density
ρ'_T	=	turbulent total density
$\vec{\tau}$	=	shear stress
$\vec{\tau}_b$	=	instantaneous boundary shear stress
$\vec{\tau}_c$	=	average boundary shear stress (accounting for direction)
$\vec{\tau}_{cw}$	=	maximum boundary shear stress
$\vec{\tau}_b'$	=	instantaneous skin friction
$\vec{\tau}'_{bm}$	=	maximum skin friction

LIST OF PRINCIPAL SYMBOLS (cont.)

ϕ	=	dimensionless sediment transport function
ϕ_c	=	angle between $\vec{u}_a$ and $\vec{u}_b$
$\bar{\phi}_c$	=	angle between $\vec{u}_r$ and $\vec{u}_b$ for near bottom model, $0^\circ \leq \bar{\phi}_c \leq 90^\circ$
ϕ_r	=	angle between $\vec{u}_r$ and $\vec{u}_b$ for Ekman layer model, $-90^\circ \leq \phi_r \leq 90^\circ$
ϕ_m	=	nondimensional velocity gradient
ϕ_s	=	nondimensional sediment gradient
χ	=	logarithmic vertical coordinate in Ekman layer
ψ_B	=	breakoff Shields parameter
ψ_c	=	critical Shields parameter
ψ'	=	instantaneous Shields parameter based on skin friction
ψ'_m	=	maximum Shields parameter based on skin friction
$\vec{\Omega}_H$	=	horizontal component of planetary angular velocity
Ω_v	=	vertical component of planetary angular velocity
ω	=	radian wave frequency

1. INTRODUCTION

A quantitative description of the bottom boundary layer on the continental shelf is necessary to understand a wide range of coastal oceanographic problems. The design of submarine structures, such as pipelines, requires detailed knowledge of the near bottom flow field to estimate realistically the resulting hydrodynamic forces on the structures. Calculation of sediment transport rates require flow field descriptions that are most accurate near the bottom where sediment concentrations are highest. Prediction of shelf circulation patterns require specification of the magnitude, direction, and spatial variability of the boundary shear stress associated with the near bottom flow field. Estimates of wave attenuation rates due to bottom friction requires the instantaneous boundary shear stress to be known. An accurate model of the bottom boundary layer on the continental shelf will significantly improve our ability to understand these problems.

A simple model for the bottom boundary layer on the continental shelf is developed here. The model is designed to predict the vertical structure of the bottom boundary layer at a point on the continental shelf from a minimum number of input parameters. Important physical processes influencing the bottom boundary layer structure include: (1) the simultaneous presence of both surface waves and low frequency currents, (2) moveable bed effects (ripple formation, near bed sediment transport, and suspended sediment transport), (3) the stabilizing or destabilizing effect of bioturbation, (4) self induced stratification of the flow field by suspended sediment, (5) planetary rotation, (6)

temperature and salinity stratification, (7) internal waves, and (8) the effect of bottom topography. With the exception of internal waves and bottom topography, which are often second order or site specific problems, the above physical processes are incorporated into a continental shelf, bottom boundary layer model. Given the wave conditions (period, amplitude, direction, and water depth), the current conditions (current speed and direction at a known height above the bottom), bottom conditions (type of sediment, type of bedforms), and the temperature and salinity profiles, the bottom boundary layer model can be used to calculate vertical velocity profiles for the wave and the current, vertical concentration profiles of suspended sediment, suspended sediment transport rates, and the boundary shear stress.

Development of the bottom boundary layer model proceeds as follows. A physical description of the important processes affecting the bottom boundary layer is presented in Chapter 2. In Chapter 3, a theoretical model for the near bottom flow in the absence of stratification is discussed. The Grant and Madsen (1979) combined wave and current model and the Grant and Madsen (1982) moveable bed roughness in oscillatory flow model are reviewed. A theoretical model for the near bottom flow that includes suspended sediment induced stratification is developed in Chapter 4. The effect of stratification is incorporated in the Grant and Madsen (1979) combined wave and current model and a model is developed to predict sediment reference concentrations. In Chapter 5, a theoretical model for the full Ekman layer is developed. The near bottom, combined wave and current model is extended by including the effects of planetary

rotation and stratification associated with suspended sediment, temperature and salinity. Finally, velocity profiles predicted by the near bottom model are compared in Chapter 6 to near bottom velocity profiles measured during two bottom boundary layer experiments on the continental shelf.

2. PHYSICAL MODEL FOR THE BOTTOM BOUNDARY LAYER ON THE CONTINENTAL SHELF

The major physical processes affecting the bottom boundary layer will be discussed in this chapter. The processes involved are the interaction of a wave boundary layer and a current boundary layer, the physical bottom roughness associated with a bioturbated moveable bed, stratification of the near bottom flow field by suspended sediment, and stratification of the outer Ekman layer by temperature and salinity. In subsequent chapters, mathematical models for these physical processes will be developed.

2.1 Wave and Current Interaction

The near bottom flow field on the continental shelf typically has velocity components associated with surface gravity waves and with tidal, wind generated, or density driven, low frequency currents. Because of the contrasting time and length scales associated with each component, two distinct boundary layers develop, one associated with the current and one associated with the wave. The current boundary layer, or Ekman layer, is relatively steady with a thickness limited by water depth or Ekman layer height. For fully

rough turbulent flow, the current boundary layer can be divided into an inner, near bottom, constant stress or logarithmic region and an outer log deficit region. Planetary rotation causes the current velocity vector in the Ekman layer to rotate in a clockwise direction with distance from the bottom in the Northern Hemisphere. Ekman turning of the velocity vector, however, is significant only in the outer log deficit region. Above the current boundary layer, the turbulent shear stress associated with the current is negligible. In this geostrophic core region, the current is adequately described by inviscid theory.

Nested within the current boundary layer is a wave boundary layer. In comparison, the wave boundary layer is oscillatory with a typical thickness of 2 to 20 centimeters. For fully rough turbulent flow, the wave boundary layer also can be divided into an inner constant stress region and an outer log deficit region. Above the wave boundary layer, the turbulent shear stress associated with the wave is negligible. The wave above the wave boundary layer is also adequately described by inviscid theory. A typical bottom boundary layer on the continental shelf is illustrated in Figure 2.1.

Maximum near bottom wave velocities on the continental shelf are typically the same order of magnitude or greater than near bottom current velocities. The small scale of the wave boundary layer compared to the current boundary layer causes the boundary shear stress associated with the wave to be much greater than that associated with the current. Boundary shear stress, however, is a nonlinear function of the instantaneous wave plus current velocity,

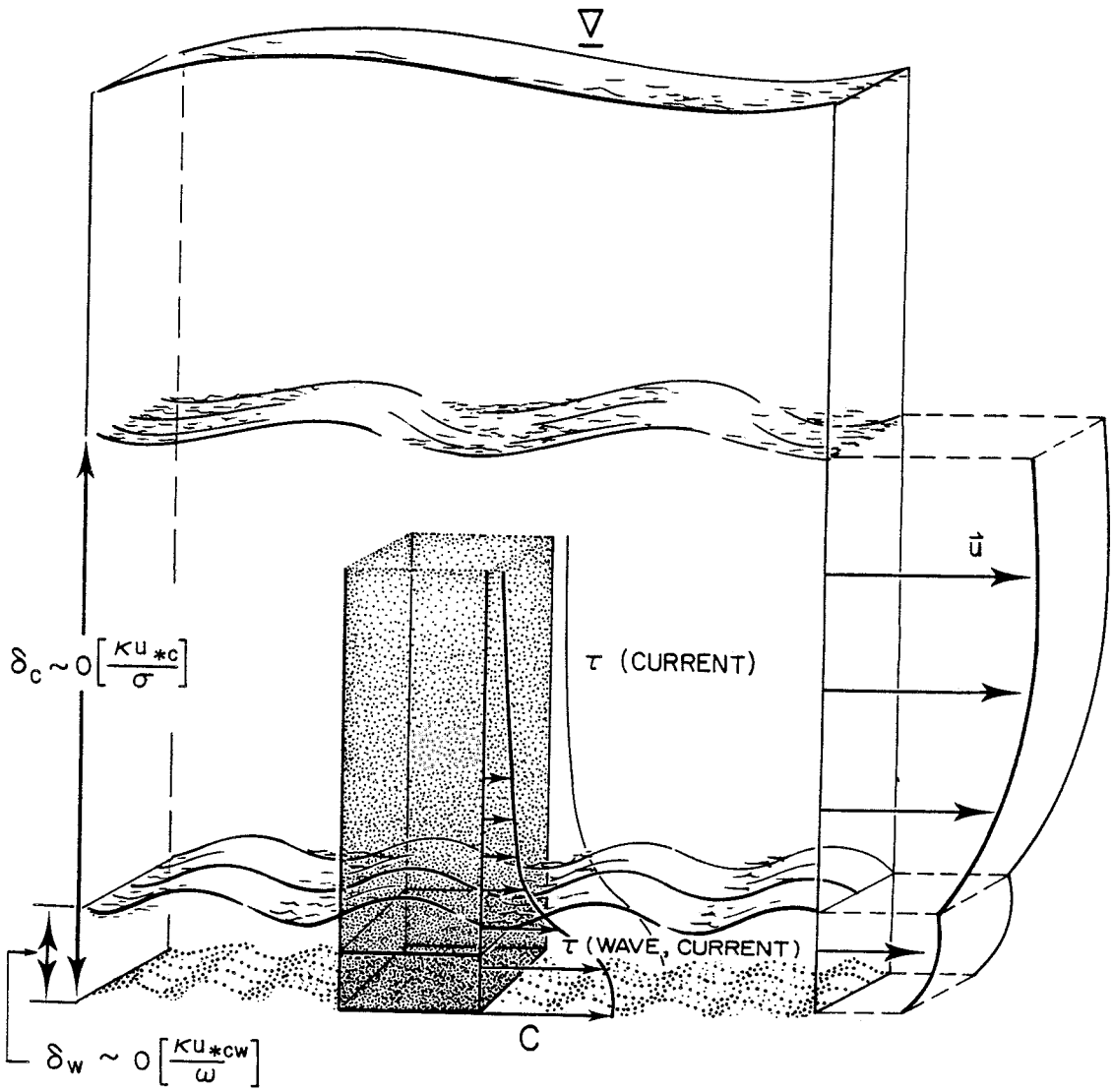

FIGURE 2.1

Skematic of the continental shelf bottom boundary layer illustrating the nested wave and current boundary layer structure.

which varies in magnitude and direction over a wave period. The wave and current therefore interact to generate a shear stress that also varies in magnitude and direction and is different from the shear stress associated with each component individually. For example, the constant stress experienced by the time average current in the inner region of the current boundary layer must be the time average of the instantaneous boundary shear stress, which is enhanced by the presence of the waves.

In the constant stress region for the current, a semi-logarithmic velocity profile is generated in the absence of stratification by turbulent diffusion of low momentum fluid away from the boundary. Above the wave boundary layer, in the potential flow region for the wave, turbulent diffusion is associated with the time average current only. Within the wave boundary layer, however, turbulent diffusion is associated with the combined wave and current flow. Because the diffusion of low momentum fluid within the wave boundary layer is enhanced by the wave, current velocities in this region are reduced. The resulting reduction in the current shear within the wave boundary layer is similar to that caused by enhanced turbulent diffusion in the boundary layers behind upstream bumps. Just as dissipation is increased behind stream bumps, the increased dissipation in the wave boundary layer causes the current above the wave boundary layer to appear to feel a much larger bottom roughness than physically exists.

2.2 Physical Bottom Roughness

The boundary shear stress in a fully rough turbulent flow also depends on the physical bottom roughness; a larger bottom roughness results in a larger shear stress. Because the moveable sediment bed commonly found on the continental shelf can be modified by marine organisms or changing flow conditions, the physical bottom roughness is highly dependent on the sediment characteristics and the boundary shear stress. The physical bottom roughness of a moveable bed is often partitioned into components associated with three physical processes; (1) drag on sediment grains in the bed, (2) form drag on bedforms, and (3) drag on sediment grains in the near bed transport layer. Since the shear stress associated with the wave is usually much greater than that associated with the current, moveable bed effects are expected to be wave dominated.

If the boundary shear stress is below that required to initiate sediment motion, the constant bottom roughness is associated with the sediment grains in the bed and with existing bedforms. Existing bedforms could be ripples formed during previous high flow events or bedforms generated by benthic organisms. If the boundary shear stress is increased above that required to initiate sediment motion, the bottom roughness becomes a function of the boundary shear stress and is no longer a constant. Pre-existing bedforms begin to erode as near bed sediment transport begins. As the boundary shear stress continues to increase, near bed sediment transport also increases. If the sediment is sand or silt, a flat bed is unstable and ripples

will form. Ripples remain in equilibrium with the flow as the boundary shear stress increases until a breakoff point is reached. As the boundary shear stress increases past the breakoff point, ripple heights decay until the bed is flat but covered by an intense near bed sediment transport layer. When sediment transport occurs, the bottom roughness is associated with all three components; sediment grains, bedforms, and near bed transport. The bedform component, which is important for low flow situations when there is little near bed transport, is found to depend on bedform geometry. The transport component, which is important for high flow situations when bedforms have been washed out, is found to depend on the height of the near bed transport layer.

2.3 Stratification

The bottom boundary layer on the continental shelf can also be affected by stable stratification. Because stable stratification inhibits the vertical turbulent transport of mass and momentum, less low momentum fluid is transported up through the water column in a stratified flow. A stratified flow will experience an increased shear in the velocity profile compared to a neutral flow with the same boundary shear stress. In the bottom boundary layer stratification can be caused by vertical gradients of suspended sediment, temperature, or salinity.

2.3.1 Suspended sediment induced stratification

Self induced stratification of the near bottom flow field can

occur when the boundary shear stress is large enough to suspend significant amounts of sediment in the water column. Since the boundary shear stress associated with the wave is greater than that associated with the current, waves are more effective at suspending sediment than currents. The effect of suspended sediment induced stratification therefore is expected to be greater for a combined wave and current flow than for a pure current flow.

In the bottom boundary layer, the upward turbulent diffusion of sediment is balanced by the sediment's tendency to fall out of suspension, resulting in a concentration profile that decreases with distance from the bottom. The vertical density gradient caused by the decreasing sediment concentration can stably stratify the flow field if the sediment has the appropriate fall velocity. If the fall velocity is too large, very little sediment will be suspended and the resulting density gradient will be insignificant. If the fall velocity is too small, large amounts of sediment will be mixed uniformly throughout the water column, again resulting in an insignificant density gradient. For the flow to be stratified by suspended sediment, the sediment fall velocity must be in an intermediate range that causes large density gradients.

For stratification to influence vertical turbulent diffusion, there must be a significant density difference over the length scale of the momentum transporting eddies. This suggests that suspended sediment induced stratification will not affect the entire bottom boundary layer. In the constant stress layer, the momentum

transporting eddies scale with distance from the bottom. Close to the bottom, the momentum transporting eddies are so small that the density differences over the eddy length scale are also small. Away from the bottom the eddy length scale is large, but there is so little sediment in suspension that again there is little density difference. Stratification induced by suspended sediment therefore is only expected to be significant in some regions of the bottom boundary layer.

2.3.2 Temperature and salinity induced stratification

Vertical turbulent transport in the bottom boundary layer can also be inhibited by stratification due to temperature and salinity gradients. Unlike the atmosphere, temperature and salinity gradients are not maintained by input from the bottom, but are caused by advection or surface input. High turbulence levels and mixing rates near the bottom will tend to smooth out any density differences due to temperature or salinity. Typical temperature and salinity profiles on the continental shelf consist of a bottom mixed layer of uniform density with significant density gradients above. If the Ekman layer height exceeds the bottom mixed layer height, temperature and salinity stratification will tend to cap the Ekman layer, inhibiting its vertical growth. In contrast to suspended sediment induced stratification, which is important to the near bottom flow, temperature and salinity stratification is usually expected to be most important in the upper Ekman layer.

3. THEORETICAL MODEL FOR A NEUTRAL NEAR BOTTOM FLOW IN COMBINED WAVES AND CURRENTS OVER A MOVEABLE BED

From the physical model presented in the preceding chapter, it is clear that a bottom boundary layer model must account for the effects of combined waves and currents over a bioturbated moveable bed in a possibly stratified Ekman layer. Existing theoretical models address several aspects of this problem. Grant and Madsen (1979) and Smith (1977) have developed a combined wave and current model for the near bottom flow that neglects the effect of stratification. Grant and Madsen (1982) have modeled the roughness of a moveable bed in oscillatory flow. Rhoads et al. (1978), Nowell et al (1981) and Grant et al. (1982) have examined the effect of bioturbation on the initiation of sediment motion. Grant and Glenn (in press) have modeled the effect of biologically induced bedforms on the near bottom flow. Smith and McLean (1977; 1977) have included the effect of suspended sediment induced stratification in a pure current model. Long (1981) developed a temperature and salinity stratification correction that applies throughout a pure current Ekman layer. Elements of these models will be used in the bottom boundary layer model developed here.

In this chapter, a model for the near bottom flow field on the continental shelf in the absence of stratification is described. The Grant and Madsen (1979) combined wave and current model, which is the fundamental component of the bottom boundary layer model, is reviewed in Section 3.1. A boundary condition required by the combined wave and current model is that the velocity is zero at a height determined by the

physical bottom roughness. A review of the Grant and Madsen (1982) moveable bed roughness in oscillatory flow model is included in the discussion of the physical bottom roughness model in Section 3.2. Together, these models can be used to calculate near bottom velocity profiles for the wave and the current when stratification is negligible.

3.1 Neutral Near Bottom Model

Grant and Madsen (1979) have developed a model that predicts the near bottom flow field over a rough bottom in an unstratified fluid due to the combined presence of a wave and a current at arbitrary angles. This model is reviewed here. The governing equations for the problem are set up, a turbulent closure scheme is described, and the resulting equations are solved for the wave and the current velocity profiles.

3.1.1 Governing equations

The equation governing the near bottom flow when suspended sediment transport is negligible is the usual horizontal conservation of fluid momentum equation

$$\frac{D\vec{u}}{Dt} + 2\,\Omega_V\,\hat{k} \times \vec{u} + 2\,\vec{\Omega}_H \times w\,\hat{k} = -\frac{1}{\rho}\vec{\nabla} p + \nu\left(\vec{\nabla}^2\vec{u} + \frac{\partial^2\vec{u}}{\partial z^2}\right) \tag{3.1}$$

where x, y, and z are the components of a Cartesian coordinate system with z measured positive upward from the bottom, t is time, $\vec{u} = (u,v)$ is the horizontal fluid velocity vector with components u and v, w is the vertical fluid velocity, $\vec{\Omega}_H$ and Ω_V are the horizontal and

vertical components of the Earth's angular velocity, $\hat{k}$ is the vertical unit vector, ρ is the fluid density, p is the pressure, ν is the kinematic viscosity, and $\vec{\nabla} = (\partial/\partial x, \partial/\partial y)$ is the horizontal vector operator. For convenience, only horizontal components are written in vector form.

Because the turbulent flow considered here is due to a combined wave and current, the fluid velocity and pressure are partitioned into current, wave, and turbulent contributions

$$\begin{aligned} \vec{u} &= \vec{u}_c + \vec{u}_w + \vec{u}' \\ w &= w_c + w_w + w' \\ p &= p_c + p_w + p' \end{aligned} \tag{3.2}$$

where the subscript c denotes the current, the subscript w denotes the wave, and the prime denotes the turbulent fluctuations. After substituting the partitioned variables for the velocity and pressure, the governing equations are Reynolds averaged over a time that is short compared to the wave period, but long compared to the turbulent time scales. The governing equations then are simplified using the following scaling arguments. The current is assumed to be quasi-steady and horizontally homogeneous. Current and wave velocities are assumed to be much less than the wave phase speed so that convective accelerations can be neglected compared to the local acceleration of the wave. Because the wave frequency is much greater than the

Coriolis parameter, Coriolis acceleration of the wave also can be neglected compared to the local wave acceleration. Viscous stresses can be neglected compared to turbulent Reynolds stresses since rough turbulent flow is expected. Since horizontal length scales are much greater than vertical length scales, horizontal derivatives of the Reynolds stresses are neglected compared to vertical derivatives. The resulting equation governing the horizontal near bottom flow is

$$\frac{\partial \vec{u}_w}{\partial t} + f\,\hat{k} \times \vec{u}_c = -\frac{1}{\rho}\vec{\nabla}(p_c + p_w) + \frac{\partial}{\partial z}\left(-\overline{\vec{u}'w'}\right) \tag{3.3}$$

where $f = 2\,\Omega_v$ is the Coriolis parameter and the overbar represents the Reynolds average.

3.1.2 Turbulent closure scheme

To solve equation (3.3), Grant and Madsen (1979) adopt a turbulent closure scheme based on an eddy viscosity model. The model assumes that the vertical turbulent momentum flux can be written as a turbulent eddy viscosity multiplied by the vertical gradient of the Reynolds averaged horizontal velocity

$$-\overline{\vec{u}'w'} = \nu_t \frac{\partial}{\partial z}(\vec{u}_c + \vec{u}_w) \tag{3.4}$$

where ν_t is the turbulent eddy viscosity. To model correctly the flow in both the wave and the current boundary layer, the eddy viscosity model must reflect the momentum transporting properties of each boundary layer. In the constant stress region of the bottom

boundary layer, the proper length scale for the momentum transporting eddies is the distance from the bottom. Grant and Madsen (1979) selected an eddy viscosity that varies linearly with z,

$$\nu_t = \kappa |\vec{u}_*| z \tag{3.5}$$

where $\kappa = 0.4$ is von Karman's constant and $|\vec{u}_*|$ is the magnitude of the characteristic shear velocity defined as

$$|\vec{u}_*| = (|\vec{\tau}|/\rho)^{1/2} \tag{3.6}$$

where $|\vec{\tau}|$ is the magnitude of the characteristic shear stress. The characteristic shear velocity is then required to represent the velocity scale of the momentum transporting eddies in each boundary layer. Characteristic shear velocities can be found by defining characteristic shear stresses for each boundary layer using the expression for the instantaneous boundary shear stress.

Grant and Madsen (1979) use a quadratic drag law to define the instantaneous boundary shear stress $\vec{\tau}_b$ for a combined wave and current flow as

$$\vec{\tau}_b = \frac{1}{2} \rho f_{cw} (u^2 + v^2) \left[\frac{u}{(u^2 + v^2)^{1/2}}, \frac{v}{(u^2 + v^2)^{1/2}}\right] \tag{3.7}$$

where u and v are the x and y components of a combined wave and current reference velocity and f_{cw} is the combined wave and current friction factor, which will be defined later. Assuming the x-axis is aligned with the wave, u and v are defined as

$$u = |\vec{u}_b| \left(\frac{|\vec{u}_a|}{|\vec{u}_b|} \cos \phi_c + \sin \theta \right) = |\vec{u}_b| \; g_x \tag{3.8}$$

and

$$v = |\vec{u}_b| \left(\frac{|\vec{u}_a|}{|\vec{u}_b|} \sin \phi_c \right) = |\vec{u}_b| \; g_y \tag{3.9}$$

where $|\vec{u}_b|$ is the magnitude of the maximum bottom wave velocity given by linear wave theory, $|\vec{u}_a|$ is the magnitude of an unknown current reference velocity, ϕ_c is the angle between $\vec{u}_a$ and $\vec{u}_b$, $\theta = \omega t$ is the wave phase angle, and ω is the radian wave frequency. The ratio $|\vec{u}_a| / |\vec{u}_b|$ expresses the relative significance of the current in the definition of the shear stress. For the usual case on the continental shelf of small currents and large waves, the relative magnitude of the current $|\vec{u}_a| / |\vec{u}_b|$ is small. Using the expressions for u and v, the instantaneous boundary shear stress can be rewritten as

$$\vec{\tau}_b = \frac{1}{2} \rho \, f_{cw} \, |\vec{u}_b|^2 \, [(g_x^4 + g_x^2 \, g_y^2)^{1/2}, \; (g_x^2 \, g_y^2 + g_y^4)^{1/2}] \tag{3.10}$$

reflecting the dominating influence of the wave.

Above the wave boundary layer, the turbulent shear stress is associated with the time average current only. The characteristic shear stress in this region is taken to be the time average of the instantaneous boundary shear stress defined as

$$\vec{\tau}_c = \frac{1}{2} \rho \, f_{cw} \, |\vec{u}_b|^2 \, [V_{2x}, \; V_{2y}] \tag{3.11}$$

where

$$V_{2x} = \frac{1}{2\pi}\left[\int_{-\theta_*}^{\pi+\theta_*} (g_x^4 + g_x^2 g_y^2)^{1/2}\, d\theta - \int_{\pi+\theta_*}^{2\pi-\theta_*} (g_x^4 + g_x^2 g_y^2)^{1/2} d\theta\right] \tag{3.12}$$

and

$$V_{2y} = \frac{1}{2\pi}\int_0^{2\pi} (g_x^2 g_y^2 + g_y^4)^{1/2}\, d\theta \tag{3.13}$$

The time average of the x-component accounts for direction since the shear stress is positive when $-\theta_* \leq \theta \leq \pi + \theta_*$ and negative when $\pi + \theta_* \leq \theta \leq 2\pi - \theta_*$ where θ_* is defined as

$$\theta_* = \sin^{-1}\left[(|\vec{u}_a|/|\vec{u}_b|)\cos\phi_c\right] \quad \text{for} \quad (|\vec{u}_a|/|\vec{u}_b|)\cos\phi_c \leq 1$$

$$\theta_* = \pi/2 \quad \text{for} \quad (|\vec{u}_a|/|\vec{u}_b|)\cos\phi_c \geq 1 \tag{3.14}$$

The time average shear stress $\vec{\tau}_c$ acts in the same direction as the near bottom current and the vertical gradient of $\vec{\tau}_c$ acts to balance the forces driving the current. Because the x-component keeps track of direction, $\vec{\tau}_c$ for a pure wave is zero. Equation (3.11) can be used to find the magnitude of $\vec{\tau}_c$

$$|\vec{\tau}_c| = \frac{1}{2}\rho\, f_{cw}\, |\vec{u}_b|^2\, V_2 \tag{3.15}$$

where

$$V_2^2 = V_{2x}^2 + V_{2y}^2 \tag{3.16}$$

and the direction of $\vec{\tau}_c$

$$\overline{\phi}_c = \tan^{-1}(V_{2y}/V_{2x}) \tag{3.17}$$

$\overline{\phi}_c$ and V_2 are plotted as functions of $|\vec{u}_a|/|\vec{u}_b|$ and ϕ_c in Figure 3.1 and Figure 3.2. For small currents relative to the waves (small $|\vec{u}_a|/|\vec{u}_b|$), V_2 and $\overline{\phi}_c$ can be approximated as

$$V_2 = \frac{2}{\pi} \left(|\vec{u}_a|/|\vec{u}_b|\right) [4 - 3 \sin^2 \phi_c]^{1/2} \tag{3.18}$$

and

$$\tan \overline{\phi}_c = \frac{1}{2} \tan \phi_c \tag{3.19}$$

Using (3.6) and (3.15), the characteristic shear velocity above the wave boundary layer can be written

$$|\vec{u}_{*c}| = \left(\frac{1}{2} f_{cw} V_2\right)^{1/2} |\vec{u}_b| \tag{3.20}$$

The direction of $\vec{u}_{*c}$, by definition, is the direction of $\vec{\tau}_c$.

Within the wave boundary layer, the turbulent shear stress is associated with the combined wave and current flow, which varies in time. A characteristic shear stress that also varies in time results in a governing equation that has no simple analytical solution. To avoid underestimating the eddy viscosity during the high velocity portion of the wave cycle when most of the turbulence is generated, the maximum boundary shear stress is chosen as the time invariant characteristic shear stress for the wave boundary layer. The magnitude of the maximum boundary shear stress is defined as

$$|\vec{\tau}_{cw}| = \frac{1}{2} \rho f_{cw} |\vec{u}_b|^2 \alpha \tag{3.21}$$

where

$$\alpha = 1 + 2 \left(|\vec{u}_a|/|\vec{u}_b|\right) \cos \phi_c + \left(|\vec{u}_a|/|\vec{u}_b|\right)^2 \tag{3.22}$$

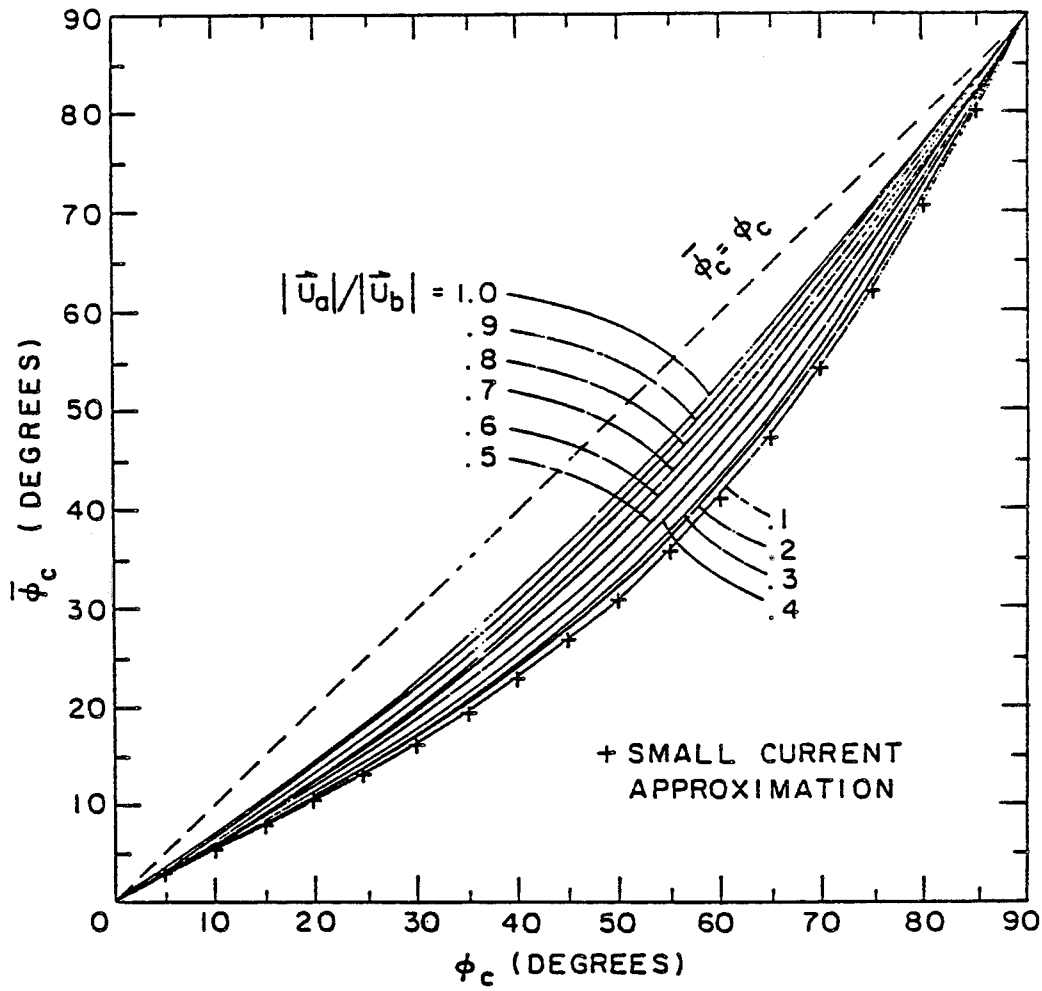

FIGURE 3.1
Direction ϕ_c of the time average boundary shear stress given by (3.17) and by the small current approximation (3.19) as a function of the reference current relative magnitude $|\vec{u}_a| / |\vec{u}_b|$ and direction ϕ_c. Grant and Madsen (1979).

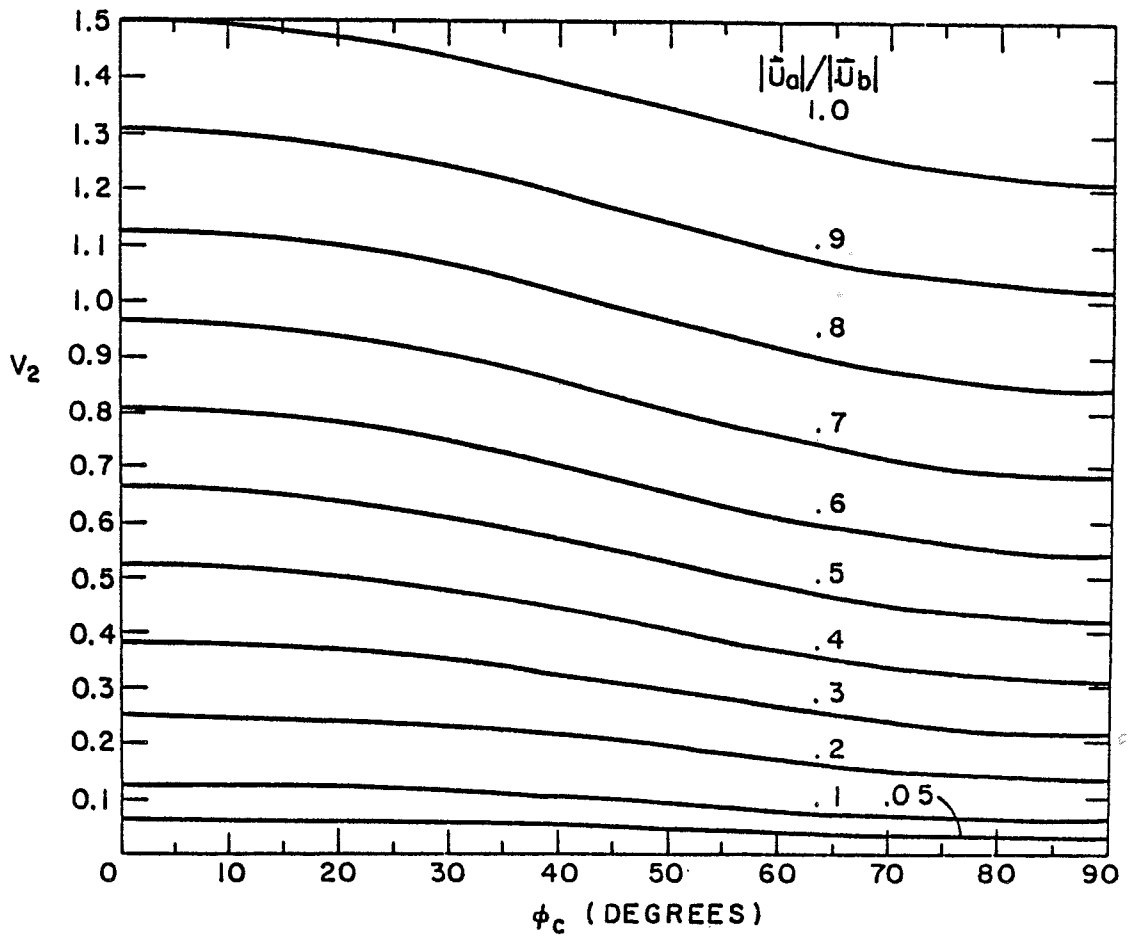

FIGURE 3.2

Parameter V_2 in (3.16) as a function of the reference current relative magnitude $|\vec{u}_a| / |\vec{u}_b|$ and direction ϕ_c. Grant and Madsen (1979).

Using (3.6) and (3.21), the magnitude of the characteristic shear velocity within the wave boundary layer can be written

$$|\vec{u}_{*cw}| = (\frac{1}{2} f_{cw} \alpha)^{1/2} |\vec{u}_b| \tag{3.23}$$

With these definitions of the characteristic shear velocities $|\vec{u}_{*c}|$ and $|\vec{u}_{*cw}|$, Grant and Madsen (1979) adopt the following expressions for the eddy viscosity profile

$$\nu_{tc} = \kappa |\vec{u}_{*c}| z \qquad z > \delta_w \tag{3.24}$$

and

$$\nu_{tcw} = \kappa |\vec{u}_{*cw}| z \qquad z < \delta_w \tag{3.25}$$

where δ_w is the height of the wave boundary layer. It should be noted that this eddy viscosity profile is discontinuous at $z = \delta_w$. The solution for a reasonable continuous eddy viscosity profile is discussed in Appendix II. Substituting the eddy viscosity model (3.4) for the momentum flux in the governing equation (3.3), the resulting equation for the combined wave and current flow is

$$\frac{\partial \vec{u}_w}{\partial t} + f \hat{k} \times \vec{u}_c = -\frac{1}{\rho} \vec{\nabla} (p_c + p_w) + \frac{\partial}{\partial z} [\nu_t \frac{\partial}{\partial z} (\vec{u}_c + \vec{u}_w)] \tag{3.26}$$

where the appropriate eddy viscosity is used for each boundary layer. Because the assumed eddy viscosity profile is time invariant, (3.26) can be separated into an equation for the wave and an equation for the current by averaging over a wave period.

3.1.3 Solution for the wave

Averaging equation (3.26) over a wave period and subtracting the result from the original equation yields the following equation for

the wave

$$\frac{\partial \vec{u}_w}{\partial t} = -\frac{1}{\rho}\vec{\nabla} p_w + \frac{\partial}{\partial z}\left(\nu_t \frac{\partial \vec{u}_w}{\partial z}\right) \tag{3.27}$$

Since the turbulent momentum flux associated with the wave is small above the wave boundary layer, the equation for the wave becomes

$$\frac{\partial \vec{u}_w}{\partial t} = -\frac{1}{\rho}\vec{\nabla} p_w \qquad z > \delta_w \tag{3.28}$$

Equation (3.28) is just the linearized Euler equation which is satisfied by the familiar linear wave theory solution. The horizontal wave velocity above the wave boundary layer therefore can be written as

$$\vec{u}_w = -\vec{u}_b \cosh kz \sin(k_x x + k_y y - \omega t) \qquad z > \delta_w \tag{3.29}$$

where $k = (k_x^2 + k_y^2)^{1/2}$ is the wave number with components k_x and k_y. Equation (3.29) states that the horizontal wave velocity above the wave boundary layer is equal to the maximum potential flow bottom velocity $\vec{u}_b$ multiplied by a vertical growth term and a periodic term. Evaluating (3.29) at $z = \delta_w$ and $x = y = 0$ gives the velocity at the top of the wave boundary layer as

$$\vec{u}_w \sim \vec{u}_b \sin\omega t \qquad z = \delta_w \tag{3.30}$$

since $\cosh k\delta_w \sim 1$. Because $|\vec{u}_{*c}|$ is expected to be the same order of magnitude as the wave and the current velocities,

substitution of equations (3.24) and (3.29) into (3.27) shows that neglect of the stress divergence term above the wave boundary layer is equivalent to the linearization assumption that fluid velocities are much less than the wave phase speed.

Within the wave boundary layer, the wave velocity is governed by (3.27) with the eddy viscosity given by (3.25)

$$\frac{\partial \vec{u}_w}{\partial t} = -\frac{1}{\rho} \vec{\nabla} p_w + \frac{\partial}{\partial z} \left(\kappa \left| \vec{u}_{*cw} \right| z \frac{\partial \vec{u}_w}{\partial z} \right) \qquad z < \delta_w \tag{3.31}$$

The current influences the wave through the eddy viscosity which depends on the maximum combined wave and current shear velocity. As z approaches the top of the wave boundary layer, the divergence of the stress approaches zero and equation (3.31) approaches

$$\frac{\partial \vec{u}_w}{\partial t} = -\frac{1}{\rho} \vec{\nabla} p_w \tag{3.32}$$

where $\vec{u}_w$ is given by (3.30). Introducing complex notation and assuming that the physical solution corresponds to the imaginary part, equation (3.30) can be written as

$$\vec{u}_{w\infty} = \vec{u}_b \, e^{i\omega t} \tag{3.33}$$

where $i = (-1)^{1/2}$. Making the usual boundary layer assumption that the pressure gradient does not vary over the depth of the boundary layer, equation (3.32) can be used to eliminate the pressure gradient from equation (3.31). Defining the velocity deficit as

$$\vec{w} \, e^{i\omega t} = \vec{u}_w - \vec{u}_{w\infty} \tag{3.34}$$

equation (3.31) can be written as

$$\frac{\partial}{\partial z}\left(\frac{\kappa |\vec{u}_{*cw}|}{\omega} z \frac{\partial \vec{w}}{\partial z}\right) - i \vec{w} = 0 \tag{3.35}$$

Defining the vertical length scale of the wave boundary layer as

$$l_{cw} = \frac{\kappa |\vec{u}_{*cw}|}{\omega} \tag{3.36}$$

and introducing the nondimensional vertical coordinate

$$\zeta = z/l_{cw} \tag{3.37}$$

equation (3.35) can be rewritten as

$$\frac{\partial}{\partial \zeta}\left(\zeta \frac{\partial \vec{w}}{\partial \zeta}\right) - i \vec{w} = 0 \tag{3.38}$$

The boundary conditions on (3.38) are that the velocity deficit approaches zero as z approaches the top of the wave boundary layer

$$\vec{w} \to 0 \qquad \text{as} \quad \zeta \to \zeta_w = \delta_w/l_{cw} \tag{3.39}$$

and that the no slip condition is satisfied at the bottom

$$\vec{w} = -\vec{u}_w \qquad \text{at} \quad \zeta = \zeta_o = z_o/l_{cw} \tag{3.40}$$

where $z_o = k_b/30$ and k_b is the physical bottom roughness.

The general solution to equation (3.38) is

$$\vec{w} = A\,(\text{Ber}\, 2\zeta^{1/2} + i\,\text{Bei}\, 2\zeta^{1/2}) + B\,(\text{Ker}\, 2\zeta^{1/2} + i\,\text{Kei}\, 2\zeta^{1/2}) \tag{3.41}$$

where Ber, Bei, Ker, and Kei are Kelvin functions of zeroth order. Since Ber and Bei grow exponentially while Ker and Kei decay exponentially as ζ increases, (3.39) requires that A = 0. The boundary condition (3.40) then requires that

$$B = \frac{-\vec{u}_w}{\text{Ker } 2\,\zeta_o^{1/2} + i\,\text{Kei } 2\,\zeta_o^{1/2}} \tag{3.42}$$

Solving (3.34) for $\vec{u}_w$ and using (3.33), (3.41) and (3.42) gives the solution for the wave as

$$\vec{u}_w = \vec{u}_b \left[1 - \frac{\text{Ker } 2\zeta^{1/2} + i\,\text{Kei } 2\zeta^{1/2}}{\text{Ker } 2\,\zeta_o^{1/2} + i\,\text{Kei } 2\,\zeta_o^{1/2}}\right] e^{i\omega t} \qquad z < \delta_w \tag{3.43}$$

Equation (3.43) states that the horizontal wave velocity within the wave boundary layer is equal to the maximum potential flow bottom velocity $\vec{u}_b$ multiplied by a vertical decay term and a periodic term. The top of the wave boundary layer is found by letting $\vec{u}_w$ given by (3.43) approach the free stream wave velocity given by (3.33). Since

$$\frac{\text{Ker } 2\,\zeta^{1/2} + i\,\text{Kei } 2\,\zeta^{1/2}}{\text{Ker } 2\,\zeta_o^{1/2} + i\,\text{Kei } 2\,\zeta_o^{1/2}} \ll 1 \tag{3.44}$$

for values of $\zeta \geq 2$, the wave boundary layer thickness is assumed to be

$$\delta_w = 2\,l_{cw} \tag{3.45}$$

Using the small argument expressions for Ker and Kei, equation (3.43) can be written for small ζ as

$$\vec{u}_w = \vec{u}_b \left[1 + \frac{0.5\,(\ln \zeta + 1.154 + i\,\pi/2)}{[\mathrm{Ker}\ 2\,\zeta_o^{1/2} + i\ \mathrm{Kei}\ 2\,\zeta_o]^{1/2}}\right] e^{i\omega t} \tag{3.46}$$

which shows that the wave velocity profile is logarithmic near the bottom.

Equation (3.46) and the eddy viscosity given by (3.25) can then be used to define the maximum boundary shear stress due to the enhanced wave motion as

$$\frac{\vec{\tau}_{w,\,max}}{\rho} = \lim_{z \to o} \left[\nu_t \left(\frac{\partial \vec{u}_w}{\partial z}\right)_{max}\right] = \kappa\, |\vec{u}_{*cw}|\, \vec{u}_b\, \zeta_o^{1/2}\, K \tag{3.47}$$

where

$$K = \frac{1}{2\,\zeta_o^{1/2}} \quad \frac{1}{[\mathrm{Ker}^2\ 2\,\zeta_o^{1/2} + \mathrm{Kei}^2\ 2\,\zeta_o]^{1/2}} \tag{3.48}$$

To find an expression for the combined wave and current friction factor, Grant and Madsen (1979) assume that the maximum shear stress associated with the combined wave and current can be partitioned into the time average shear stress associated with the enhanced current and the maximum shear stress associated with the enhanced wave,

$$|\vec{\tau}_{cw}| = |\vec{\tau}_c + \vec{\tau}_{w,\,max}| \tag{3.49}$$

After substituting (3.11), (3.21), and (3.47) into (3.49), the equation for the combined wave and current friction factor is found to be

(3.50)

$$\left[0.097 \left(\frac{k_b}{A_b}\right)^{1/2} \frac{K}{f_{cw}^{3/4}}\right]^2 + 2\left[0.097 \left(\frac{k_b}{A_b}\right)^{1/2} \frac{K}{f_{cw}^{3/4}}\right]\left[\frac{V_2}{2\alpha^{1/4}}\right] \cos \bar{\phi}_c = \frac{\alpha^{3/2}}{4} - \frac{V_2^2}{4\alpha^{1/2}}$$

where A_b is the bottom excursion amplitude for the wave defined as

$$A_b \omega = |\vec{u}_b| \tag{3.51}$$

and it is assumed that $\kappa = 0.4$. The friction factor f_{cw} is plotted in Figure 3.3 as a function of the relative current magnitude $|\vec{u}_a|/|\vec{u}_b|$ and the relative roughness k_b/A_b for $\phi_c = 0°$ and $\phi_c = 90°$.

3.1.4 Solution for the current

Averaging equation (3.26) over a wave period yields the following governing equation for the current

$$f \hat{k} \times \vec{u}_c = -\frac{1}{\rho} \vec{\nabla} p_c + \frac{\partial}{\partial z}\left(\nu_t \frac{\partial \vec{u}_c}{\partial z}\right) \tag{3.52}$$

In the constant stress region for the current, the turbulent stress term in parentheses is equal to the time average stress associated with the time average current

$$\nu_t \frac{\partial \vec{u}_c}{\partial t} = \vec{\tau}_c = |\vec{u}_{*c}| \vec{u}_{*c} \tag{3.53}$$

Using the eddy viscosity profile given by (3.24) and (3.25), (3.53)

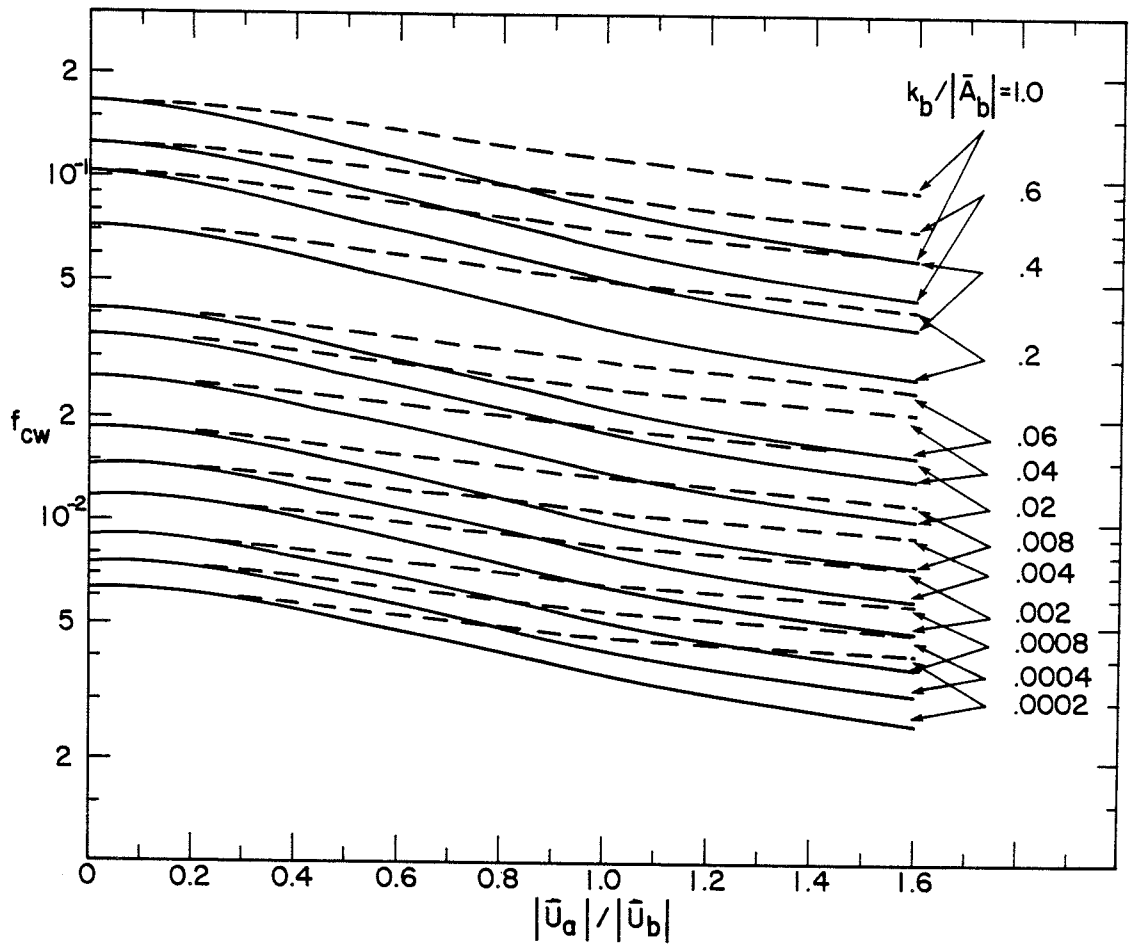

FIGURE 3.3

Friction factor f_{cw} in (3.50) as a function of $|\vec{u}_a|/|\vec{u}_b|$ and k_b/A_b for $\phi_c = 0^\circ$ (solid line) and for $\phi_c = 90^\circ$ (dashed line). Grant and Madsen (1979).

can be rewritten as

$$\frac{\partial \vec{u}_c}{\partial z} = \frac{\vec{u}_{*c}}{\kappa z} \qquad z > \delta_w \tag{3.54}$$

and

$$\frac{\partial \vec{u}_c}{\partial z} = \frac{|\vec{u}_{*c}|}{|\vec{u}_{*cw}|} \frac{\vec{u}_{*c}}{\kappa z} \qquad z < \delta_w \tag{3.55}$$

The wave influences the current shear above the wave boundary layer through the time average shear stress. Since $|\vec{u}_{*c}| < |\vec{u}_{*cw}|$, the current shear within the wave boundary layer is reduced.

Integrating (3.55) and applying the no slip boundary condition at z_o,

$$\vec{u}_c = 0 \qquad \text{at} \qquad z = z_o = k_b/30 \tag{3.56}$$

the solution for the current velocity in the wave boundary layer becomes

$$\vec{u}_c = \frac{\vec{u}_{*c}}{\kappa} \frac{|\vec{u}_{*c}|}{|\vec{u}_{*cw}|} \ln \frac{z}{z_o} \qquad z < \delta_w \tag{3.57}$$

Integrating equation (3.54) and applying the boundary condition that the current velocity appears to go to zero at z_{oc},

$$\vec{u}_c = 0 \qquad \text{at} \qquad z = z_{oc} = k_{bc}/30 \tag{3.58}$$

where k_{bc} is the apparent bottom roughness, the solution for the

current velocity above the wave boundary layer becomes

$$\vec{u}_c = \frac{\vec{u}_{*c}}{\kappa} \ln \frac{z}{z_{oc}} \qquad z > \delta_w \tag{3.59}$$

Since Coriolis acceleration of the current is negligible in the constant stress layer, the current velocity vector is in the direction of the mean shear stress $\bar{\phi}_c$ in this region. An expression for the apparent bottom roughness felt by the current above the wave boundary layer can be found by matching (3.57) and (3.59) at $z = \delta_w$,

$$\frac{z_{oc}}{z_o} = \left(\frac{\delta_w}{z_o}\right)^{\left(1 - |\vec{u}_{*c}| / |\vec{u}_{*cw}|\right)} \tag{3.60}$$

The apparent bottom roughness is highly dependent on wave characteristics. z_{oc} increases as the wave boundary layer thickness δ_w increases, however, z_{oc} is always constrained to be less than δ_w. Since the ratio $|\vec{u}_{*c}| / |\vec{u}_{*cw}|$ decreases as the relative magnitude of the current decreases, the ratio z_{oc}/z_o is greatest for small currents and large waves. The ratio of the apparent bottom roughness k_{bc} to the physical bottom roughness k_b is plotted in Figure 3.4 as a function of the relative current magnitude $|\vec{u}_a| / |\vec{u}_b|$ and the relative roughness k_b/A_b for $\phi_c = 0°$.

3.1.5 Solution procedure

To calculate near bottom velocity profiles for the wave and

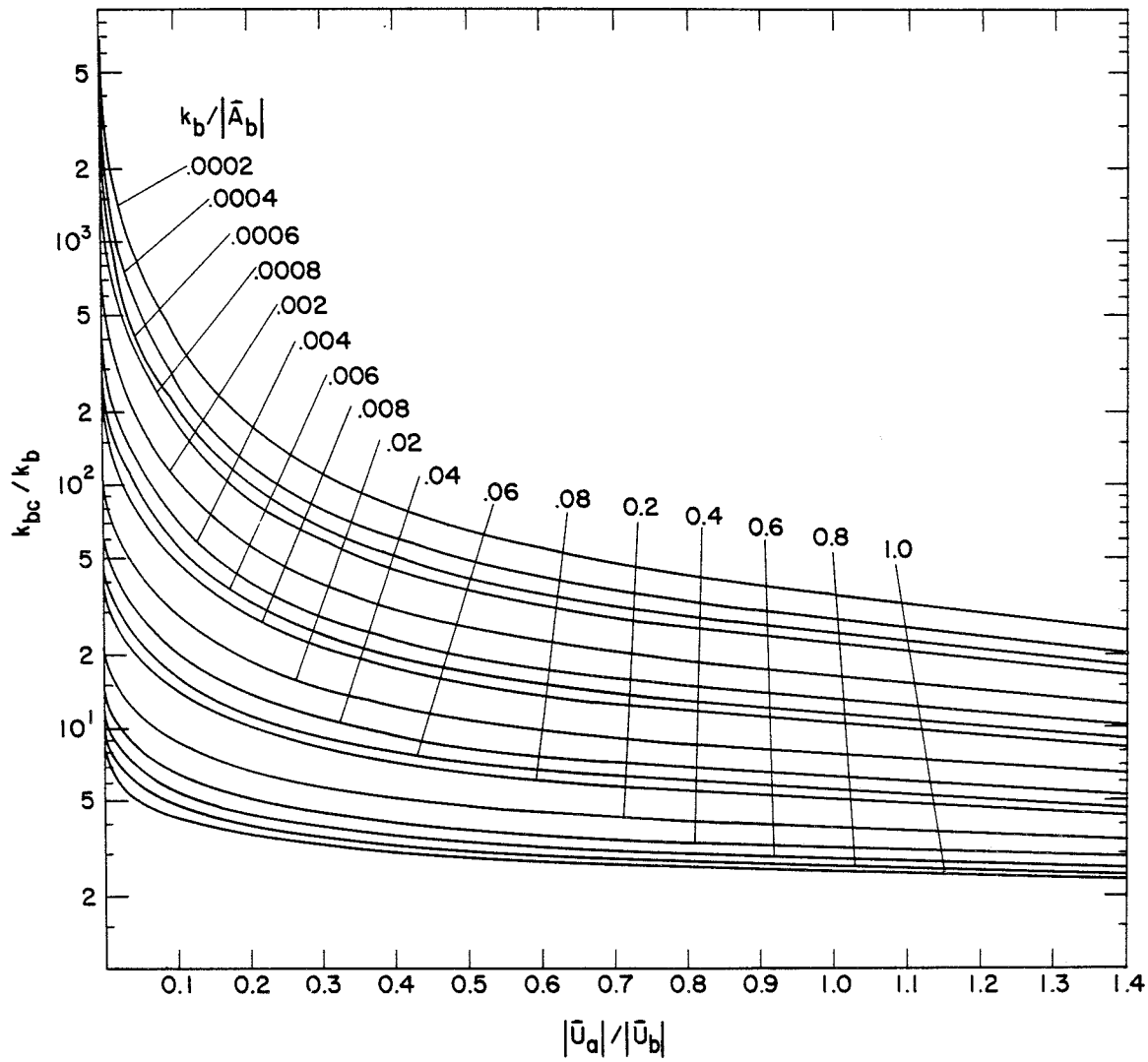

FIGURE 3.4
Apparent bottom roughness k_{bc}/A_b given by (3.60) as a function of k_b/A_b and $|\vec{u}_a|/|\vec{u}_b|$ for $\phi_c = 0°$. Grant and Madsen (1979).

current, the neutral near bottom model developed by Grant and Madsen (1979) requires as input the maximum bottom orbital velocity $|\vec{u}_b|$ and excursion amplitude A_b for the wave, the current speed $|\vec{u}_r|$ and direction with respect to the wave $\bar{\phi}_c$ at a known height above the bottom z_r, and the physical bottom roughness k_b. Because the near bottom model applies only to the current constant stress layer, z_r also is required to be in the constant stress region. Using the wave variables $|\vec{u}_b|$ and A_b as master velocity and length scales, these conditions can be arranged into four dimensionless input parameters,

$$\frac{|\vec{u}_r|}{|\vec{u}_b|} \quad , \quad \frac{z_r}{A_b} \quad , \quad \bar{\phi}_c \quad , \text{ and } \frac{k_b}{A_b} \, .$$

The relative angle $\bar{\phi}_c$ need only be specified within the range $0^\circ \leq \bar{\phi}_c \leq 90^\circ$ since linear wave theory has been used to describe the wave.

To solve for the velocity profiles, an iterative procedure is adopted in which a value is initially guessed for the relative magnitude of the current $|\vec{u}_a| / |\vec{u}_b|$ in the definition of the boundary shear stress. The assumed value of $|\vec{u}_a| / |\vec{u}_b|$ is used to calculate ϕ_c from (3.17), (3.19) or Figure 3.1. The parameters α and V_2 can then be calculated; α from (3.22) and V_2 from (3.16), (3.18) or Figure 3.2. The friction factor f_{cw} is found using (3.50) or Figure 3.3. The characteristic shear velocities $|\vec{u}_{*c}|$ and $|\vec{u}_{*cw}|$ follow from (3.20) and (3.23). The wave boundary layer

height δ_w is given by (3.45) and the apparent bottom roughness can be found using (3.60) or Figure 3.4. The current velocity is then calculated at z_r from (3.57) if $z_r < \delta_w$ or from (3.59) if $z_r > \delta_w$. If the calculated magnitude of the current at z_r does not match the known value, the procedure is repeated with a new value of $|\vec{u}_a| / |\vec{u}_b|$. Once the proper value of $|\vec{u}_a| / |\vec{u}_b|$ has been found, the near bottom current velocity profile is given by (3.57) and (3.59) and the wave velocity profile is given by (3.43) and (3.29). An efficient method to find the proper value of $|\vec{u}_a| / |\vec{u}_b|$ is described in Appendix I.

3.2 Physical Bottom Roughness Model

To calculate the instantaneous boundary shear stress as defined by Grant and Madsen (1979) in the previous section, the friction factor must be found by evaluating equation (3.50) for an independently specified value of the physical bottom roughness k_b. As discussed in Chapter 2, the physical bottom roughness of a moveable sediment bed can be partitioned into components associated with drag on sediment grains in the bed, form drag on bedforms, and drag on sediment grains in the near bed transport layer. In this section, mathematical models for the three bottom roughness components will be discussed. It is found that the relative contribution of each component is a function of the boundary shear stress and the sediment characteristics.

3.2.1 Sediment grain roughness, skin friction, and initiation of motion

The component of the roughness associated with drag on individual sediment grains in the bed is the Nikuradse sand grain roughness k_{bN} based on the sediment diameter d,

$$k_{bN} = d \tag{3.61}$$

If the bed is flat and there is no sediment transport, the total physical bottom roughness is equal to k_{bN}. The boundary shear stress acting on the sediment grains in the bed, labeled skin friction, is found by evaluating the friction factor using k_{bN}. If bedforms exist or sediment is being transported, the total boundary shear stress felt by the flow is calculated using the total k_b, but the skin friction component is still calculated using k_{bN}.

For sediment transport to occur, the skin friction must exceed the critical value for initiation of motion. Madsen and Grant (1976) have shown that Shields criterion for the initiation of sediment motion can be applied to oscillatory flow. The maximum Shields parameter based on skin friction ψ'_m therefore must exceed the critical Shields parameter for initiation of motion ψ_c for sediment to be transported. The maximum Shields parameter is defined as

$$\psi'_m = \frac{\vec{\tau}'_{bm}}{\rho (s-1) gd} \tag{3.62}$$

where τ'_{bm} is the magnitude of the maximum skin friction, g is

the acceleration of gravity, $s = \rho_s/\rho$ is the relative sediment density, and ρ_s is the sediment density. The critical Shields parameter for a clean, non-cohesive, uniform sediment can be obtained from the modified Shields diagram in Figure 3.5 as a function of a dimensionless sediment parameter S_* defined as

$$S_* = \frac{d}{4\nu} [(s-1)gd]^{1/2} \tag{3.63}$$

Grant et al. (1982) have shown that the critical Shields parameter for a bioturbated sediment can be as much as twice the value given by Shields diagram. The actual increase in the critical Shields parameter is found to vary with the type of marine organisms present and with the season of the year.

3.2.2 Roughness associated with general bedforms

The ocean bottom on the continental shelf is rarely flat. Bedforms usually are generated by the flow or by marine organisms. Because the physical bottom roughness associated with bedforms is often orders of magnitude greater than the Nikuradse roughness, a method to determine the roughness due to general, three-dimensional, micro-topography is necessary.

Most bedforms on the continental shelf act as distributed roughness elements characterized by the formation of eddies behind each element and reattachment of the flow between elements. This type of bottom roughness can be expected to depend both on the height and the concentration of the elements. Using the results of Wooding

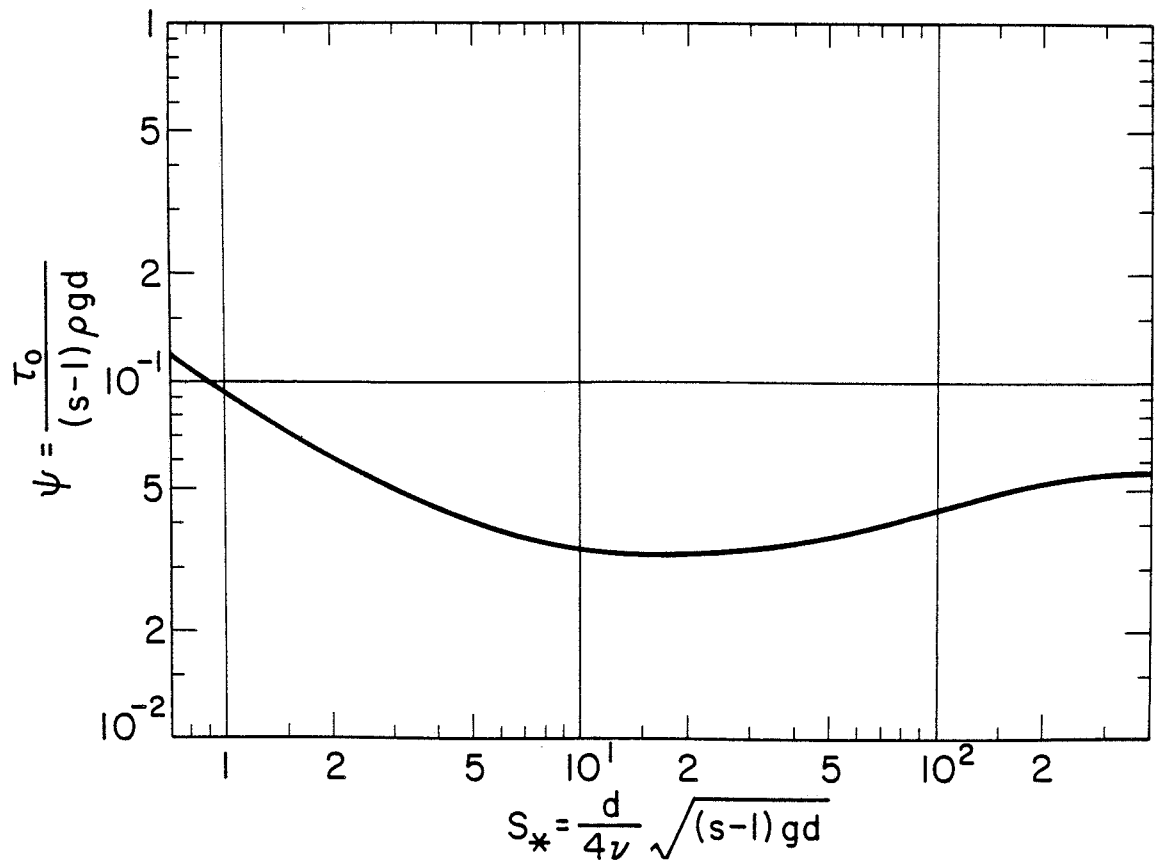

FIGURE 3.5
Modified Shields diagram with the critical Shields parameter ψ_c plotted as a function of S*.

et al. (1973), Grant and Madsen (1982) suggest that the physical bottom roughness associated with distributed roughness elements can be written as

$$k_{bB} \sim 30\, k_h \left[\frac{k_h\, k_w}{k_L\, k_W}\right] f\left(\frac{k_h}{k_1}, \frac{k_h}{k_w}\right) \tag{3.64}$$

where k_h is the height, k_w the cross-stream width, and k_1 the streamwise length of the roughness element; k_W is the cross-stream width and k_L is the streamwise length of the flat bottom area associated with the roughness element; and $f\,(k_h/k_1,\ k_h/k_w)$ is an aspect ratio function. The concentration is defined as the ratio of the frontal area of the roughness element to the area of the flat bottom associated with the element, $[k_h k_w / k_L k_W]$.

Wooding et al. (1973) do not investigate the dependence on the height to cross-stream width ratio since k_h/k_w is always small in their data. Based on their data, Wooding et al. (1973) estimates the aspect ratio function as

$$f\,(k_h/k_1,\ k_h/k_w) \sim (k_h/k_1)^a \tag{3.65}$$

where $a = 0.38$ for $1/3 < k_h/k_1 < 2$.

Using equations (3.64) and (3.65), the physical bottom roughness for a two-dimensional ($k_w = k_W$) roughness element with a streamwise length equal to its height ($k_1 = k_h$) is approximately (Grant and Glenn, in press)

$$k_{bB} \sim 30\, k_h\, (k_h/k_L) \tag{3.66}$$

3.2.3 Roughness associated with wave generated ripples

If the skin friction is large enough to initiate sediment motion and the sediment is a sand or large silt that can be transported as bedload, a flat bed is unstable and ripples will form. Since the boundary shear stress in a combined wave and current flow is usually dominated by the wave, ripples are expected to be wave dominated. Ripples generated by waves are symmetrical and nearly two-dimensional. The height and streamwise length of the ripple peak are approximately equal, but both are much smaller than the ripple wave length. The expressions for ripple geometry and the bottom roughness associated with ripples developed by Grant et al. (in prep.) and Grant and Madsen (1982) for pure oscillatory flow will be discussed here.

Depending on the value of the maximum Shields parameter based on skin friction ψ'_m, Grant et al. (in prep.) find that ripples are either in an equilibrium range or a breakoff range. The transition point between the two ranges is labeled the breakoff point and can be obtained from the empirical relation.

$$(\psi_B/\psi_c) = 1.8\ S_*^{0.6} \tag{3.67}$$

where ψ_B is the Shields parameter at the breakoff point. If $\psi_c < \psi'_m < \psi_B$, ripples are in the equilibrium range. The ripple length λ scales with the bottom excursion amplitude of the wave A_b, while the ripple steepness n/λ, where n is the ripple height, is approximately constant and equal to a maximum. Grant et al. (in prep) find that ripple geometry in the equilibrium range can

be estimated by the empirical relationships

$$\frac{n}{A_b} = 0.22\ (\psi'_m/\psi_c)^{-0.16}$$

and $$\psi_c < \psi'_m < \psi_b \tag{3.68}$$

$$\frac{n}{\lambda} = 0.16\ (\psi'_m/\psi_c)^{-0.04}$$

If $\psi'_m > \psi_B$, ripples are in the breakoff range. Ripple length is no longer strongly correlated with the bottom excursion amplitude and the ripple height decays. Grant et al. (in prep.) find that ripple geometry in the breakoff range can be estimated by the empirical relationships

$$\frac{n}{A_b} = 0.48\ S_*^{0.8}\ (\psi'_m/\psi_c)^{-1.5}$$

and $$\psi'_m > \psi_B \tag{3.69}$$

$$\frac{n}{\lambda} = 0.28\ S_*^{0.6}\ (\psi'_m/\psi_c)^{-1.0}$$

Because ripples act as distributed roughness elements as discussed in the previous section, the physical bottom roughness associated with ripples is expected to depend on the ripple height, concentration, and aspect ratio. Assuming the ripples are nearly two-dimensional, the ripple concentration reduces to the ripple steepness. Assuming the height and streamwise length of the ripple peak are approximately equal, the effect of the aspect ratio can be neglected. With these assumptions, Grant and Madsen (1982) use standard law-of-the-wall arguments to derive the following expression for the physical bottom roughness associated with wave formed ripples,

$$k_{bB} = 27.7\ \eta\ \eta/\lambda \tag{3.70}$$

an expression similar to equation (3.66).

Using equations (3.68), (3.69) and (3.70), the relative roughness k_b/A_b associated with the ripples is found to be largest when the skin friction just exceeds the critical shear stress for initiation of motion. As the skin friction increases, the relative roughness decreases slowly until the breakoff point is reached. Once the breakoff point is passed, further increases in skin friction cause rapid decreases in the relative roughness. The rapid decrease in the roughness is associated mainly with the decay in ripple height as ripples are washed out. Wave generated ripples therefore have the greatest effect on the relative roughness when the boundary shear stress is small.

3.2.4 Roughness associated with near bed transport in oscillatory flow

If the skin friction exceeds the critical shear stress for initiation of motion, near bed transport of sediment also begins. Owen (1964) hypothesized that the turbulence associated with the wake structure around individual sediment grains in the near bed layer causes the flow to feel a bottom roughness proportional to the height of the layer. As the shear stress increases, the layer height and the resulting bottom roughness also increase. As with ripples, near

bed transport effects depend on the boundary shear stress, which is time dependent and usually wave dominated. Since the maximum dissipation occurs when the shear stress is highest, Grant and Madsen (1982) argue that the bottom roughness can be related to the maximum height of the near bed transport layer. A method to predict the height of the near bed layer and the associated bottom roughness is presented here.

Grant and Madsen (1982) argue that particles moving along the bed are deflected upwards by collisions with particles in the bed. Particles that lose little velocity in the collision and leave the bed vertically will determine the height of the near bed layer. This height can be estimated by balancing the initial kinetic energy of the particle as it leaves the bed with its final potential energy at the top of its trajectory. The resulting height of the near bed transport layer h_T is

$$h_T = \frac{(s + c_m)}{(s - 1)} \frac{w_o^2}{2g} \tag{3.71}$$

where w_o is the initial particle speed and c_m is the mass coefficient for the particle (c_m = 1/2 for a sphere).

The maximum height of the near bed transport layer is found by setting w_o equal to the maximum horizontal particle velocity. Assuming no significant variation in the forces acting on particle during the time it takes to accelerate, Grant and Madsen (1982) find the maximum horizontal particle velocity by neglecting the horizontal

inertia force and balancing the maximum horizontal fluid drag with the maximum horizontal friction force between the particle and the bed. The resulting expression for the maximum horizontal particle velocity in the near bed transport layer is

$$u_{Tm} = e\,[(s - 1)gd]^{1/2}\,\psi_c^{1/2}\,[(\psi'_m/\psi_c)^{1/2} - b] \qquad \psi'_m > \psi_c \tag{3.72}$$

where $e = 9.2$ and $b = 0.7$ were determined from data. Substituting (3.72) into (3.71), the maximum height of the near bed transport layer for spherical particles is

$$h_{Tm} = 42\,(s + 1/2)\,d\,\psi_c\,[(\psi'_m/\psi_c)^{1/2} - 0.7]^2 \qquad \psi'_m > \psi_c \tag{3.73}$$

Using (3.73) to predict the maximum layer height and data from Carsten's et al. (1969) oscillatory flow over a moveable bed experiment, Grant and Madsen (1982) find that the bottom roughness associated with near bed transport is

$$k_{bT} = 3.8\,h_{Tm} \tag{3.74}$$

3.2.5 Total roughness in a combined wave and current flow

The total physical bottom roughness is found by adding the components associated with sediment grains, bedforms, and near bed transport,

$$k_b = k_{bN} + k_{bB} + k_{bT} \tag{3.75}$$

Since $k_{bN} \ll k_{bB}$ or k_{bT} for most cases of interest on the

continental shelf, the Nikuradse roughness given by (3.61) is usually neglected. The bottom roughness associated with bedforms, which is most important when the shear stress is low, is given by (3.64) for general bedforms and (3.70) for wave generated ripples. If ripple geometry is not known, it can be estimated from equations (3.68) or (3.69). The bottom roughness associated with near bed transport, which is most important when the shear stress is high, is given by equations (3.73) and (3.74).

Because the expression for ripple geometry, ripple roughness, and near bed transport roughness were developed using laboratory data for oscillatory flow over a clean, uniform sand with dimensionless sediment parameters S_* of order 1-15, they should be applied with some degree of caution to general field conditions on the continental shelf. For very fine silts with $S_* < 0.375$, equation (3.67) predicts that $\psi_B < \psi_c$, implying that equilibrium range ripples do not form and the physical bottom roughness is dominated by near bed transport. Since ripples are not expected to form in very fine sediment, this result seems reasonable but is untested. Because the available data used to develop equations (3.68) and (3.69) was for predominently oscillatory flow only, these equations should be used cautiously if the current has a significant influence on the boundary shear stress ($|\vec{u}_a|/|\vec{u}_b| \sim 0(1)$). With no additional data available to generalize the existing theory, equations (3.68) and (3.69) for ripple geometry will be adopted for the full range of sediment and flow conditions until new information is available. If

ripples are not actively being generated by the ambient flow, however, the equations for ripple geometry do not apply and the ripples should be treated as general bedforms.

Sediment on the continental shelf typically is a bioturbated mixture of particles with different sizes and densities. To use equations (3.68), (3.69), and (3.73), the sediment class that dominates the bottom roughness must be chosen. If the sediment size and density distribution is not narrow and unimodal, the bottom roughness is usually dominated by the larger sediment that is transported as bedload, since the smaller sediment is often forced into suspension. Using (3.68) or (3.69) to predict ripple geometry in this case assumes that enough sediment is available in the proper size class to form full size ripples. Equations (3.68), (3.69), and (3.73) also depend on the critical Shields parameter for initiation of motion, which, for a bioturbated sediment mixture, can be different from the clean, uniform sediment value given by Shields diagram.

3.2.6 Solution procedure

The neutral near bottom model discussed in Section 3.1 requires the relative roughness k_b/A_b to be specified as an input parameter. The value of k_b is supplied by the physical bottom roughness model. If sediment is not being transported by the flow, the constant bottom roughness associated with general bedforms given by (3.64) can be specified directly. If ripple geometry (n/A_b, n/λ) is known, the bottom roughness associated with ripples can be calculated from (3.70). If ripple geometry or the roughness associated with near bed

transport must be calculated, however, the neutral near bottom model must supply a value for the skin friction.

Additional dimensionless input parameters required to calculate ripple geometry or the height of the near bed transport layer are

$$\frac{d}{A_b}, \quad s, \quad S_*, \quad \text{and} \quad \frac{[(s-1)\, gd]^{1/2}}{u_b}$$

The iterative procedure adopted is similar to that discussed in Section 3.1.5. The assumed value of $|\vec{u}_a|/|\vec{u}_b|$ is used to calculate ϕ_c, α, and V_2. Since k_b/A_b is not yet known, equation (3.50) cannot be evaluated for f_{cw}. The skin friction factor f'_{cw}, however, can be found from (3.50) if the relative sediment grain diameter d/A_b is substituted for the relative roughness k_b/A_b. The maximum skin friction τ'_{cw} can be calculated from f'_{cw} and (3.21), which can be used to find the maximum Shields parameter ψ'_m from $[(s-1)\, gd]^{1/2}/|\vec{u}_b|$ and (3.62). The critical Shields parameter ψ_c and the breakoff Shields parameter ψ_B can be found from S_*, Figure 3.5 and equation (3.67). Ripple geometry can be calculated from (3.68) or (3.69) and the maximum height of the near bed transport layer can be calculated from (3.73). The total physical bottom roughness, given by (3.61), (3.70), (3.74) and (3.75), then can be used in (3.50) to find the total friction factor f_{cw}. Continuing as in Section 3.1.5, the characteristic shear velocities are found and the calculated current velocity at z_r is compared to the given current velocity at z_r. Once the proper value of $|\vec{u}_a|/|\vec{u}_b|$ is found, near bottom velocity profiles for the wave and the current can be constructed as before.

4. THEORETICAL MODEL FOR A STRATIFIED NEAR BOTTOM FLOW IN COMBINED WAVES AND CURRENTS OVER A MOVEABLE BED

The bottom boundary layer on the continental shelf is often affected by stable stratification. Since the ocean bottom does not act as a heat sink or salinity source, the high mixing rates associated with the near bottom turbulence will smooth out any density differences due to temperature and salinity, forming a bottom mixed layer of nearly constant fluid density. Temperature and salinity induced stratification therefore is not expected to influence the near bottom flow for most cases of interest on the continental shelf.

If the boundary shear stress is sufficiently large, significant amounts of sediment can be suspended by the flow. Unlike temperature and salinity, suspended sediment is not mixed uniformly throughout the near bottom flow field. The upward turbulent diffusion of sediment is balanced by the tendency of the sediment to fall out of suspension, producing a concentration profile that decreases with height. Since the total density of the fluid-sediment suspension also decreases with height, suspended sediment can stably stratify the near bottom flow field. Stable stratification inhibits vertical turbulent transport by decreasing the correlation between vertical and horizontal turbulent fluctuations. Since the turbulent fluxes of mass and momentum can be modified by suspended sediment induced stratification, the eddy viscosity used to model the fluxes must also be modified.

In this chapter, a model for the near bottom flow that includes stratification is developed. The Grant and Madsen (1979) combined wave

and current model is modified for the effects of suspended sediment induced stratification in Section 4.1. Just as the neutral model required a boundary condition to be specified for the fluid velocity, the stratified model will require boundary conditions on both the fluid velocity and the sediment concentration. The usual boundary conditions for rough turbulent flow are that the fluid velocity is zero and the sediment concentration is known at $z_o = k_b/30$. A sediment reference concentration model that specifies the sediment concentration at z_o therefore is developed in Section 4.2. The stratified combined wave and current model then can be run in conjunction with the physical bottom roughness model and the reference concentration model to calculate near bottom fluid velocity and sediment concentration profiles. Sample model runs are discussed in Section 4.3.

4.1 Stratified Combined Wave and Current Model

The effect of suspended sediment induced stratification in combined waves and currents will be modeled by the usual method applied to small sediment concentrations. The sediment is initially treated as distinct particles and the conservation of momentum equation for each particle is solved to find the particle velocity in terms of the fluid velocity. The continuum hypothesis is then invoked and the conservation of sediment mass, fluid mass, and fluid momentum equations are solved for the fluid velocity and sediment concentration profiles. This method has been applied to steady flow by Hunt (1954, 1969), Taylor and Dyer (1977), and Smith and McLean

(1977, 1977), and to oscillatory flow by Kennedy and Loucher (1972). An approach similar to Smith and McLean's (1977, 1977) will be used here to modify the Grant and Madsen (1979) combined wave and current model for the effects of suspended sediment.

4.1.1 Governing equations

The equations governing the flow of a suspension of sediment are greatly simplified if sediment concentrations are low and particle interactions are neglected. Lumley (1978) suggests that particle interactions can be safely neglected for volumetric sediment concentrations less than 3×10^{-3}, which for quartz is equivalent to a mass concentration of 8×10^{3} milligrams/liter. Except in the immediate vicinity of the bed, maximum volumetric concentrations on the continental shelf are expected to be of order 10^{-3}. Particle interactions therefore are neglected and the governing equations are developed assuming sediment concentrations are small.

Conservation of momentum can be applied to a single particle in a turbulent flow as described by Soo (1967) or Hinze (1959). If the particle diameter and response time are much smaller than the turbulent length and time scales, the conservation of momentum equation for a single particle reduces to

$$\vec{u}_n = \vec{u} \qquad (4.1)$$

$$w_n = w - w_{fn}$$

where $\vec{u}_n$ and w_n are the horizontal and vertical particle velocities, $\vec{u}$ and w are the horizontal and vertical fluid velocities,

and w_{fn} is the particle fall velocity. The particle fall velocity is found by balancing the submerged particle weight with the fluid drag force on the particle. The nondimensional fall velocity for a spherical particle is plotted in Figure 4.1 as a function of the nondimensional sediment parameter S_* (Madsen and Grant, 1976). For $S_* < 1$, Stokes drag law applies and the nondimensional fall velocity is given by

$$\frac{w_{fn}}{[(s-1)\ gd]^{1/2}} = \frac{2}{9} S_* \qquad S_* < 1 \tag{4.2}$$

Grant and Madsen (1982) have shown that the response time of a particle with diameter d in turbulent flow is approximately d/u_*. In the constant stress layer, the large energetic eddies responsible for the momentum flux have a length scale z and a time scale z/u_*. Because suspended sediment induced stratification is expected to be important when the boundary shear stress is high, the physical bottom roughness is expected to be dominated by near bed transport and z_o will be much greater than d. Since $d << z$ throughout the boundary layer, equation (4.1) is assumed to be valid for the momentum transporting eddies. That (4.1) may not be valid for the small dissipation scale eddies is not important for this application. Because dissipation merely adjusts to balance the combined effects of turbulent production and buoyancy, dissipation scale eddies do not effect the momentum flux. Since the effects of suspended sediment induced stratification on vertical turbulent momentum transport is being modeled here, equation (4.1) is considered an adequate

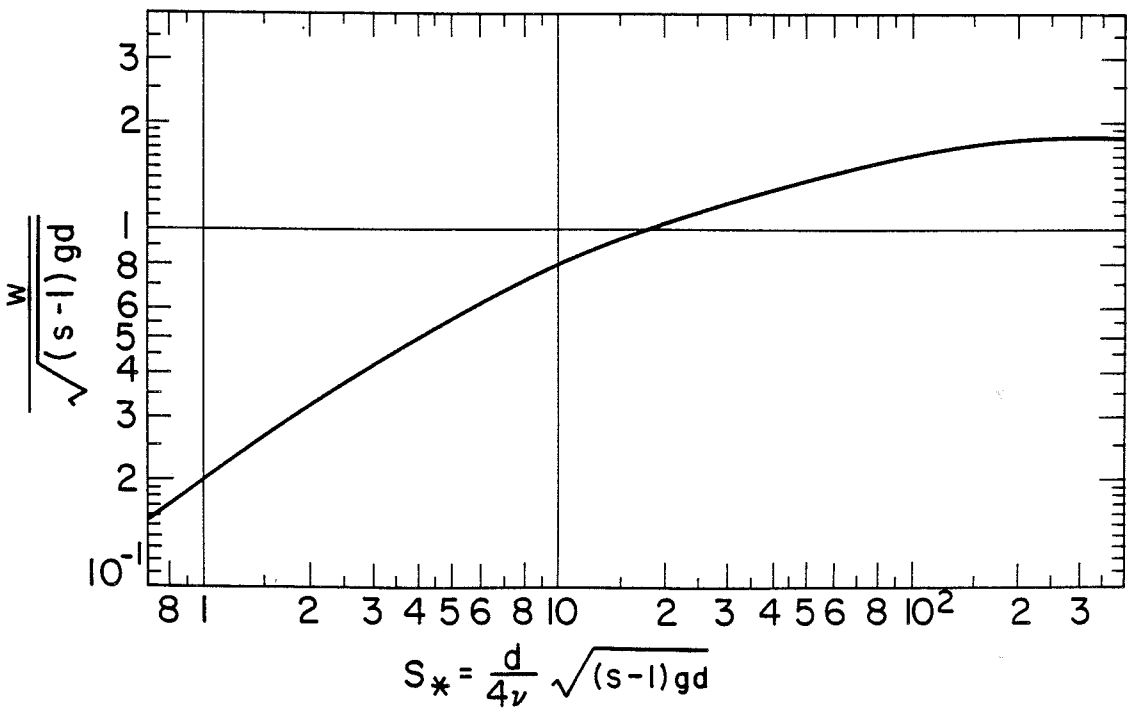

FIGURE 4.1
Dimensionless particle fall velocity plotted as a function of S_* for spherical particles.

$$\text{For } S_* < 1, \quad \frac{w}{[(s-1)\ d]^{1/2}} = \frac{2}{9}\ S_*$$

approximation for the particle velocity.

As discussed by Lumley (1978), the fluid-sediment suspension then is treated as a continuum. The sediment is divided into size and density classes and each sediment class is treated as a distinct phase. Conservation equations then can be written for sediment mass in each sediment class n,

$$\frac{\partial C_n}{\partial t} + \vec{\nabla} \cdot (C_n \vec{u}_n) + \frac{\partial}{\partial z}(C_n w_n) = 0 \tag{4.3}$$

for fluid mass,

$$\frac{\partial C}{\partial t} + \vec{\nabla} \cdot (C \vec{u}) + \frac{\partial}{\partial z}(C w) = 0 \tag{4.4}$$

and for fluid momentum

$$\frac{D\vec{u}}{Dt} + 2\Omega_v \hat{k} \times \vec{u} + 2\vec{\Omega}_H \times w\hat{k} = -\frac{1}{\rho}\vec{\nabla} p + \nu\left(\vec{\nabla}^2 \vec{u} + \frac{\partial^2 \vec{u}}{\partial z^2}\right) \tag{4.5}$$

where C_n is the volumetric concentration of sediment in class n and C is the volumetric concentration of fluid. The relation between C and C_n is simply

$$C + \sum_n C_n = 1 \tag{4.6}$$

Assuming that the sediment velocity in class n is given by (4.1), conservation of sediment mass can be rewritten

$$\frac{\partial C_n}{\partial t} + \vec{\nabla} \cdot (C_n \vec{u}) + \frac{\partial}{\partial z}(C_n w) - w_{fn}\frac{\partial C_n}{\partial z} = 0 \tag{4.7}$$

Using (4.6) and (4.7), conservation of fluid mass becomes

$$\vec{\nabla} \cdot \vec{u} + \frac{\partial w}{\partial z} - \sum_n w_{fn} \frac{\partial C_n}{\partial z} = 0 \tag{4.8}$$

For the small sediment concentrations expected on the continental shelf, the vertical fluid velocity induced by the sediment falling out of suspension ($= \sum_n w_{fn} C_n$) is small and the usual continuity equation

$$\vec{\nabla} \cdot \vec{u} + \frac{\partial w}{\partial z} \sim 0 \tag{4.9}$$

is recovered.

The fluid velocity and pressure again can be partitioned into current, wave, and turbulent components as in equation (3.2). The concentrations can be partitioned into mean, periodic and turbulent components

$$\begin{aligned} C_n &= C_{nm} + C_{np} + C_{n'} \\ C &= C_m + C_p + C' \end{aligned} \tag{4.10}$$

where the subscript m denotes the mean concentration associated with the wave and current, the subscript p denotes the periodic concentration associated with the wave, and the prime denotes the turbulent concentration fluctuation. The partitioned variables are then substituted into the conservation equations which are Reynolds averaged as before.

The governing equations can be simplified using scaling arguments

similar to those used in the neutral case. The current and mean concentration are assumed to be quasi-steady and horizontally homogeneous. Coriolis acceleration of the wave is neglected compared to the local acceleration of the wave. Viscous stresses are neglected compared to Reynolds stresses since rough turbulent flow is expected. Suspended sediment induced stratification is expected to be most important when the boundary shear stress is large enough to suspend significant amounts of sediment. When the boundary shear stress is large, it is anticipated that ripples will be washed out and the dominant horizontal length scale is the length of the wave. Horizontal derivatives of the turbulent fluxes then can be neglected compared to vertical derivatives. In the momentum equation, the remaining nonlinear convective accelerations can be neglected compared to the local acceleration if the magnitude of the wave and current velocities are much less than the wave phase speed. A similar argument can be applied to the sediment mass equation. The order of magnitude of nonlinear terms involving the periodic concentration are

$$(\vec{u}_c + \vec{u}_w)\cdot\vec{\nabla} C_{np} \sim O\left(u \frac{C_{np}}{\lambda_w}\right) \tag{4.11}$$

and

$$w_w \frac{\partial C_{np}}{\partial z} \sim O\left(\frac{u z}{\lambda_w} \frac{C_{np}}{z}\right) \tag{4.12}$$

where u is the magnitude of $\vec{u}_c$ or $\vec{u}_w$, λ_w is the wave length,

and the continuity equation has been used to estimate w_w. The order of magnitude of the local time derivative of the periodic concentration is

$$\frac{\partial C_{np}}{\partial t} \sim O\left(\frac{C_{np}}{T}\right) \tag{4.13}$$

where T is the wave period. Since the wave phase speed is defined as

$$c_w = \lambda_w / T \tag{4.14}$$

the terms in (4.11) and (4.12) can be neglected compared to (4.13) if $u << c_w$. The resulting equations governing the near bottom flow are

$$\frac{\partial \vec{u}_w}{\partial t} + f \hat{k} \times \vec{u}_c = -\frac{1}{\rho} \vec{\nabla} (p_c + p_w) + \frac{\partial}{\partial z} (-\overline{\vec{u}'w'}) \tag{4.15}$$

$$\frac{\partial C_{np}}{\partial t} + w_w \frac{\partial C_{nm}}{\partial z} - w_{fn} \frac{\partial}{\partial z} (C_{nm} + C_{np}) + \frac{\partial}{\partial z} (\overline{C_n'w'}) = 0 \tag{4.16}$$

Equation (4.15) is the same conservation of momemtum equation derived by Grant and Madsen (1979). To this, the unsteady conservation of sediment mass equation given by (4.16) has been added.

4.1.2 Turbulent closure scheme

A turbulent closure scheme similar to the eddy viscosity model used by Grant and Madsen (1979), but modified for the effects of stratification, is used to solve (4.15) and (4.16). The closure scheme assumes that the vertical turbulent fluxes can be written as an eddy diffusivity multiplied by the vertical gradient of the appropriate Reynolds averaged quantity,

$$- \overrightarrow{u'w'} = \nu_{tm} \frac{\partial}{\partial z} (\vec{u}_c + \vec{u}_w) \tag{4.17}$$

$$- \overline{C'_n w'_n} = \nu_{ts} \frac{\partial}{\partial z} (C_{nm} + C_{np}) \tag{4.18}$$

$$- \overline{C'w'} = \nu_{tf} \frac{\partial}{\partial z} (C_m + C_p) \tag{4.19}$$

where ν_{tm}, ν_{ts}, and ν_{tf} are the eddy diffusivities of momentum, sediment mass, and fluid mass. From the assumed sediment velocity in equation (4.1), it follows that $w'_n = w'$ and

$$- \overline{C'_n w'} = \nu_{ts} \frac{\partial}{\partial z} (C_{nm} + C_{np}) \tag{4.20}$$

Equation (4.6) can be used to show that $C' = - \sum_n C'_n$ and $(C_m + C_p) = 1 - \sum_n (C_{nm} + C_{np})$. Substituting these expressions into (4.19) and comparing the result with (4.20), it follows that the eddy diffusivities of sediment mass and fluid mass are equal. In a thermally stratified turbulent flow such as the atmospheric boundary layer, heat is diffused with fluid mass. Since the eddy diffusivities of heat and fluid mass are equal, it is postulated that temperature and suspended sediment induced stratification have similar effects on the eddy diffusivities.

By analogy with atmospheric surface layer models, the eddy diffusivities for a stably stratified ocean bottom boundary layer are

defined as

$$\nu_{tm} = \frac{\nu_t}{\phi_m} \tag{4.21}$$

and

$$\nu_{ts} = \frac{\nu_t}{\phi_s} \tag{4.22}$$

where ν_t is the neutral eddy viscosity, ϕ_m is the nondimensional velocity gradient, and ϕ_s is the nondimensional concentration gradient. ϕ_m and ϕ_s are defined as

$$\phi_m = 1 + \beta\ z/L \tag{4.23}$$

and

$$\phi_s = \gamma + \beta\ z/L \tag{4.24}$$

where γ and β are constants, L is the Monin-Obukov length, and z/L is the stability parameter. For stable conditions, Businger et al. (1971) determine that $\beta \sim 4.7$ and $\gamma \sim 0.74$ using atmospheric boundary layer data.

The Monin-Obukov length, defined as

$$L = \frac{|\vec{u}_*|^3\ \bar{\rho}}{\kappa\, g\ \overline{\rho' w'}} \tag{4.25}$$

where $\bar{\rho}$ is the Reynolds averaged density and ρ' is the turbulent density fluctuation, can be used to write the stability parameter as

$$\frac{z}{L} = \frac{\nu_t}{|\vec{u}_*|^4} \frac{g}{\bar{\rho}} \overline{\rho' w'} \tag{4.26}$$

The Richardson flux number, defined as the ratio of the amount of turbulent kinetic energy absorbed by buoyancy to that produced by the mean shear

$$R_f = \frac{(g \overline{\rho' w'}/\bar{\rho})}{(|\vec{u}_*|^4/\nu_{tm})} \tag{4.27}$$

is related to the stability parameter by

$$R_f = \frac{1}{\phi_m} \frac{z}{L} \tag{4.28}$$

or

$$\frac{z}{L} = \frac{R_f}{1 - \beta R_f} \tag{4.29}$$

As stable stratification decreases and $R_f \to 0$, the preceeding equations require $z/L \to 0$, $\nu_{tm} \to \nu_t$, and $\nu_{ts} \to \nu_t/\gamma$. The eddy diffusivity of momentum approaches the neutral eddy viscosity and assuming $\gamma < 1$, the eddy diffusivity of mass approaches a larger value. As stable stratification increases and $R_f \to 1/\beta$, the preceeding equations require $z/L \to \infty$, and $\nu_{tm} \sim \nu_{ts} \to 0$. The eddy diffusivities are approximately equal but very small, implying that stable stratification inhibits vertical turbulent transport.

The ratio of the eddy diffusivities varies in the range $1/\gamma > \nu_{tm}/\nu_{ts} > 1$. The Businger et al. (1971) value of $\gamma = 0.74$ corresponds to an upper limit of 1.35. Hunt (1968) quotes two suspended sediment experiments that find $1.5 > \nu_{tm}/\nu_{ts} > 1.2$. The Businger et al. (1971) values for γ and β therefore appear reasonable and will be used until better data is available.

Suspended sediment induced stratification in the ocean bottom boundary layer will be modeled similar to thermal stratification in the atmospheric surface layer. Defining the total density of the fluid-sediment suspension as

$$\rho_T = \rho \left[1 + \sum_n (s_n-1)\, C_n\right] \tag{4.30}$$

and substituting partitioned variables for ρ_T and C_n, it is found that after Reynolds averaging

$$\bar{\rho}_T = \rho \left[1 + \sum_n (s_n-1)\, (C_{nm} + C_{np})\right] \sim \rho \tag{4.31}$$

and

$$\rho'_T = \rho \sum_n (s_n-1)\, C'_n \tag{4.32}$$

The stability parameter for suspended sediment induced stratification then can be written

$$\frac{z}{L} = \frac{\nu_t}{|\vec{u}_*|^4} \sum_n g\, (s_n-1)\, \overline{C'_n w'} \tag{4.33}$$

As in the neutral case, the eddy diffusivities must reflect the mass and momentum transporting properties of both the wave and the current boundary layers. The characteristic shear stress above the wave boundary layer again is assumed to be the time average defined by (3.15) and the characteristic shear stress within the wave boundary layer is assumed to be the maximum defined by (3.21). The neutral eddy viscosity profile will be that adopted by Grant and Madsen (1979),

$$\nu_{tc} = \kappa |\vec{u}_{*c}| z \qquad z > \delta_w \tag{4.34}$$

and

$$\nu_{tcw} = \kappa |\vec{u}_{*cw}| z \qquad z < \delta_w \tag{4.35}$$

where $|\vec{u}_{*c}|$ and $|\vec{u}_{*cw}|$ are defined by (3.20) and (3.23). The eddy diffusivity model also requires characteristic stratification corrections to be defined for each boundary layer.

Above the wave boundary layer, turbulent diffusion is associated with the time average current only. Just as the turbulent momentum flux associated with the wave velocity gradient is negligible above the wave boundary layer, the turbulent concentration flux associated with the wave generated periodic concentration gradient in (4.20) is negligible. Substituting equation (4.20) for the turbulent concentration flux in (4.33), the characteristic stability parameter above the wave boundary layer becomes

$$\frac{z}{L_c} = \frac{\nu_{tc}}{|\vec{u}_{*c}|^4} \sum_n g\,(s_n-1)\,(-\nu_{ts}\,\frac{\partial C_{nm}}{\partial z}) \qquad z > \delta_w \tag{4.36}$$

where ν_{tc} is given by (4.34).

Within the wave boundary layer, turbulent diffusion is associated with the combined wave and current flow. The total turbulent concentration flux is expected to be the same order of magnitude throughout the wave boundary layer due to the enhanced diffusion associated with the wave. Since the neutral eddy viscosity increases linearly with z, the stability parameter is expected to be negligible near the bottom and greatest near the top of the wave boundary layer. The concentration flux associated with the periodic concentration gradient decreases rapidly as the top of the wave boundary layer is approached. Because the stratification correction is greatest in the region where the concentration flux is dominated by the mean concentration gradient, the characteristic stability parameter within the wave boundary layer is assumed to be

$$\frac{z}{L_{cw}} = \frac{\nu_{tcw}}{|\vec{u}_{*cw}|^4} \sum_n g\,(s_n-1)\,(-\nu_{ts}\frac{\partial C_{nm}}{\partial z}) \qquad z < \delta_w \tag{4.37}$$

where ν_{tcw} is given by (4.35).

With characteristic eddy diffusivities now defined for each boundary layer, (4.17) and (4.20) can be substituted for the turbulent fluxes in the governing equations (4.15) and (4.16) to give

$$\frac{\partial \vec{u}_w}{\partial t} + f\,\hat{k} \times \vec{u}_c = -\frac{1}{\rho}\vec{\nabla}(p_c + p_w) + \frac{\partial}{\partial z}\left[\nu_{tm}\frac{\partial}{\partial z}(\vec{u}_c + \vec{u}_w)\right] \tag{4.38}$$

and

$$\frac{\partial C_{np}}{\partial t} + w_w \frac{\partial C_{nm}}{\partial z} - w_{fn} \frac{\partial}{\partial z}(C_{nm} + C_{np}) \tag{4.39}$$

$$- \frac{\partial}{\partial z}\left[\nu_{ts} \frac{\partial}{\partial z}(C_{nm} + C_{np})\right] = 0$$

where the appropriate eddy diffusivities are used for each boundary layer. Because the eddy diffusivities are again constant in time, (4.38) and (4.39) can be averaged over a wave period to give separate wave, current, mean concentration, and periodic concentration equations.

4.1.3 Solution for the mean concentration

Averaging (4.39) over a wave period, the equation governing the mean concentration becomes

$$- \frac{\partial}{\partial z}\left[\nu_{ts} \frac{\partial C_{nm}}{\partial z} + w_{fn} C_{nm}\right] = 0 \tag{4.40}$$

This can be integrated to give at any height z,

$$\nu_{ts} \frac{\partial C_{nm}}{\partial z} + w_{fn} C_{nm} = \text{constant} \tag{4.41}$$

Because both $\partial C_{nm}/\partial z$ and C_{nm} go to zero as z approaches the top of the current boundary layer, the above constant is zero. Substituting for the eddy diffusivity of sediment mass defined by (4.22) and (4.24), equation (4.41) becomes

$$\frac{\partial C_{nm}}{\partial z} + \frac{\gamma + \beta z/L}{\nu_t} w_{fn} C_{nm} = 0 \tag{4.42}$$

Because the second term in (4.42) is always positive, the mean concentration gradient is always negative, requiring the mean concentration for each sediment class to decrease with height.

With the characteristic neutral eddy viscosities defined by (4.34) and (4.35) and the characteristic stability parameters defined by (4.36) and (4.37), the mean concentration equation can be written as

$$\frac{\partial C_{nm}}{\partial z} + \left(\frac{\gamma w_{fn}}{\kappa |u_{*cw}|}\frac{1}{z} + \frac{\beta w_{fn}}{\kappa |u_{*cw}|}\frac{1}{L_{cw}}\right) C_{nm} = 0 \qquad z < \delta_w \tag{4.43}$$

within the wave boundary layer and as

$$\frac{\partial C_{nm}}{\partial z} + \left(\frac{\gamma w_{fn}}{\kappa |u_{*c}|}\frac{1}{z} + \frac{\beta w_{fn}}{\kappa |u_{*c}|}\frac{1}{L_c}\right) C_{nm} = 0 \qquad z > \delta_w \tag{4.44}$$

above the wave boundary layer. The solution to (4.43) and (4.44) for the mean concentration profile within the wave boundary layer is

$$C_{nm}(z) = C_{nm}(z_o)\left(\frac{z}{z_o}\right)^{\left(-\frac{\gamma w_{fn}}{\kappa |u_{*cw}|}\right)} \exp\left(-\frac{\beta w_{fn}}{\kappa |u_{*cw}|}\int_{z_o}^{z}\frac{dz}{L_{cw}}\right) \qquad z < \delta_w \tag{4.45}$$

and above the wave boundary layer is

$$C_{nm}(z) = C_{nm}(\delta_w)\left(\frac{z}{\delta_w}\right)^{\left(-\frac{\gamma w_{fn}}{\kappa |u_{*c}|}\right)} \exp\left(-\frac{\beta w_{fn}}{\kappa |u_{*c}|}\int_{\delta_w}^{z}\frac{dz}{L_c}\right) \qquad z > \delta_w \tag{4.46}$$

In (4.46), the mean concentration at the top of the wave boundary

layer, $C_{nm}(\delta_w)$, can be found by evaluating (4.45) at $z = \delta_w$. In (4.45), the mean concentration at z_o, $C_{nm}(z_o)$, is labelled the reference concentration and is a boundary condition that must be specified independently.

Equations (4.45) and (4.46) for the mean concentration profile consist of a concentration specified at the bottom of each layer multiplied by two factors that decay with height. The first factor gives the mean concentration decay rate in the absence of stratification. It depends on the characteristics of the sediment in class n only and is independent of the amount of sediment in suspension. The second factor gives the mean concentration decay rate associated with suspended sediment induced stratification. This decay rate increases as suspended sediment concentrations increase. Since it depends on the total mean concentration distribution, all the mean concentration equations are coupled through this term. Stratification caused by any sediment class inhibits vertical turbulent transport and therefore affects all sediment classes.

Both decay terms depend on the ratio of the sediment fall velocity to the characteristic shear velocity. If this ratio is small, both decay terms are small and stratification has little influence on the mean concentration profile. Since by definition $w_{fn}/|\vec{u}_{*cw}| < w_{fn}/|\vec{u}_{*c}|$, the decay rates are smaller within the wave boundary layer due to the enhanced turbulent diffusion associated with the wave. This also suggests that stratification effects may be insignificant within the wave boundary layer, a

possibility that will be investigated in the next section.

4.1.4 Simplification of the stability parameter

The characteristic stability parameters can now be simplified using the mean concentration solution. Substituting (4.41) with the constant set equal to zero into (4.36) and (4.37), the characteristic stability parameters can be rewritten as

$$\frac{z}{L_c} = \frac{\nu_{tc}}{|\vec{u}_{*c}|^4} \sum_n g\,(s_n - 1)\, w_{fn}\, C_{nm} \qquad z > \delta_w \tag{4.47}$$

and

$$\frac{z}{L_{cw}} = \frac{\nu_{tcw}}{|\vec{u}_{*cw}|^4} \sum_n g\,(s_n - 1)\, w_{fn}\, C_{nm} \qquad z < \delta_w \tag{4.48}$$

Since the Monin-Obukov length is assumed to be constant in the atmospheric surface layer, the atmospheric stability parameter increases linearly with z. In this case, the neutral eddy viscosity increases linearly with z but the mean concentration decreases. The suspended sediment induced stratification correction therefore may not always increase with z.

For suspended sediment induced stratification to affect the flow, the part of the stability parameter associated with buoyancy, $\sum_n g\,(s_n-1)\, w_{fn}\, C_{nm}$, must be the same order of magnitude or greater than the part associated with production, $|\vec{u}_{*c}|^4/\nu_{tc}$ or

$|u_{*cw}|^4/\nu_{tcw}$. Large suspended sediment concentrations, however, are not sufficient to ensure a large buoyancy term. The buoyancy part of the stability parameter is large only when the fall velocity, mean concentration product is large. This is a physically reasonable result considering that sediment will be mixed uniformly throughout the near bottom region if the fall velocity is very small and little sediment will be in suspension if the fall velocity is very large. Since both of these cases result in density gradients too weak to stratify the near bottom flow, only an intermediate range of sediment fall velocities result in a large stratification correction. For this reason, it is important not only to know how much sediment is in suspension, but what type of sediment is in suspension to determine if a flow is stratified.

Substituting (4.34) and (4.35) for the neutral eddy viscosities and (4.45) and (4.46) for the mean concentrations, the characteristic stability parameters can be written

$$\frac{z}{L_c} = \frac{\kappa |\vec{u}_{*c}| z}{|\vec{u}_{*c}|^4} \cdot \tag{4.49}$$

$$\cdot \sum_n g\,(s_n-1)\, w_{fn}\, C_{nm}\, (\delta_w)\, \left(\frac{z}{\delta_w}\right)^{\left(-\frac{\gamma\, w_{fn}}{\kappa |\vec{u}_{*c}|}\right)} \exp\left(-\frac{\beta\, w_{fn}}{\kappa |\vec{u}_{*c}|} \int_{\delta_w}^{z} \frac{dz}{L_c}\right) \qquad z > \delta_w$$

and

$$\frac{z}{L_{cw}} = \frac{\kappa |\vec{u}_{*cw}| z}{\kappa |\vec{u}_{*cw}|^4} . \tag{4.50}$$

$$\cdot \sum_n g (s_n - 1) w_{fn} C_{nm} (z_o) \left(\frac{z}{z_o}\right)^{\left(-\frac{\gamma w_{fn}}{\kappa |\vec{u}_{*cw}|}\right)} \exp\left(\frac{-\beta w_{fn}}{\kappa |\vec{u}_{*cw}|} \int_{z_o}^{z} \frac{dz}{L_{cw}}\right) \qquad z < \delta_w$$

The vertical structure of the stability parameter above the wave boundary layer is controlled by two factors,

$$z^{\left(1 - \frac{\gamma w_{fn}}{\kappa |\vec{u}_{*c}|}\right)} \quad \text{and} \quad \exp\left(-\frac{\beta w_{fn}}{\kappa |\vec{u}_{*c}|} \int_{\delta_w}^{z} \frac{dz}{L_c}\right) \tag{4.51}$$

If $w_{fn} \geq \kappa |\vec{u}_{*c}|/\gamma$, the contribution to the stability parameter for sediment class n decreases with height. If $w_{fn} < \kappa |\vec{u}_{*c}|/\gamma$, however, the contribution to the stability parameter for sediment class n increases with height until the exponential decay factor limits the increase. Since the exponential decay factor depends on the integral of the stability parameter over depth, the exponential decay rate associated with sediment class n stays large once it becomes large. The contribution to the stability parameter for each sediment class n therefore is self-limiting.

The vertical structure of the stability parameter within the wave boundary layer is also controlled by two factors

$$z^{\left(1 - \frac{\gamma w_{fn}}{\kappa |\vec{u}_{*cw}|}\right)} \quad \text{and} \quad \exp\left(-\frac{\beta w_{fn}}{\kappa |\vec{u}_{*cw}|} \int_{z_o}^{z} \frac{dz}{L_{cw}}\right) \tag{4.52}$$

At $z = z_o$, the stability parameter is negligible for any case of practical interest because z is so small. The stability parameter remains negligible in the wave boundary layer if $w_{fn} \geq \kappa |\vec{u}_{*cw}|/\gamma$. For $w_{fn} < \kappa |\vec{u}_{*cw}|/\gamma$, the stability parameter increases with z until limited by the exponential decay term. The maximum value of the stability parameter within the wave boundary layer therefore can be estimated by ignoring the exponential decay factor and evaluating the stability parameter at the top of the wave boundary layer for values of $w_{fn} < \kappa |\vec{u}_{*cw}|/\gamma$,

$$\left(\frac{z}{L_{cw}}\right)_{max} < \frac{\kappa |\vec{u}_{*cw}| \delta_w}{|\vec{u}_{*cw}|^4} \sum_n g (s_n - 1) w_{fn} C_{nm} (z_o) \left(\frac{\delta_w}{z_o}\right)^{\left(-\frac{\gamma w_{fn}}{\kappa |\vec{u}_{*cw}|}\right)} \quad (4.53)$$

Taking the derivative of (4.53) with respect to w_{fn} and setting the result equal to zero, the fall velocity that has the largest contribution to the stability parameter is found to be

$$w_{fn} = \frac{\kappa}{\gamma} |\vec{u}_{*cw}| \frac{1}{\ln \delta_w/z_o} \quad (4.54)$$

where the inequality $\delta_w > e\, z_o$ must be satisfied. If all the sediment is assumed to have the fall velocity given by (4.54), an estimate of the maximum stability parameter in the wave boundary layer is

$$\left(\frac{z}{L}\right)_{cw\ max} < \frac{\kappa^2}{\gamma}(s_n-1)\ \frac{\delta_w g}{|\vec{u}_{*cw}|^2}\ C_{nm}(z_o)\ \frac{1}{\ln\frac{\delta_w}{z_o}}\ \left(\frac{\delta_w}{z_o}\right)^{\left(\frac{-1}{\ln\frac{\delta_w}{z_o}}\right)} \tag{4.55}$$

For a typical case on the continental shelf when suspended sediment induced stratification is expected to be important, $C_{nm}(z_o) = 0.001$, $|\vec{u}_{*cw}| = 5$ cm/sec, $\delta_w = 10$ cm, $z_o = 1$ cm, $s = 2.65$, $g = 980$ cm/sec, $\kappa = 0.4$, and $\gamma = 0.74$, the maximum stability parameter in the wave boundary layer is

$$\left(\frac{z}{L}\right)_{cw\ max} < 0.012 \tag{4.56}$$

Since the stratification correction, $\beta\ z/L$ where $\beta = 4.7$, must be O (1) to effect the turbulent fluxes, suspended sediment induced stratification is expected to have a negligible effect in the wave boundary layer. The stratification correction therefore will be ignored within the wave boundary layer. Equation (4.45) for the mean sediment concentration in the wave boundary layer then can be rewritten as

$$C_{nm}(z) = C_{nm}(z_o)\left(\frac{z}{z_o}\right)^{\left(-\frac{\gamma w_{fn}}{\kappa |\vec{u}_{*cw}|}\right)} \tag{4.57}$$

4.1.5 Solution for the wave

Averaging equation (4.38) over a wave period and subtracting the

result from the original equation gives the equation for the wave as

$$\frac{\partial \vec{u}_w}{\partial t} = -\frac{1}{\rho} \nabla \vec{p}_w + \frac{\partial}{\partial z} \left(\nu_{tm} \frac{\partial \vec{u}_w}{\partial z} \right) \tag{4.58}$$

Above the wave boundary layer, the turbulent momentum flux associated with the wave is negligible and the resulting equation for the wave is (3.28). Within the wave boundary layer, the stratification correction is negligible and the resulting equation for the wave is (3.31). Suspended sediment induced stratification therefore does not effect the wave directly. The solution for the wave velocity profile is the same as the neutral solution given by (3.29) and (3.43). The wave boundary layer height is again given by (3.45) and the combined wave and current friction factor by (3.50). Using equations (4.9) and (3.29), the vertical wave velocity above the wave boundary layer is found to be

$$w_w = |\vec{u}_b| \sinh kz \cos (k_x x + k_y y - \omega t) \tag{4.59}$$

4.1.6 Solution for the periodic concentration

Subtracting (4.40) from (4.39), the equation for the periodic concentration becomes

$$\frac{\partial C_{np}}{\partial t} + w_w \frac{\partial C_{nm}}{\partial z} - w_{fn} \frac{\partial C_{np}}{\partial z} - \frac{\partial}{\partial z} \left(\nu_{ts} \frac{\partial C_{np}}{\partial z} \right) = 0 \tag{4.60}$$

The turbulent diffusion associated with the periodic concentration is negligible above the wave boundary layer and (4.60) can be written

$$\frac{\partial C_{np}}{\partial t} + w_w \frac{\partial C_{nm}}{\partial z} - w_{fn} \frac{\partial C_{np}}{\partial z} = 0 \qquad z > \delta_w \tag{4.61}$$

Away from the wave boundary layer, w_w is the same order of magnitude or greater than w_{fn}. If it is assumed that $\partial C_{np}/\partial z \ll \partial C_{nm}/\partial z$, equation (4.61) is approximately

$$\frac{\partial C_{np}}{\partial t} + w_w \frac{\partial C_{nm}}{\partial z} = 0 \qquad z \gg \delta_w \tag{4.62}$$

Equation (4.62) states that the periodic concentration far above the wave boundary layer is caused by advection of the mean concentration gradient by the vertical wave velocity. Because C_{nm} is constant in time, the solution for the periodic concentration away from the wave boundary layer is

$$C_{np} = A_b \sinh kz \frac{\partial C_{nm}}{\partial z} \sin (k_x x + k_y y - \omega t) \qquad z \gg \delta_w \tag{4.63}$$

where (4.59) was used for w_w. Taking the derivative of (4.63) with respect to z, the periodic concentration gradient becomes

$$\frac{\partial C_{np}}{\partial z} = \tag{4.64}$$

$$(A_b\, k \cosh kz \frac{\partial C_{nm}}{\partial z} + A_b \sinh kz \frac{\partial^2 C_{nm}}{\partial z^2}) \sin (k_x x + k_y y - \omega t) \quad z \gg \delta_w$$

Equations (4.63) and (4.64) can be scaled for both $kz \ll 1$ and $kz \sim O(1)$.

When $kz \ll 1$, it follows that $\sinh kz \sim 0\ (z/\lambda_w)$ and $\partial/\partial z \sim 0\ (1/z)$. When $kz \sim 0\ (1)$, it follows that $\sinh kz \sim 0\ (1)$ and $\partial/\partial z \sim 0\ (1/\lambda_w)$. Because $\cosh kz \sim 0\ (1)$ and $A_b \sim 0\ (u_b T)$ in either case, scaling (4.62) and (4.63) gives

$$C_{np} \sim 0\ \left(\frac{u_b}{c_w} C_{nm}\right) \qquad \text{and} \qquad \frac{\partial C_{np}}{\partial z} \sim 0\ \left(\frac{u_b}{c_w} \frac{\partial C_{nm}}{\partial z}\right) \tag{4.65}$$

where c_w is the wave phase velocity defined by (4.14). Since the linearization assumptions require $u_b \ll c_w$, it follows that $C_{np} \ll C_{nm}$, $\partial C_{np}/\partial z \ll \partial C_{nm}/\partial z$, and (4.62) is valid for $w_w \geq 0\ (w_{fn})$.

Near the wave boundary layer, it is possible that $w_w \ll w_{fn}$. If both the periodic and the mean concentration gradients are the same order of magnitude, equation (4.61) becomes

$$\frac{\partial C_{np}}{\partial t} - w_{fn} \frac{\partial C_{np}}{\partial z} = 0 \qquad z \geq \delta_w \tag{4.66}$$

This equation requires the sediment to fall out of suspension until the periodic concentration gradient is small and $w_{fn}\ \partial C_{np}/\partial z \sim 0\ (w_w\ \partial C_{nm}/\partial z)$. The periodic concentration gradient therefore is always much smaller than the mean concentration gradient above the wave boundary layer.

In the wave boundary layer, the vertical wave velocity is negligible, the stratification correction can be neglected, and equation (4.60) can be rewritten

$$\frac{\partial C_{np}}{\partial t} - \frac{\partial}{\partial z}\left(\frac{\nu_t}{\gamma} \frac{\partial C_{np}}{\partial z} + w_{fn} C_{np}\right) = 0 \qquad z < \delta_w \tag{4.67}$$

Whereas the periodic concentration above the wave boundary layer was dominated by vertical advection of the mean concentration gradient by the wave, the periodic concentration within the wave boundary layer is associated with turbulent diffusion and is not coupled directly to the mean concentration. Suspended sediment induced stratification therefore has no direct influence on the periodic concentration, though it does influence the periodic concentration above the wave boundary layer indirectly through the mean concentration.

The boundary condition for equation (4.67) at the bottom is

$$C_{np}(z_o) = C_n(z_o) - C_{nm}(z_o) \tag{4.68}$$

where $C_n(z_o)$ is the instantaneous reference concentration and $C_{np}(z_o)$ is the periodic reference concentration. Because $C_n(z_o)$ is expected to depend on the absolute value of the instantaneous shear stress, $C_{np}(z_o)$ does not behave as a simple periodic function and (4.67) must be solved numerically. The order of magnitude of the periodic concentration in the wave boundary layer still can be established from (4.67) and (4.68). Since all terms in (4.68) are the same order of magnitude, periodic and mean concentrations are expected to be the same order of magnitude near the bed. Near the top of the wave boundary layer, however, the solution satisfying (4.67) and (4.61) must approach each other, requiring periodic concentrations to be much less than mean concentrations for $z > \delta_w$.

In the momentum equation, the nonlinear convective accelerations

where neglected compared to the local acceleration in the equation for the wave,

$$\vec{u}_w \cdot \vec{\nabla}\ \vec{u}_w + w_w \frac{\partial \vec{u}_w}{\partial z} << \frac{\partial \vec{u}_w}{\partial t} \tag{4.69}$$

To show that the convective accelerations do not contribute to the current equation, these terms can be averaged over a wave period. Since $\vec{u}_w$ is 90° out of phase with $\vec{\nabla}\vec{u}_w$ and w_w is 90° out of phase with $\partial u_w/\partial z$, the nonlinear convective accelerations average to zero over a wave period. Similarly, the nonlinear periodic terms in the concentration equation were neglected compared to the time derivative of the periodic concentration

$$\vec{u}_w \cdot \vec{\nabla}\ C_{pn} + w_w \frac{\partial C_{pn}}{\partial z} << \frac{\partial C_{pn}}{\partial t} \tag{4.70}$$

The nonlinear periodic terms also can be averaged over a wave period to see if they contribute to the mean concentration equation. For $z > \delta_w$ and $w_w \geq 0$ (w_{fn}), the solution for the wave and the periodic concentration indicate that $\vec{u}_w$ is 90° out of phase with $\vec{\nabla} C_{np}$ and w_w is 90° out of phase with $\partial C_{np}/\partial z$. The nonlinear periodic terms therefore average to zero in this region.

For $w_w << w_{fn}$ or $z < \delta_w$, an explicit solution for the periodic concentration was not found. For these cases, simple scaling arguments can be used to estimate the order of magnitude of the nonlinear terms. Since the continuity equation was used in Section 4.1.1

to show that the nonlinear periodic terms are the same order of magnitude, only $w_w \partial C_{np}/\partial z$ will be compared to $w_f \partial C_{nm}/\partial z$ in the mean concentration equation. The case being considered above the wave boundary layer is $w_w << w_{fn}$. Since $\partial C_{np}/\partial z << \partial C_{nm}/\partial z$ in this region, it follows that

$$w_w \frac{\partial C_{np}}{\partial z} << w_{fn} \frac{\partial C_{nm}}{\partial z} \tag{4.71}$$

In the wave boundary layer, w_w decreases from a very small value at the top to zero at the bed, while the periodic concentration gradient increases from a very small value at the top to a value the same order of magnitude as the mean concentration gradient at the bed. Near the top of the wave boundary layer, $\partial C_{np}/\partial z << \partial C_{nm}/\partial z$, so (4.71) is satisfied. Near the bed $\partial C_{np}/\partial z \sim O(\partial C_{nm}/\partial z)$, but $w_w > o$, so (4.71) again is satisfied. The nonlinear periodic terms therefore do not contribute to the mean concentration equation throughout the bottom boundary layer.

4.1.7 Solution for the current

Averaging (4.38) over a wave period, the governing equation for the current is found to be

$$f \hat{k} \times \vec{u}_c = -\frac{1}{\rho} \vec{\nabla} p_c + \frac{\partial}{\partial z} \left(\nu_{tm} \frac{\partial \vec{u}_c}{\partial z} \right) \tag{4.72}$$

In the constant stress layer for the current, the turbulent stress term in parenthesis again is equal to the time average shear stress associated with the current

$$\frac{\nu_t}{1 + \beta \frac{z}{L}} \quad \frac{\partial \vec{u}_c}{\partial z} = |\vec{u}_{*c}| \; \vec{u}_{*c} \tag{4.73}$$

where (4.21) and (4.23) have been substituted for ν_{tm}. Using (4.34) and (4.35) for the neutral eddy viscosity and (4.36) and (4.37) for the stability parameter, (4.73) can be written above the wave boundary layer as

$$\frac{\partial \vec{u}_c}{\partial z} = \frac{\vec{u}_{*c}}{\kappa z} \left(1 + \beta \frac{z}{L_c} \right) \qquad z > \delta_w \tag{4.74}$$

and within the wave boundary layer as

$$\frac{\partial \vec{u}_c}{\partial z} = \frac{|\vec{u}_{*c}|}{|\vec{u}_{*cw}|} \frac{\vec{u}_{*c}}{\kappa z} \qquad z < \delta_w \tag{4.75}$$

where the stratification correction has been neglected within the wave boundary layer. For a given $|\vec{u}_{*c}|$, stratification increases the current shear above the wave boundary layer. The current within the wave boundary layer, however, is not affected directly by stratification.

Integrating equation (4.75) and applying the no-slip boundary condition at z_o, the solution for the current velocity in the wave boundary layer is the same as in the neutral case,

$$\vec{u}_c = \frac{\vec{u}_{*c}}{\kappa} \frac{|\vec{u}_{*c}|}{|\vec{u}_{*cw}|} \ln \frac{z}{z_o} \qquad z < \delta_w \tag{4.76}$$

Integrating (4.74) and applying the apparent no-slip boundary condition at z_{oc}, the solution for the current velocity above the wave boundary layer is

$$\vec{u}_c = \frac{\vec{u}_{*c}}{\kappa} \left(\ln \frac{z}{z_{oc}} + \beta \int_{\delta_w}^{z} \frac{dz}{L_c}\right) \qquad z > \delta_w \tag{4.77}$$

By matching the current velocities at $z = \delta_w$, the equation for the apparent bottom roughness felt by the current above the wave boundary layer,

$$\frac{z_{oc}}{z_o} = \left(\frac{\delta_w}{z_o}\right)^{(1 - |\vec{u}_{*c}| / |\vec{u}_{*cw}|)} \tag{4.78}$$

is the same as in the neutral case. The current velocity profile is coupled to the mean sediment concentration through the stability parameter, while the mean concentration profile is coupled to the current through the characteristic shear velocities. The current and mean concentration equations therefore must be solved simultaneously in the bottom boundary layer.

4.1.8 Solution procedure

The stratified near bottom model solution procedure is similar to the method used for the neutral near bottom model. Because the stratified model includes the effect of buoyancy, the acceleration of gravity must be included as an input variable. Again, using $|\vec{u}_b|$ and A_b as master velocity and length scales, the basic dimensionless input parameters for the stratified model are

$$\frac{|\vec{u}_r|}{|\vec{u}_b|}, \frac{z_r}{A_b}, \bar{\phi}_c, \frac{k_b}{A_b}, \text{ and } \frac{g\,A_b}{|\vec{u}_b|^2} .$$

The new input parameter is just the acceleration of gravity divided by the potential flow solution for the local wave acceleration at the bottom. Additional dimensionless input parameters required for each sediment class n are

$$s_n, S_{*n}, \frac{[(s_n-1)\,gd_n]^{1/2}}{|\vec{u}_b|}, \text{ and } C_{nm}(z_o) .$$

The iterative procedure used to solve the stratified near bottom model equations is as described in Section 3.1.5, except that (4.77) instead of (3.59) is used to calculate the current velocity above the wave boundary layer. To evaluate (4.77), the stability parameter profile must be evaluated from (4.47) and (4.46). First the sediment fall velocity w_{fn} is found from S_{*n} and Figure 4.1, and the mean concentration at the top of the wave boundary layer $C_{nm}(\delta_w)$ is calculated from (4.57). It is initially assumed that $z/L_c = 0$ and (4.46) is solved for the mean concentration profile $C_{nm}(z)$. A new stability parameter profile then can be found using $C_{nm}(z)$ and (4.47). The process is repeated until the correct stability parameter profile is established. If $z_r > \delta_w$, equation (4.77) for the current above the wave boundary layer can be evaluated at z_r and the result compared to the known current at z_r. When the

proper value of $|\vec{u}_a|/|\vec{u}_b|$ is finally found, the wave velocity profile is given be (3.43) and (3.29), the near bottom current velocity profile by (4.76) and (4.77), and the near bottom concentration profiles by (4.57) and (4.46) for $z < \delta_w$ and $z > \delta_w$ respectively.

4.2 Sediment Reference Concentration Model

The solution for the velocity and sediment concentration profiles in Section 4.1 require independently specified values of the physical bottom roughness k_b and the mean reference concentrations $C_{nm}(z_o)$. The bottom roughness model discussed in Section 3.2 can be used to predict k_b. A mathematical model to predict $C_{nm}(z_o)$ is developed in this section by generalizing a model proposed for steady flow to combined wave and current flows.

4.2.1 Combined wave and current reference concentration

Smith and McLean (1977) suggest that the steady flow reference concentration at z_o be written for each sediment class as

$$C_{ns}(z_o) = C_{nb}\frac{\gamma_o S_n}{1 + \gamma_o S_n} \tag{4.79}$$

where $C_{ns}(z_o)$ is the steady flow reference concentration for class n, C_{nb} is the maximum allowable concentration taken as the bed concentration of sediment in class n, γ_o is a constant of order 10^{-3} that must be determined from data, and S_n is the normalized excess shear stress for class n. S_n is defined as

$$S_n = \frac{\vec{\tau}_b - \vec{\tau}_{cn}}{\tau_{cn}} \tag{4.80}$$

where τ_b is the magnitude of the boundary shear stress and τ_{cn} is the magnitude of the critical shear stress for initiation of motion for sediment in class n. The form of (4.79) was chosen so that reference concentrations behave reasonably for a wide range of shear stresses. When S_n is small, the reference concentration increases linearly with the normalized excess shear stress. As $S_n \to \infty$, however, the reference concentration is limited to not exceed the bed concentration. Because the maximum allowable concentration for all size classes is assumed to be the bed concentration, (4.79) neglects the effect of armoring in sediment mixtures. Armoring of the bed by the course sediment in some cases can reduce the amount of fine sediment available for suspension and further limit the maximum allowable concentration.

Grant and Madsen (1982) have shown that the sediment response time, $O(d/u_*)$, is much less than the wave period for most cases of interest on the continental shelf. The unsteady combined wave and current flow therefore appears quasi-steady to the sediment particles. Madsen and Grant (1976) have demonstrated that steady flow sediment transport relationships can be used to predict instantaneous sediment transport rates in unsteady oscillatory flow if the shear stress is taken as the instantaneous skin friction. Following this approach, it

is proposed that the instantaneous reference concentration at z_o in a combined wave and current flow be defined as

$$C_n(z_o) = C_{nb}\frac{\gamma_o S'_n}{1+\gamma_o S'_n} \qquad S'_n > 0$$
$$C_n(z_o) = 0 \qquad S'_n \leq 0 \tag{4.81}$$

S'_n is the instantaneous normalized excess skin friction defined as

$$S'_n = \frac{|\vec{\tau}'_{bn}| - |\vec{\tau}_{cn}|}{|\vec{\tau}_{cn}|} = \frac{\psi'_n}{\psi_{cn}} - 1 \tag{4.82}$$

where $|\vec{\tau}'_{bn}|$ is the magnitude of the instantaneous skin friction for class n, $|\vec{\tau}_{cn}|$ is the magnitude of the critical shear stress for initiation of motion for sediment in class n, ψ'_n is the skin friction component of the instantaneous Shields parameter based on skin friction for class n, and ψ_{cn} is the critical Shields parameter for class n. The instantaneous reference concentration is then averaged over a wave period to find the mean reference concentration $C_{nm}(z_o)$

$$C_{nm}(z_o) = \frac{1}{2\pi}\int_0^{2\pi} C_n(z_o)\, d\theta \tag{4.83}$$

4.2.2 Determination of the reference concentration constant

To use (4.83) to estimate sediment reference concentrations, the reference concentration constant γ_o must first be determined from data. The best method to determine if (4.83) is a reasonable form and to calculate γ_o is to match predicted sediment concentration

profiles to profiles measured in a combined wave and current flow over a non-bioturbated moveable bed. This should be done for different types of uniform sediment to minimize errors in the initiation of motion criteria and the suspended sediment concentration measurements and for mixtures of sediment to investigate the effect of armoring on the sediment reference concentration. Because no data of this type exists, two alternate approaches were used to determine the reference concentration constant. The first method involves using instantaneous sediment concentrations and velocities in the near bed transport layer to estimate sediment transport rates and matching the results to oscillatory flow transport rates measured by Kalkanis (1964) and Abou-Seida (1965) in the laboratory. The second method is to match predicted sediment concentrations to concentrations measured by Cacchione and Drake (1982) 2 meters above a highly bioturbated sandy silt bottom in a combined wave and current flow on the continental shelf.

In the experimentss performed by Kalkanis (1964) and Abou-Sedia (1965), a plate of sediment with a sediment trap in the center was oscillated sinusoidally. Equal amounts of sediment were caught in the trap during the forward and backward motion of the plate. Using the experimental data, Madsen and Grant (1976) computed the average volumetric sediment transport rate defined as

$$q_s = \frac{Q_s}{\rho_s \, g \, bt} \tag{4.84}$$

where Q_s is the total dry weight of the sediment caught in the trap, ρ_s is the sediment density, g is the acceleration of gravity, b is the width of the sediment trap, and t is the total time the trap was in motion. Madsen and Grant (1976) then developed expressions that relate the maximum Shields parameter based on skin friction ψ'_m to the average dimensionless sediment transport function defined as

$$\phi = \frac{q_s}{w_f d} \tag{4.85}$$

where w_f is the particle fall velocity and d is the particle diameter. The data collected by Kalkanis (1964) and Abou-Seida (1965) and analyzed by Madsen and Grant (1976) is plotted in Figure 4.2.

Assuming that the sediment caught by the trap was transported primarily as bedload, it is proposed that the average volumetric transport rate can also be expressed as

$$q_s = \frac{1}{2\pi} \int_0^{2\pi} C_T \, |\vec{u}_T| \, h_T \, d\theta \tag{4.86}$$

where C_T and $\vec{u}_T$ are the instantaneous sediment concentration and velocity in the near bed transport layer, h_T is the instantaneous height of the layer, and the average is taken over a wave period. Because u_T changes direction for $\pi < \theta < 2\pi$ so that the net transport is zero over wave period, the magnitude of $\vec{u}_T$ is used in (4.86) to calculate the amount of sediment caught by the trap during both the forward and backward parts of the cycle. Since z_o is

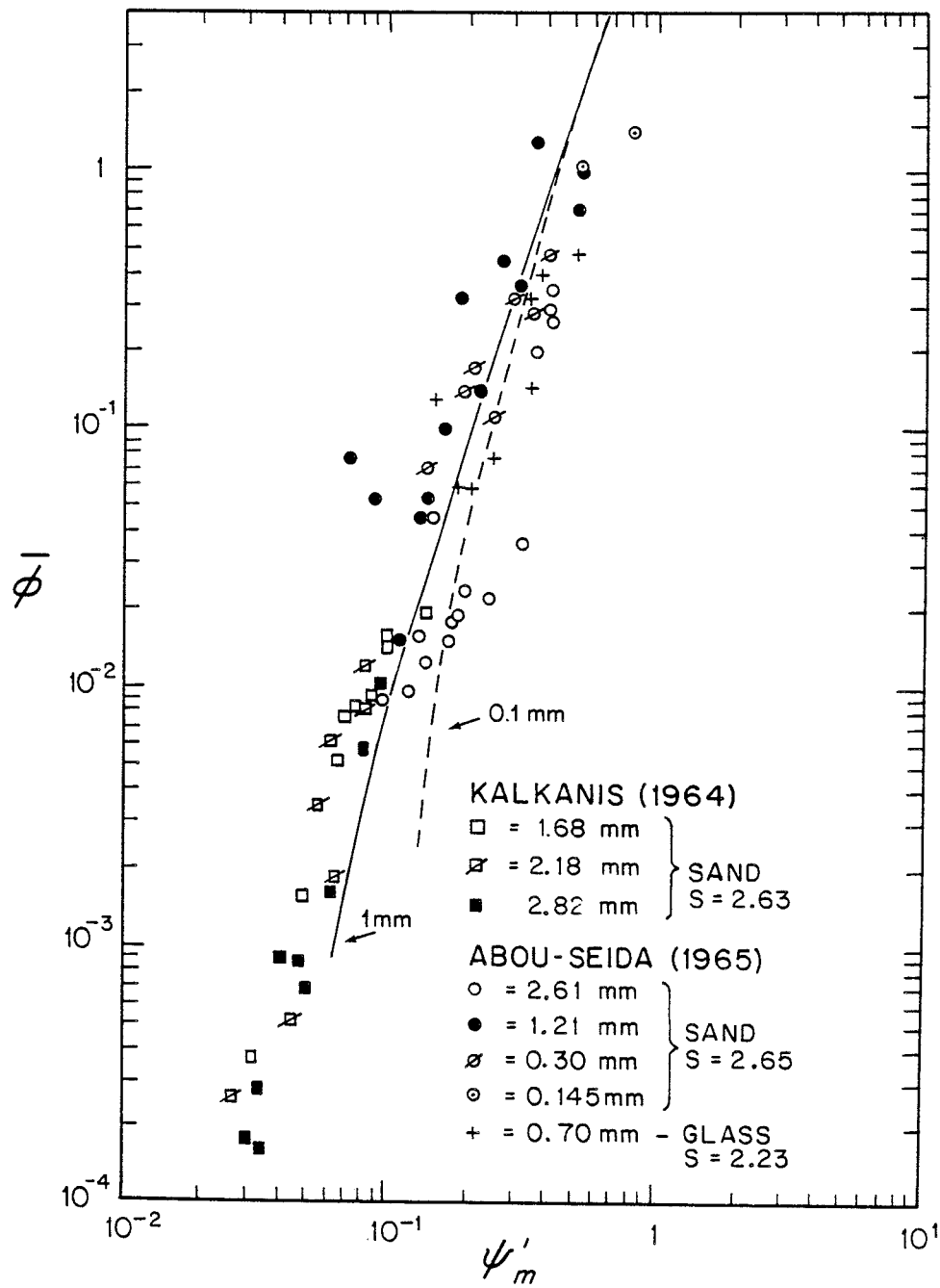

FIGURE 4.2
Dimensionless sediment transport function $\bar{\phi}$ as a function of ψ'_m calculated from (4.85) and (4.86) (for d = 1 mm and d = 0.1 mm with s = 2.65) compared to the data of Kalkanis (1964) and Abou-Seida (1965).

within the near bed transport layer, the instantaneous reference concentration given by (4.81) will be used to estimate C_T. Expressions for $\vec{u}_T$ and h_T are derived as Grant and Madsen (1982) derived (3.72) and (3.73) for the maximum particle velocity and layer height.

Grant and Madsen (1982) derived an expression for the maximum horizontal particle velocity in the near bed transport layer by considering the balance between the maximum horizontal inertia, drag, and friction forces on a sediment particle. Neglecting the inertia force compared to the drag force, equation (3.72) for the maximum particle velocity is found by balancing the maximum drag force with the maximum friction force. Because the inertia force can be neglected compared to the instantaneous drag force over most of the wave cycle, an expression for the instantaneous particle velocity can be found by balancing the instantaneous drag force with the instantaneous friction force. The resulting expressions for $\vec{u}_T$ and h_T are identical to (3.72) and (3.73) with the maximum Shields parameter ψ'_m replaced by the instantaneous Shields parameter ψ' based on skin friction. Though these expressions for $\vec{u}_T$ and h_T are not expected to be valid as the oscillatory particle velocity goes through zero and the inertia force dominates the drag force, the sediment concentration is zero once $\psi' < \psi_c$ and the exact forms of $\vec{u}_T$ and h_T are not required. Using equation (4.86), the calculated dimensionless sediment transport function agrees best with the data of Kalkanis (1964) and Abou-Seida (1965) when the reference

concentration constant γ_o is approximately 0.003. Assuming γ_o = 0.003 and s = 2.65, the dimensionless sediment transport function is plotted in Figure 4.2 for d = 0.1 mm and d = 1.0 mm. The agreement with the data suggests that (4.81) is a reasonable form for the instantaneous reference concentration.

The reference concentration constant can also be determined by matching the predicted sediment concentrations with those measured by Cacchione and Drake. A major problem with this method is that only concentrations 2 meters above the bed, rather than concentration profiles, where measured. Because sediment concentrations can decay by orders of magnitude between z_o and 2 meters, a small error in the concentration measurement at 2 meters can result in a large error in the predicted reference concentration. The measured sediment concentrations at 2 meters were dominated by the fine silts, so little is known about the other sediment classes. Because the fall velocity of the fine silt is so small, the silt concentration may not be in local equilibrium and may be dominated by advection. As described by Grant et al (1982), not only is the value of the critical Shields parameter for a very fine non-cohesive sediment in question, but bioturbation can increase the critical Shields parameter by as much as a factor of 2. When a critical Shields parameter twice the value given by Shields diagram for a non-cohesive sediment was used, γ_o was found to be approximately 0.0005. Because the fine sand could have armored the bed and inhibited the suspension of silt, the calculated value of γ_o would be too low if armoring had occurred.

With the many uncertainties in the data, this value of γ_0 at best can be considered an order of magnitude estimate and is probably too low. The analysis of the data collected by Cacchione and Drake that led to this estimate is discussed in Chapter 7.

In summary, two different methods determined that the reference concentration constant is probably in the range of 0.0005 to 0.003. The stratified wave and current model has been run with the reference concentration model for a range of reference concentration constants larger than $0.0005 \leq \gamma_0 \leq 0.003$. It was found that an order of magnitude difference in γ_0 can significantly change the velocity profiles while factors of 2-3 difference in γ_0 cause very little change in the velocity profiles. An average value of $\gamma_0 = 0.002$ therefore will be adopted for use in the reference concentration model until better data is available.

4.2.3 Solution procedure

The stratified near bottom model requires mean reference concentrations to be specified for each sediment class. Since these concentrations usually are not known, they can be calculated using the reference concentration model. Additional dimensionless input parameters required for each sediment class n are the relative sediment grain diameter d_n/A_b, which is necessary to calculate skin friction, and the concentration of sediment in the bed C_{nb}. Using (3.50) to find the skin friction factor for each sediment class, the instantaneous skin friction for each class τ'_{bn} can be

found from (3.10). The instantaneous normalized excess skin friction S'_n is given by (4.82) and the instantaneous reference concentration by (4.81). The mean reference concentration is found by averaging (4.81) over a wave period as in (4.83).

4.3 Near Bottom Model Runs

The effects of surface waves and a moveable sediment bed on the near bottom flow field are illustrated in this section using the models discussed in Chapters 3 and 4. The neutral near bottom model is used to calculate the neutral current velocity profile and the stratified near bottom model is used to calculate the stratified current and the suspended sediment concentration profiles. Ripple geometry, height of the near bed transport layer, and the associated bottom roughness are calculated by the physical bottom roughness model. The mean sediment concentration at z_o is calculated by the reference concentration model. To use these models, several wave, current, and bottom conditions must be specified. Since the physical bottom roughness model has not been generalized to sediment mixtures, the following examples are run for uniform sediments.

For the examples to be discussed here, the input conditions are taken from typical data collected by Cacchione and Drake during a winter storm on the northern California continental shelf. The wave orbital velocity and excursion amplitude at the bottom are assumed to be $|\vec{u}_b| = 50$ cm/sec and $A_b = 120$ cm, corresponding roughly to a 15 second wave with a height of 6.5 meters in 100 meters of water. The

specified current speed and direction are taken as $|\vec{u}_r|$ = 50 cm/sec and $\bar{\phi}_c = 0^\circ$ at z_r = 100 cm above the bottom. The bottom sediment is assumed to be fine quartz sand with a grain diameter d = 0.01 cm, a relative density s = 2.65, and a porosity of 0.4. The kinematic viscosity of seawater and the acceleration of gravity are taken as $\nu = 0.013$ cm^2/sec and g = 980 cm/sec^2.

With this information, all the input parameters necessary to run the models can be specified. The resulting neutral current velocity and stratified current velocity profiles calculated by the models are compared in Figure 4.3 and the suspended sediment concentration profile is shown in Figure 4.4. The kink in the profiles corresponds to the top of the wave boundary layer. In the wave boundary layer, the increased vertical turbulent transport associated with the combined wave and current decreases both the current shear and the suspended sediment concentration vertical decay rate. Above the wave boundary layer, vertical turbulent transport is associated with the enhanced current only, so the current shear and the vertical decay rate for suspended sediment increase. Suspended sediment induced stratification, which acts to inhibit vertical turbulent transport, also increases the current shear and sediment concentration decay rate. Important model parameters for both the neutral and the stratified model runs are listed in Table 4.1 for comparison.

Because the maximum Shields parameter based on skin friction ψ'_m is above the critical value for initiation of motion, sediment is transported and ripples form. The contribution to the physical

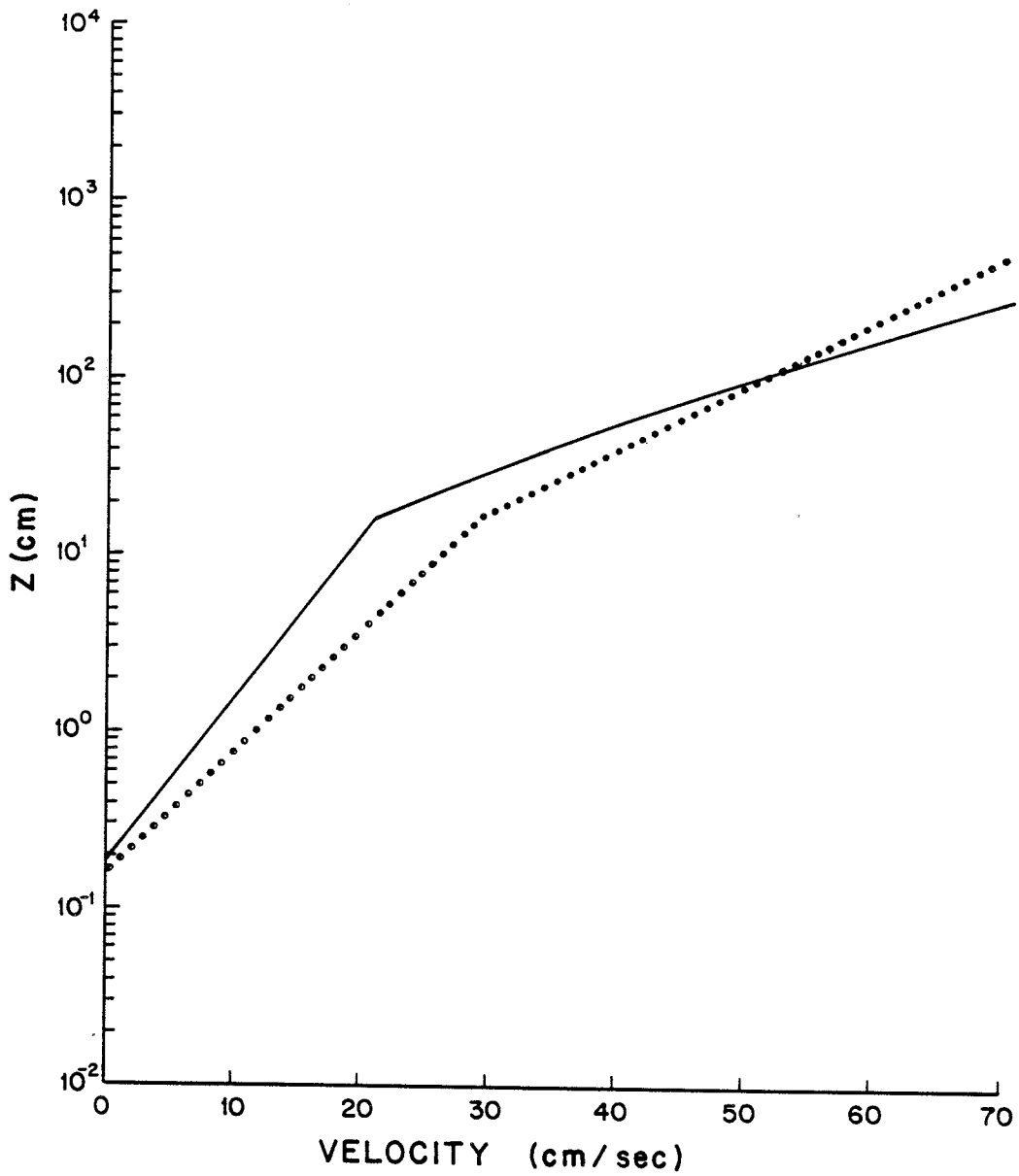

FIGURE 4.3
Current velocity profiles for the fine sand, medium wave case, predicted by the stratified (solid line) and the neutral (dotted line) near bottom models.

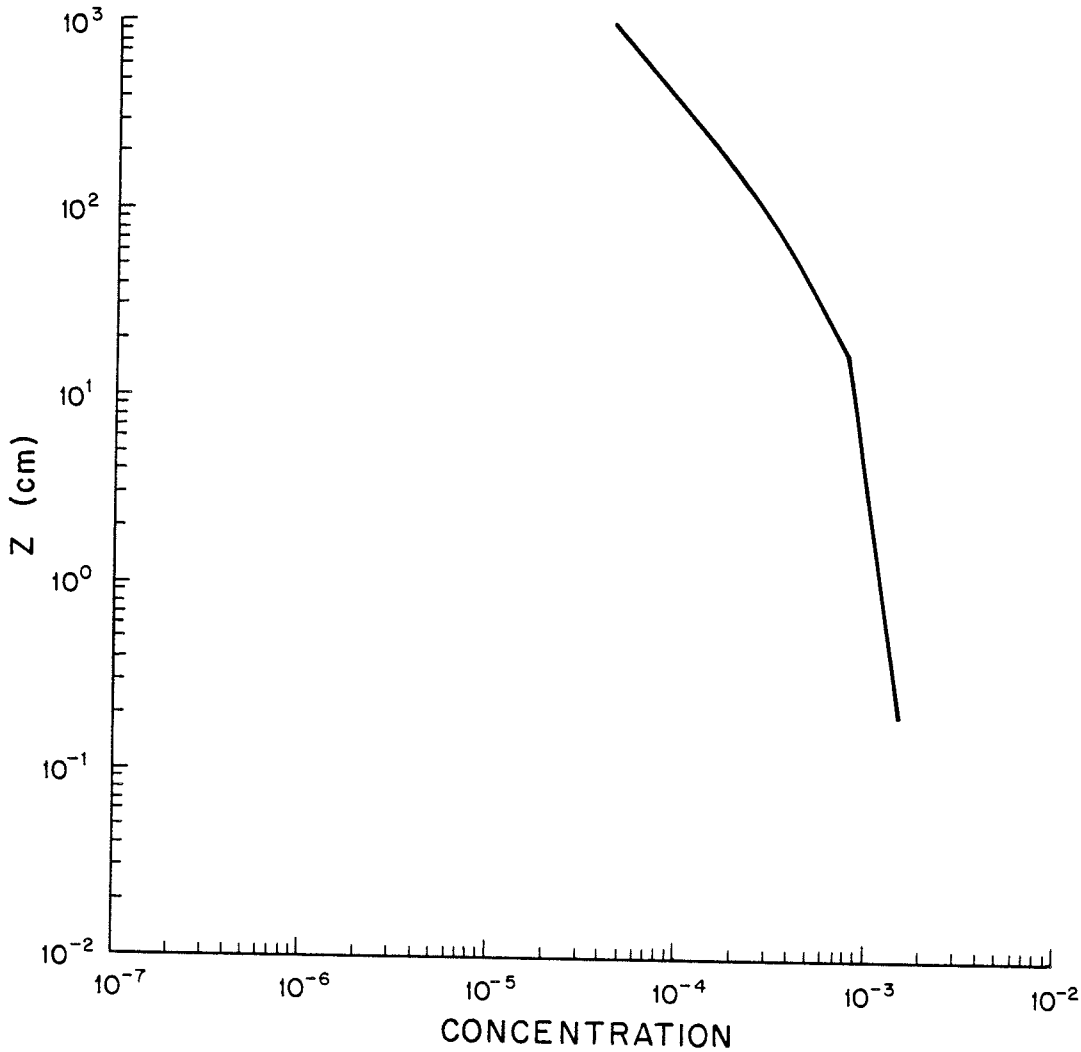

FIGURE 4.4
Sediment concentration profile for the fine sand, medium wave case, predicted by the stratified near bottom model.

TABLE 4.1: Near Bottom Model Parameters: Medium Wave

	Silt		Fine Sand		Medium Sand	
	Neutral	Stratified	Neutral	Stratified	Neutral	Stratified
δ_w(cm)	13.6	13.5	16.8	16.4	34.9	34.5
z_{oc}(cm)	.611	.624	1.41	2.06	10.4	10.9
z_o(cm)	0.0500	0.0493	0.162	0.196	2.86	2.88
u_{*c}(cm/sec)	3.92	3.84	4.69	4.01	8.84	8.30
u_{*cw}(cm/sec)	7.09	7.02	8.78	8.56	18.2	17.9
ψ'_m/ψ_c	4.49	4.41	6.46	5.52	5.39	5.14
ψ'_m/ψ_B	12.4	12.2	4.19	3.58	0.820	0.782
k_{bB}(cm)	0.249	0.260	2.93	4.34	83.6	84.3
k_{bT}(cm)	1.25	1.22	1.91	1.53	2.29	2.14
$C_{nm}(z_o)(x10^{-3})$		1.06		1.44		1.30

bottom roughness from ripples and near bed transport are both significant because ψ'_m is above the breakoff point and ripples are partially washed out. The total physical bottom roughness is a factor of 500 greater than the sediment grain diameter. Due to the wave-current interaction, the apparent bottom roughness experienced by the current above the wave boundary layer is a factor of 10 greater then the physical bottom roughness. If the wave-current interaction is neglected, the moveable bed effects are neglected, and the flat bed bottom roughness is taken as the sediment grain diameter, the roughness length above the wave boundary layer in this case is under-predicted by a factor of 5000.

For a given shear velocity, stratification increases the current shear. To match the specified current velocity at z_r = 100 cm, lower shear velocities are required for the stratified case. Stratification therefore reduces the current velocity below z_r. Because the shear velocities are lower, the skin friction is lower and ψ'_m is closer to the breakoff point. Sediment transport is reduced and the ripples are eroded less. Because the ripple roughness increases more than the near bed transport roughness decreases, the total physical bottom roughness increases for the stratified case.

This example shows that the wave-current interaction, the physical bottom roughness associated with a moveable bed, and the suspended sediment stratification correction significantly influence the structure of the near bottom flow field. To further illustrate

how the moveable sediment bed and the wave affect the near bottom velocity profiles, the models will be rerun for the same conditions but with different types of bottom sediment or with different wave conditions.

To illustrate the moveable bed effects, the wave and current conditions are held constant while the bottom sediment is first assumed to be silt with a diameter d = 0.002 cm (1/5 the fine sand diameter) and then assumed to be a medium sand with a diameter d = 0.05 cm (5 times the fine sand diameter). Assuming spherical sediment particles, the fall velocity for the silt is 0.028 cm/sec, for the fine sand is 0.69 cm/sec, and for the medium sand is 6.6 cm/sec.

For the silt bed, the resulting neutral velocity profile is compared to the stratified velocity profile in Figure 4.5. The sediment concentration profile plotted in Figure 4.6 shows that because the silt fall velocity is so small, it is mixed almost uniformly throughout the near bottom flow field. Even though there is much more sediment in suspension compared to the fine sand case, the vertical density gradient induced by the silt is so small that the resulting stratification correction is almost negligible below 2 meters. Because the current velocity $|\vec{u}_r|$ was specified at 1 meter, there is little difference between the neutral and stratified model parameters listed in Table 4.1 for this type of bottom sediment.

For the silt bottom, the maximum Shields parameter based on skin friction is well above the breakoff point, so ripples are nearly washed out and the bottom roughness is dominated by near bed

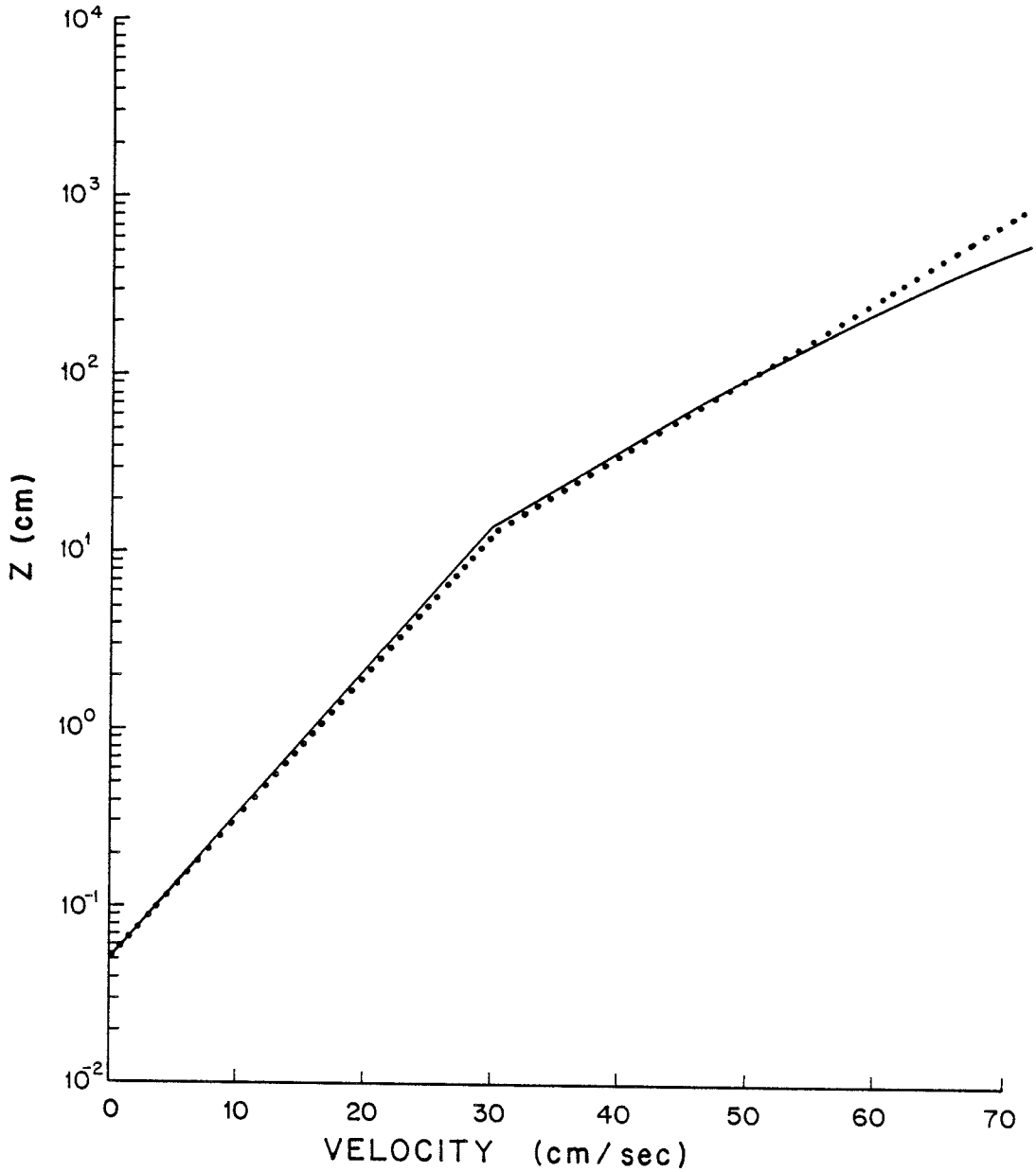

FIGURE 4.5
Current velocity profiles for the silt, medium wave case, predicted by the stratified (solid line) and the neutral (dotted line) near bottom models.

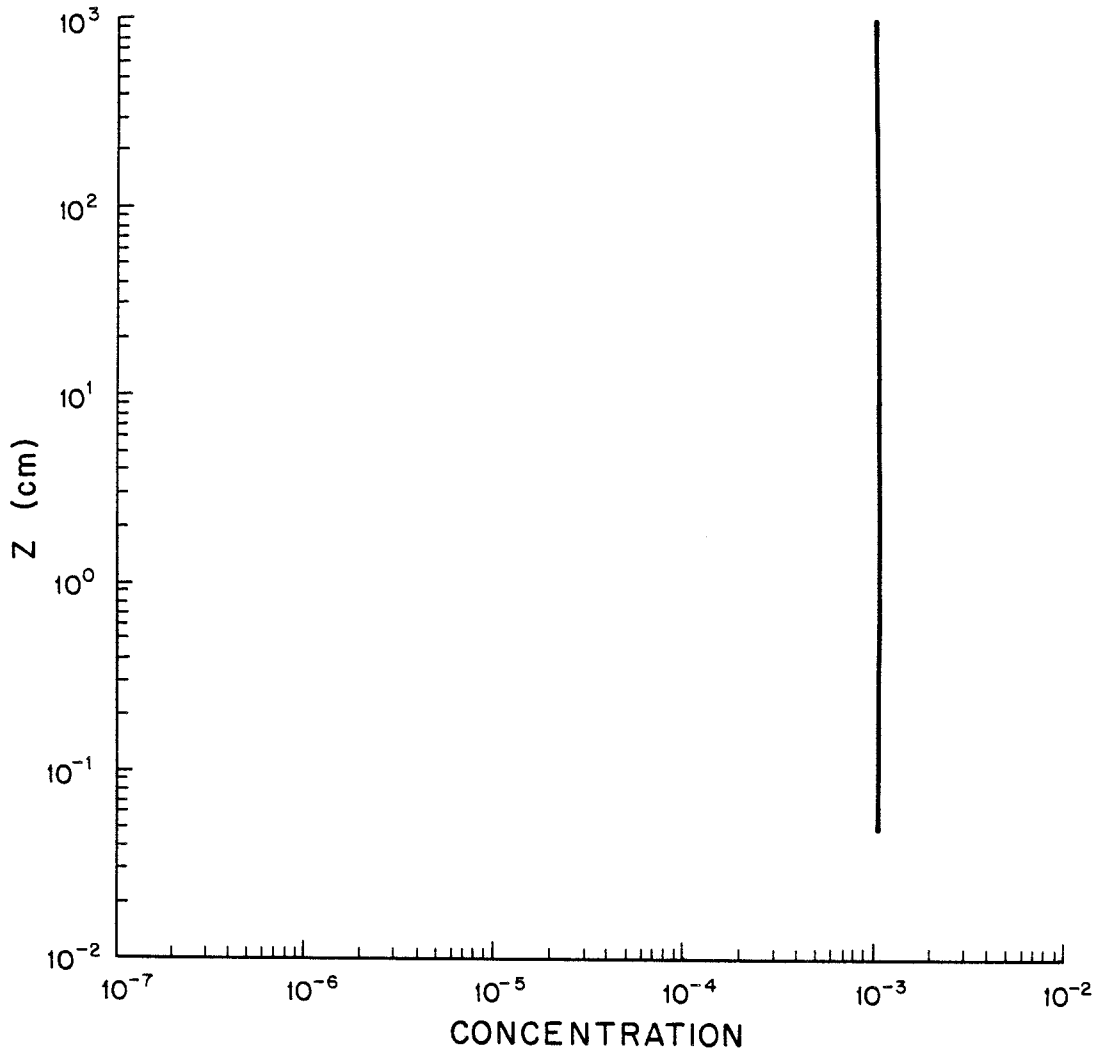

FIGURE 4.6
Sediment concentration profile for the silt, medium wave case, predicted by the stratified near bottom model.

transport. Because stratification reduces the skin friction only slightly, the effect on the bottom roughness lengths is negligible. Compared to the fine sand case, however, the roughness lengths z_o and z_{oc} are decreased by factors of 2-3 and the shear velocities are reduced by 20-25 percent.

The silt in this case is so fine ($S_* < 0.375$) that the breakoff point Shields parameter calculated from (3.67) is below the critical Shields parameter for initiation of motion, so equilibrium range ripples are not expected to form. Though the ripple geometry theory has only been tested in coarser sediments, this is a realistic result in agreement with observation. Another problem with very fine sediment is the uncertainty in the critical Shields parameter. As discussed by Grant et al. (1982), Shields diagram is considered an overestimate of the critical Shields parameter for fine non-cohesive sediments. Because a lower critical Shields parameter will only enhance the trends illustrated by this example, Shields curve was used to avoid choosing a value too low.

For the medium sand bed and the same wave and current conditions, the neutral and stratified velocity profiles are compared in Figure 4.7 and the sediment concentration profile is shown in Figure 4.8. Because the medium sand fall velocity is so large, the suspended sediment concentration decreases rapidly with distance from the bottom. Compared to the fine sand case, much less sediment is in suspension. The resulting vertical density gradient is so small that the stratification correction again is almost negligible. The model

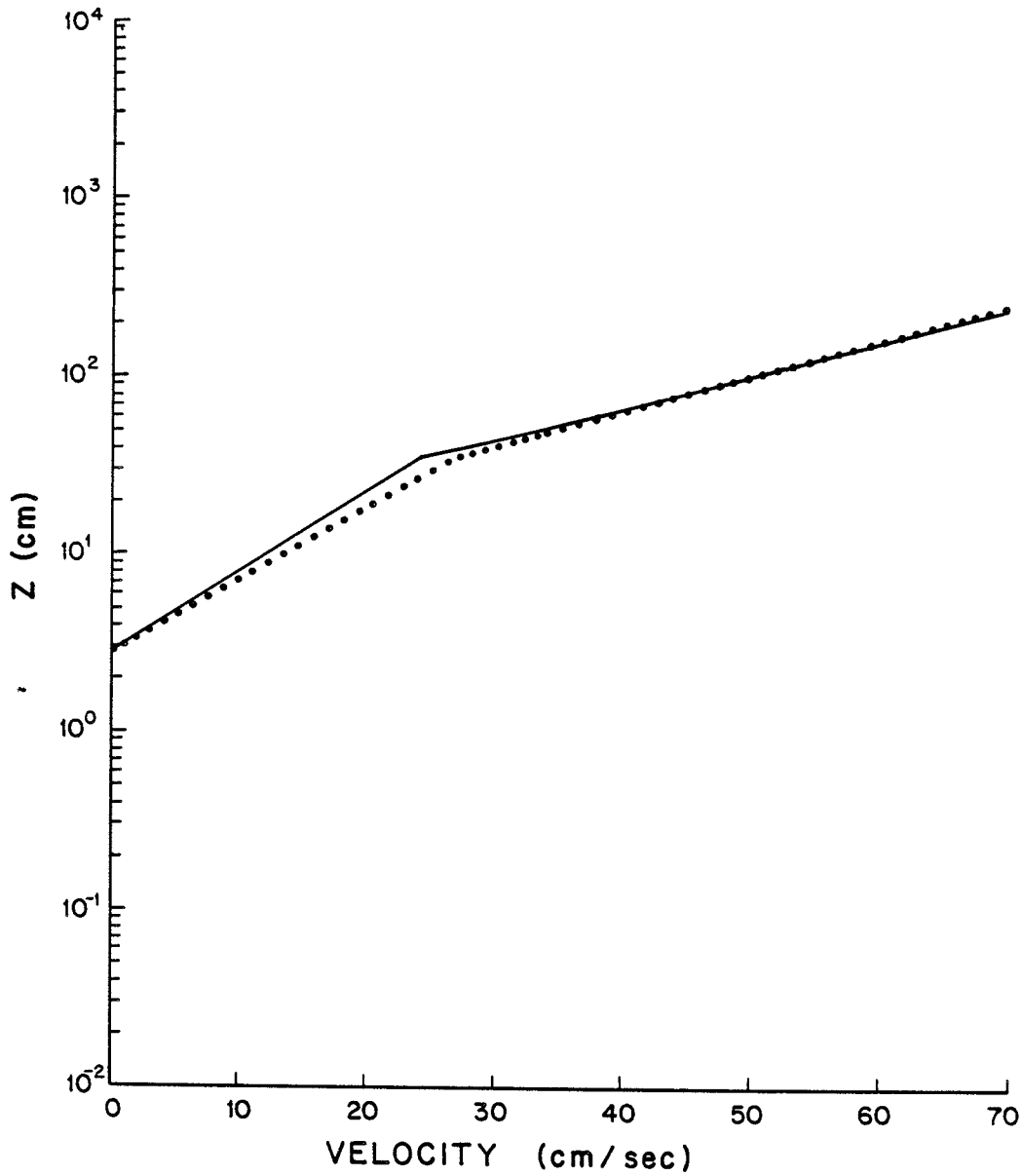

FIGURE 4.7
Current velocity profiles for the medium sand, medium wave case, predicted by the stratified (solid line) and the neutral (dotted line) near bottom models.

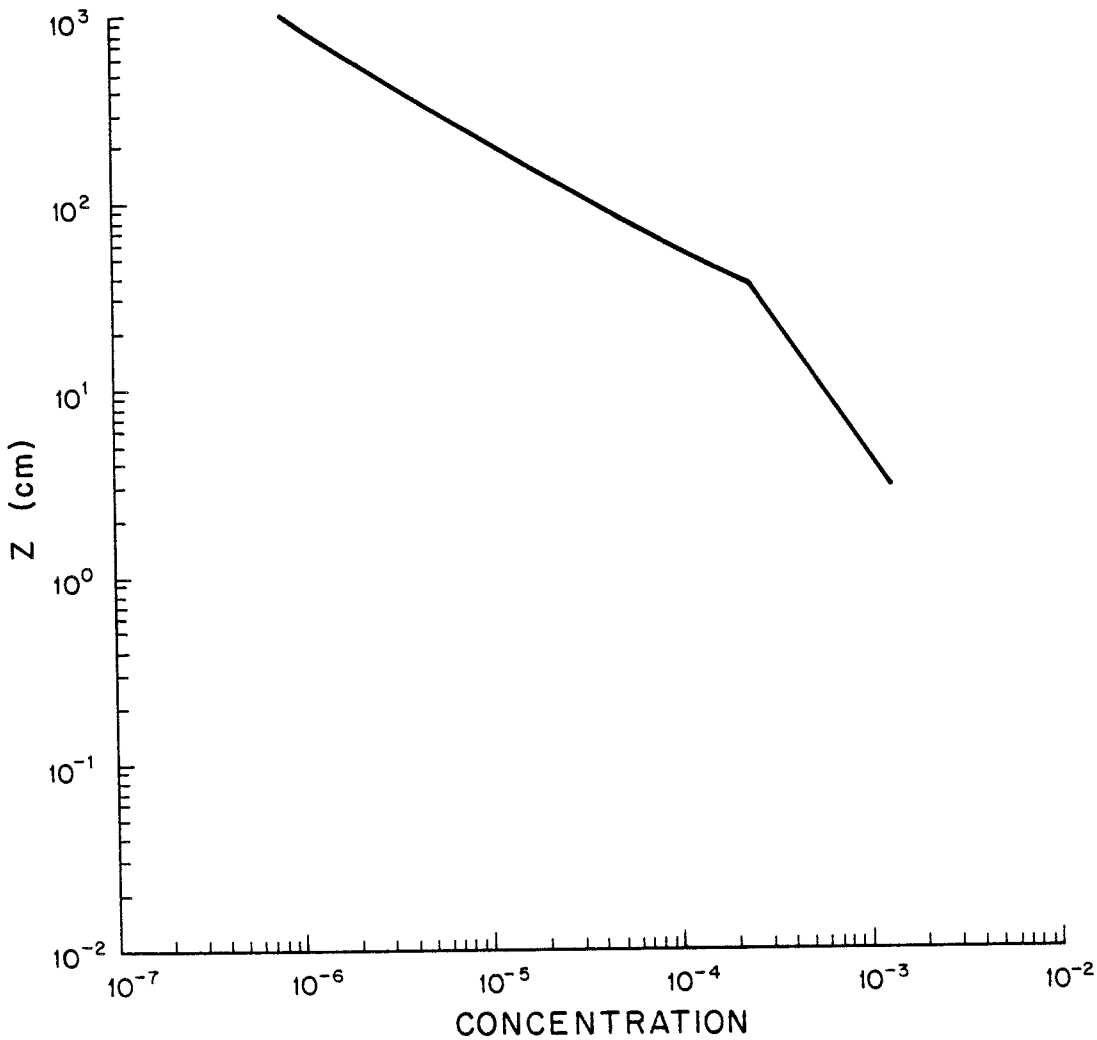

FIGURE 4.8
Sediment concentration profile for the medium sand, medium wave case, predicted by the stratified near bottom model.

parameters listed in Table 4.1 show little change between the neutral and stratified model runs.

The maximum Shields parameter based on skin friction for the medium sand case is below the breakoff point. Large equilibrium range ripples are formed and there is very little near bed transport. Since large ripples are effective roughness elements, the resulting physical bottom roughness is very large. Stratification again only slightly reduces the skin friction, so there is little effect on the bottom roughness. Compared to the fine sand case, the roughness lengths are orders of magnitude larger and the shear velocities are doubled.

This series of examples illustrates the effect different moveable sediment beds have on a combined wave and current flow field. For these wave and current conditions, the physical bottom roughness decreases as the sediment grain diameter decreases. The medium sand roughness was dominated by ripples, the fine sand roughness was due to both ripples and near bed transport, and the silt roughness was dominated by near bed transport. Since the bottom roughness decreases, the shear velocity also decreases with decreasing sediment size. In Section 4.1, it was shown that the near bottom suspended sediment induced stratification correction is only significant when the fall velocity, sediment concentration product is large. The medium sand fall velocity was so large that there was very little sediment in suspension. Suspended silt concentrations were significant but the silt fall velocity was too small. For the fine

sand, however, the fall velocity and the suspended sediment concentrations were large enough that stratification had a significant effect on the current velocity profile.

To illustrate the effect of the wave on the near bottom flow over a moveable bed, the current and the sediment parameters are held constant while the wave height is varied. The sediment again is assumed to be fine sand with a diameter d = 0.01 cm. The solution for a 6.5 meter high, 15 second wave in 100 meters of water shown in Figures 4.3 and 4.4 will be compared to wave heights first decreased and then increased by 1/2.

If the wave height is reduced by 1/2, the resulting wave parameters are $|\vec{u}_b|$ = 25 cm/sec and A_b = 60 cm/sec. The neutral and stratified velocity profiles are shown in Figure 4.9 and the concentration profile in Figure 4.10. Model parameters for this case are listed in Table 4.2. Compared to the initial example, the lower wave height results in a reduced skin friction, so the sediment reference concentration is reduced by a factor of 3-4. The resulting stratification correction is much less significant because there is not enough sediment in suspension to effectively stratify the flow.

The maximum Shields parameter based on skin friction in this case is just above the breakoff point. There is very little near bed transport and the physical bottom roughness is dominated by ripples. Because the wave is much weaker in this case, the apparent bottom roughness is only a factor of 3 greater than the physical bottom roughness. Compared to the medium wave case, the physical roughness

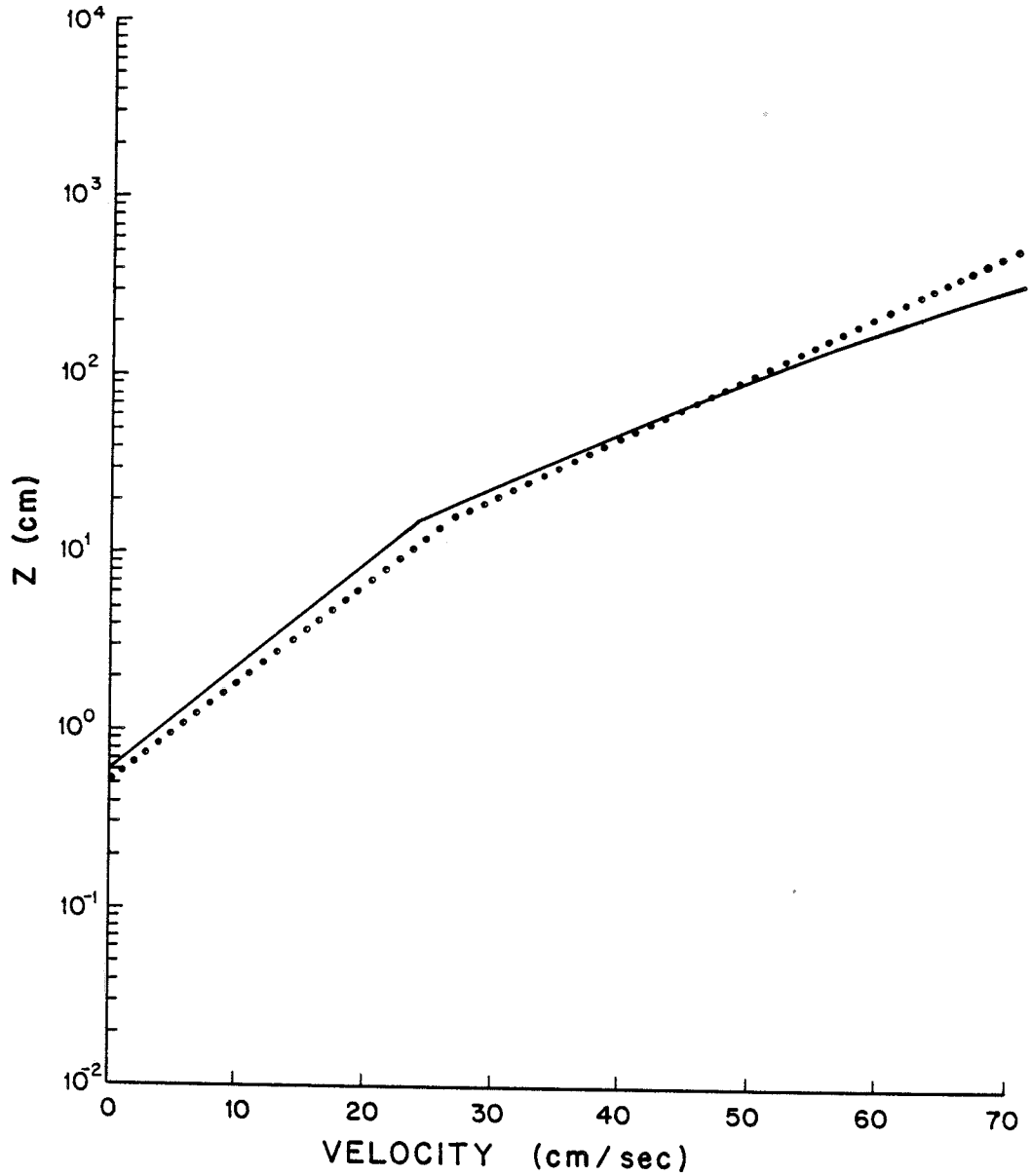

FIGURE 4.9
Current velocity profiles for the fine sand, small wave case, predicted by the stratified (solid line) and the neutral (dotted line) near bottom models.

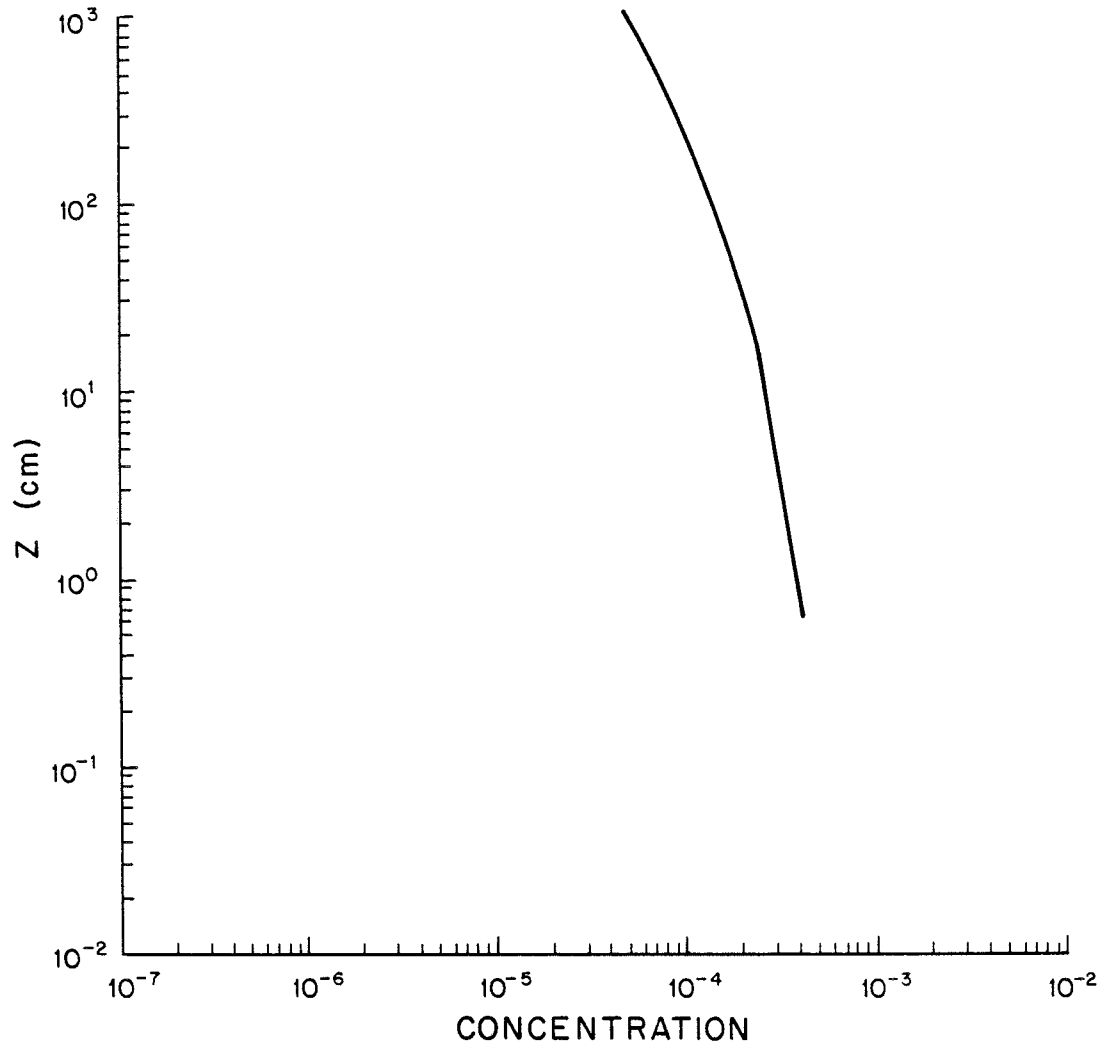

FIGURE 4.10
Sediment concentration profile for the fine sand, small wave case, predicted by the stratified near bottom model.

TABLE 4.2: Near Bottom Model Parameters: Fine Sand

	Small Wave		Medium Wave		Large Wave	
	Neutral	Stratified	Neutral	Stratified	Neutral	Stratified
δ_w(cm)	15.1	15.5	16.8	16.4	21.8	19.6
z_{oc}(cm)	1.79	2.19	1.41	2.06	2.27	3.97
z_o(cm)	0.514	0.621	0.162	0.196	0.170	0.164
u_{*c}(cm/sec)	4.97	4.90	4.69	4.01	5.28	3.39
u_{*cw}(cm/sec)	7.88	8.05	8.78	8.56	11.3	10.2
ψ'_m/ψ_c	2.55	2.36	6.46	5.52	11.3	9.02
ψ'_m/ψ_B	1.65	1.53	4.19	3.58	7.34	5.85
k_{bB}(cm)	15.0	18.2	2.93	4.34	1.08	1.91
k_{bT}(cm)	0.454	0.394	1.91	1.53	4.00	2.99
$C_{nm}(z_o)(x10^{-3})$		0.402		1.44		3.48

z_o is increased by a factor of 3, but the apparent roughness z_{oc} is only increased by 30 percent.

If the wave height is increased by 1/2, the wave conditions become $|\vec{u}_b|$ = 75 cm/sec and A_b = 180 cm/sec. The resulting neutral and stratified velocity profiles are compared in Figure 4.11 and the sediment concentration profile is plotted in Figure 4.12. In this case, sufficient sediment is in suspension to significantly stratify the near bottom flow. Model parameters for this example are listed in Table 4.2. Compared to the medium wave case, the larger wave results in a larger skin friction, which increases the sediment reference concentration by a factor of 2-3. Even though there is more sediment in suspension very near the bottom for the large wave case, away from the bottom there is less sediment in suspension. This occurs because the stratification correction also increases the sediment concentration vertical decay rate above the wave boundary layer. While the increased skin friction acts to increase sediment concentrations in the wave boundary layer, the increased stratification correction acts to confine the suspended sediment close to the bottom.

For the neutral, large wave model run, the maximum Shields parameter based on skin friction is well above the breakoff point. Ripples are washed out and the bottom roughness is dominated by near bed transport. For the stratified case, however, the skin friction is reduced so the ripple roughness and near bed transport roughness are the same order of magnitude. Since the ripple roughness increases

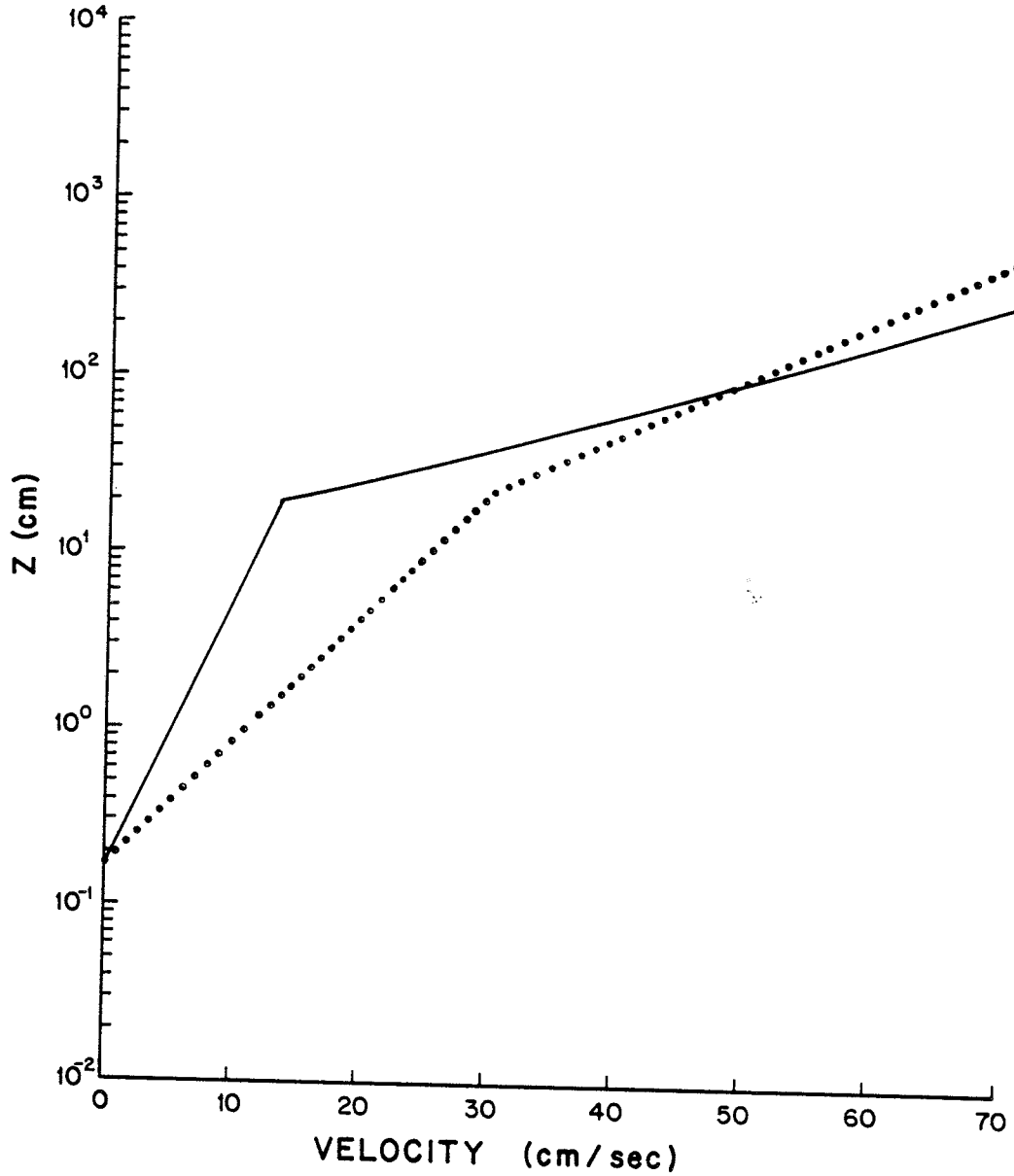

FIGURE 4.11
Current velocity profiles for the fine sand, large wave case, predicted by the stratified (solid line) and the neutral (dotted line) near bottom models.

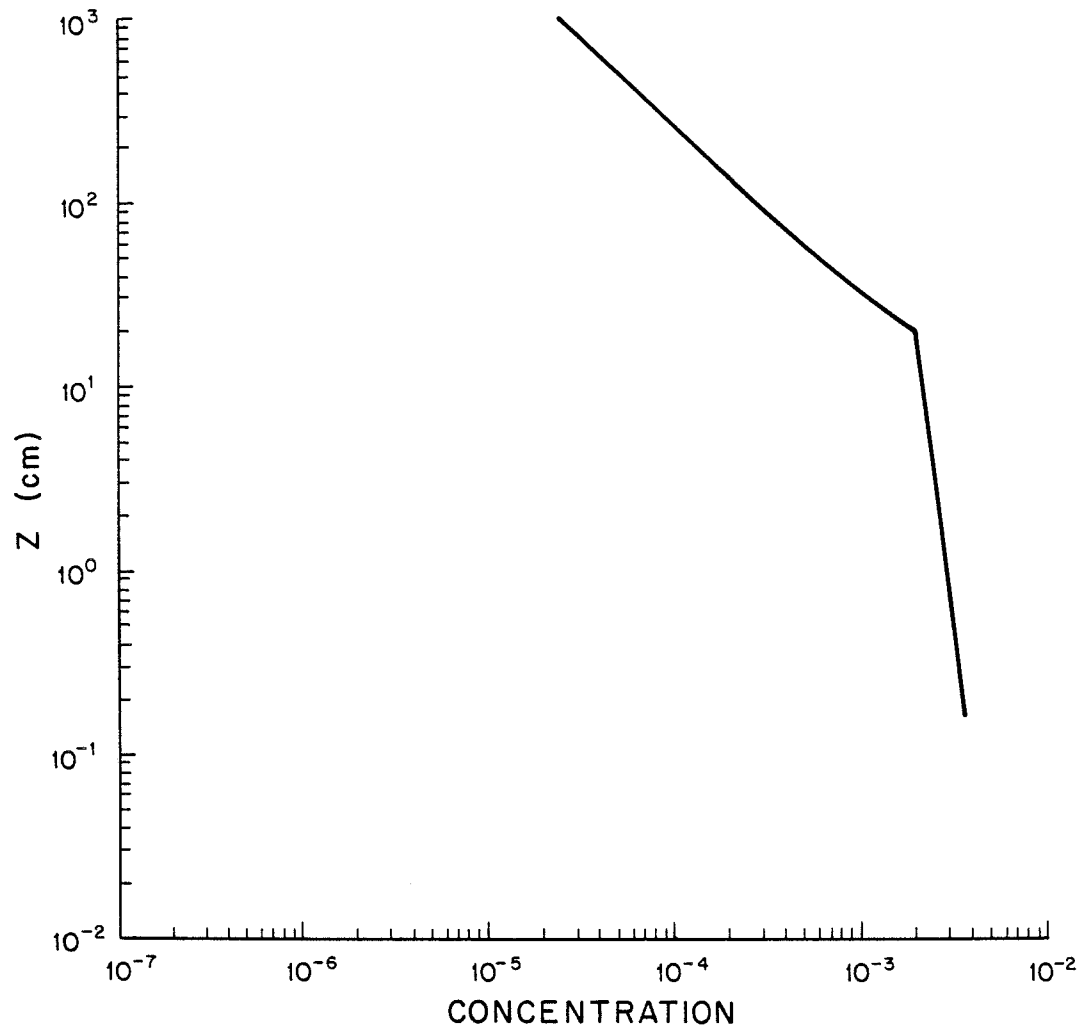

FIGURE 4.12
Sediment concentration profile for the fine sand, large wave case, predicted by the stratified near bottom model.

by nearly the same amount as the transport roughness decreases, the total physical bottom roughness is approximately the same for both the neutral and stratified cases. While the apparent roughness for the neutral model is a factor of 13 greater than the physical bottom roughness, the apparent roughness for the stratified model is a factor of 24 greater. In this case, stratification acts to enhance the effect of the wave on the current.

Compared to the neutral, large wave model run, stratification changes the characteristics of the physical bottom roughness, increases the apparent bottom roughness, and reduces the shear velocity felt by the current above the wave boundary layer by 35 percent. The resulting current velocity at the top of the wave boundary layer is drastically reduced from 30 cm/sec to 13.5 cm/sec, demonstrating that under the proper conditions, suspended sediment induced stratification can significantly influence the near bottom flow field.

This final series of examples illustrates the effect of the wave on the near bottom flow. As the wave height increases, the wave dominated skin friction also increases, reducing the ripple roughness, increasing the near bed transport roughness, and increasing the amount of sediment in suspension. The bottom roughness for the small wave is dominated by the ripples, for the medium wave is due to ripples and near bed transport, and for the neutral, large wave case is dominated by near bed transport. As suspended sediment

concentrations for this sediment increase, suspended sediment induced stratification effects are enhanced. The stratification correction increases the current shear, so current velocities below the height z_r, shear velocities, and skin friction are reduced. Stratification also increases the sediment concentration vertical decay rate, so sediment is confined close to the bottom.

5. THEORETICAL MODEL FOR A STRATIFIED EKMAN LAYER IN COMBINED WAVES AND CURRENTS OVER A MOVEABLE BED

Currents in the ocean are often influenced by Coriolis acceleration due to the earth's rotation or stratification induced by vertical temperature and salinity gradients, effects that were neglected by the near bottom models. The near bottom models apply only to the current constant stress layer where Coriolis acceleration has little effect on the velocity profiles. Temperature and salinity induced stratification was neglected because typical density profiles on the continental shelf indicate that the near bottom flow is usually well mixed. Coriolis acceleration, however, must be included in the governing momentum equation if velocity profiles are desired above the constant stress layer. If Ekman layer height exceeds the mixed layer height, the effect of temperature and salinity induced stratification also must be included in the eddy diffusivity model for the turbulent fluxes.

In this chapter a model is developed for a stratified Ekman layer in a combined wave and current flow over a moveable bottom. The stratified, near bottom model developed in Section 4.1 is extended by including the effects of planetary rotation and stratification induced by temperature and salinity gradients. As before, boundary conditions on the velocity and sediment concentration profiles can be applied using the physical bottom roughness model discussed in Section 3.2 and the reference concentration model developed in Section 4.2. The temperature and salinity profiles are assumed to be given. Sample Ekman layer model runs are discussed in Section 5.2.

5.1 Ekman Layer Model

The Ekman layer model will be developed following the usual approach for small sediment concentrations as in the stratified, near bottom model. Conservation of momentum is applied to each sediment particle to find the sediment velocity in terms of the fluid velocity. The continuum hypothesis again is invoked to write conservation equations for sediment mass, fluid mass, and fluid momentum. The turbulent fluxes are represented by an eddy diffusivity model similar to a model developed by Long (1981), and the resulting equations are solved for the fluid velocity and sediment concentration profiles.

5.1.1 Governing equations

For small sediment concentrations, the sediment momentum equations reduce to (4.1) assuming $d \ll z$ and neglecting particle interactions. Invoking the continuum assumption, conservation of sediment mass is written as (4.3) for each sediment class. By the Boussinesq approximation, the conservation of fluid momentum equation is given by (4.5). Because the fluid density is a function of temperature and salinity, conservation of fluid mass must be written

$$\frac{\partial \rho C}{\partial t} + \vec{\nabla} \cdot (\rho C \vec{u}) + \frac{\partial}{\partial z} (\rho C w) = 0 \tag{5.1}$$

Assuming the fluid flow is incompressible,

$$\frac{D\rho}{Dt} = 0 \tag{5.2}$$

and the conservation of fluid mass equation reduces to (4.4). For the small sediment concentrations expected, the vertical fluid velocity induced by the falling sediment can be neglected and the usual continuity equation given by (4.9) is recovered.

The fluid velocity and pressure can be partitioned into current, wave, and turbulent components as in (3.2) and the concentrations can be partitioned into mean, periodic, and turbulent components as in (4.10). The fluid density similarly can be partitioned into mean, periodic, and turbulent components

$$\rho = \rho_m + \rho_p + \rho' \tag{5.3}$$

The partitioned variables can be substituted into the governing equations which are Reynolds averaged. The resulting equations then can be simplified by the usual scaling arguments.

The current, mean concentrations, and mean fluid density are assumed to be horizontally homogeneous. Nonlinear convective terms containing derivatives of periodic variables are neglected compared to the local time derivatives of the periodic variables. Coriolis acceleration of the wave is neglected compared to the local wave acceleration. Viscous stresses are neglected compared to Reynolds stresses and horizontal derivatives of turbulent fluxes are neglected compared to vertical derivatives. With these simplifying assumptions, the resulting equations governing the flow in the Ekman layer become

$$\frac{\partial}{\partial t}(\vec{u}_c + \vec{u}_w) + f\,\hat{k} \times \vec{u}_c = -\frac{1}{\rho}\vec{\nabla}(p_c + p_w) - \frac{\partial}{\partial z}\overline{(\vec{u}'w')} \tag{5.4}$$

$$\frac{\partial}{\partial t}(C_{nm} + C_{np}) + w_w \frac{\partial C_{nm}}{\partial z} - w_{fn}\frac{\partial}{\partial z}(C_{nm} + C_{np}) + \frac{\partial}{\partial z}(\overline{C_n' w'}) = 0 \tag{5.5}$$

$$\frac{\partial}{\partial t}(\rho_m + \rho_p) + w_w \frac{\partial \rho_m}{\partial z} + \frac{\partial}{\partial z}(\overline{\rho' w'}) = 0 \tag{5.6}$$

where the quasi-steady assumption has not yet been invoked for the current, mean concentration, and mean density.

5.1.2 Turbulent closure scheme

As in Section 4.1.2, an eddy diffusivity model is adopted for turbulent closure. Along with equations (4.17) and (4.20) for the fluid momentum and sediment mass fluxes must be included an expression for the fluid density flux

$$-\overline{\rho' w'} = \nu_{tf}\frac{\partial}{\partial z}(\rho_m + \rho_p) \tag{5.7}$$

where $\nu_{tf} = \nu_{ts}$ by the assumed sediment velocity. The eddy diffusivities again can be written in terms of the neutral eddy viscosities and stratification corrections given by (4.21) through (4.24). As before, the remaining task is to define characteristic eddy viscosities and stratification corrections in and above the wave boundary layer.

In the wave boundary layer, the neutral eddy viscosity is assumed

to be the usual linear function of z given by (4.35). Since the near bottom flow is expected to be well mixed, it is assumed that temperature and salinity stratification do not influence turbulent diffusion in the wave boundary layer. Because the stratification correction for suspended sediment was shown to be negligible in the wave boundary layer, the characteristic stability parameter is assumed to be zero for $z < \delta_w$.

Above the wave boundary layer, the eddy viscosity and stability parameter must apply not only to the constant stress layer but to the full Ekman layer. Ellison (1956) and Businger and Ayra (1974) suggest that the neutral eddy viscosity for a pure current Ekman layer is well represented by a linear function of z modulated by an exponential decay

$$\nu_t = \kappa |\vec{u}_*| \, z \, e^{- z/h} \tag{5.8}$$

where h is a height to be determined. Equation (5.8) increases linearly for small z, reaches a maximum at z = h and decays exponentially for large z. Long (1981) solves the neutral pure current Ekman layer equations using the eddy viscosity given by (5.8) and finds that for large $|\vec{u}_*|/f \, z_o$,

$$h \sim \frac{1}{6} \frac{|\vec{u}_*|}{f} \tag{5.9}$$

Long (1981) also generalizes the constant stress layer stability parameter by modeling the terms in the turbulent kinetic energy

equation. The generalized stability parameter for a stratified pure current Ekman layer derived by Long (1981) can be written

$$\zeta = \frac{\nu_t}{\frac{|\vec{u}_*|^2}{|\overrightarrow{-u'w'}|}} \frac{g}{\bar{\rho}} \overline{\rho' w'} \tag{5.10}$$

where ν_t is the neutral eddy viscosity given by (5.8) and $\rho\,|\overrightarrow{-u'w'}|$ is the magnitude of the local turbulent shear stress. In the constant stress layer, $\nu_t \approx \kappa\,|\vec{u}_*|\,z$, $|-\overrightarrow{u'w'}| \approx |\vec{u}_*|^2$, and it follows that $\zeta \approx z/L$, consistent with the earlier definition of the stability parameter. Long (1981) has demonstrated that this form for the generalized stability parameter agrees well with data.

Using Long's (1981) results, a characteristic eddy viscosity and stability parameter can be defined above the wave boundary layer for a combined wave and current Ekman layer. Defining the characteristic length scale of the Ekman layer as

$$l_c = \frac{\kappa\,|\vec{u}_{*c}|}{f} \tag{5.11}$$

the neutral eddy viscosity above the wave boundary layer can be written

$$\nu_{tc} = \kappa\,|\vec{u}_{*c}|\,z\,e^{-2.4\,z/l_c} \qquad z > \delta_w \tag{5.12}$$

The characteristic stability parameter above the wave boundary layer becomes

$$\zeta_c = \frac{\nu_{tc}}{|\vec{u}_{*c}|^2 \; |-\overline{\vec{u}'w'}|} \frac{g}{\bar{\rho}_T} \overline{\rho'_T w'} \qquad z > \delta_w \tag{5.13}$$

The modulated eddy viscosity given by (5.12) is compared to the linear eddy viscosity given by (3.24) in Figure 5.1.

The buoyancy term in the stability parameter in this case must be found for a suspension of sediment in a fluid with variable density. The total density of the suspension can be written approximately as

$$\rho_T = \rho + \sum_n (\rho_{sn} - \rho) C_n \sim \rho + \rho_b \sum_n (s_n - 1) C_n \tag{5.14}$$

where ρ is the fluid density which is a function of z, ρ_b is the constant fluid density in the bottom mixed layer where suspended sediment concentrations are expected to be significant, and $s_n = \rho_{sn}/\rho_b$. Since the difference between ρ and ρ_b above the mixed layer is expected to be 0 (10^{-3}) and maximum sediment concentrations are 0 (10^{-3}), the use of ρ_b rather than ρ in the suspended sediment term above the mixed layer results in a negligible error. Substituting partitioned variables for ρ_T, ρ, and C_n, it is found that after Reynolds averaging

$$\overline{\rho_T} \sim \bar{\rho} \sim \rho_b \tag{5.15}$$

and

$$\rho'_T = \rho' + \rho_b \sum_n (s_n - 1) C'_n \tag{5.16}$$

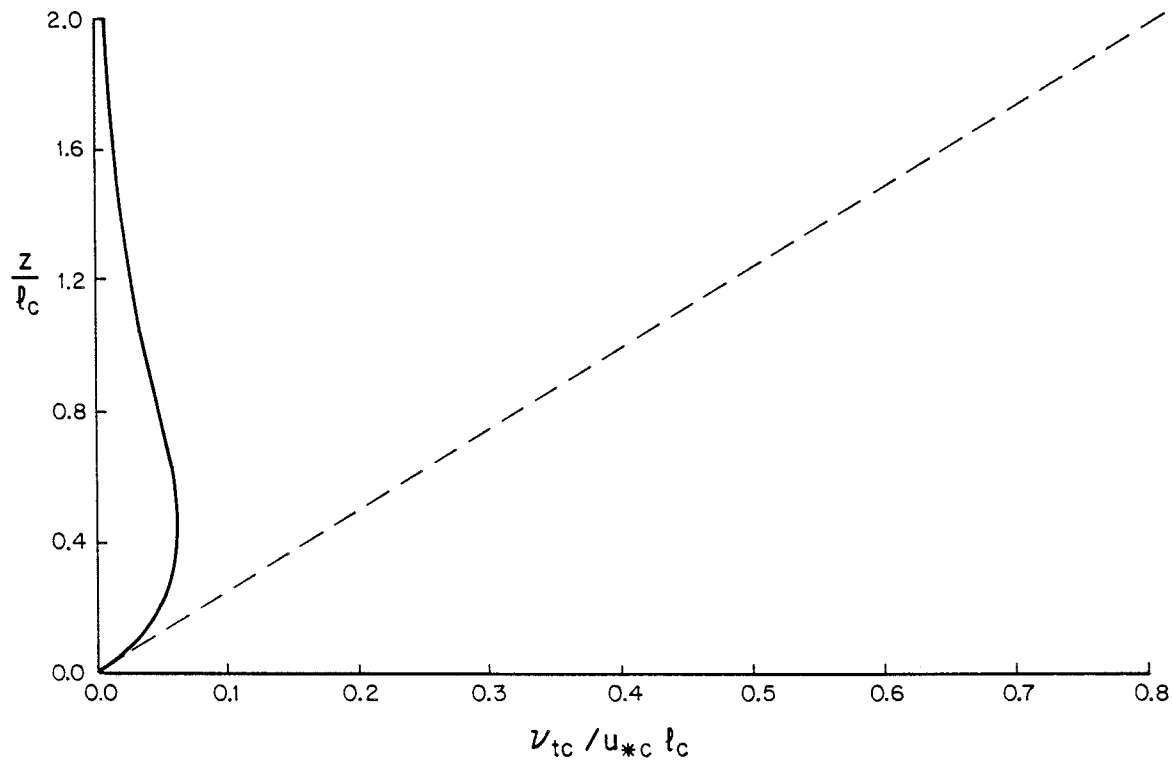

FIGURE 5.1
Dimensionless eddy viscosity $\nu_{tc}/u_{*c}\, l_c$ in the current boundary layer as a function of z/l_c; linear eddy viscosity (dashed line) given by (3.24) compared to modulated eddy viscosity (solid line) given by (5.12).

Substituting (5.15) and (5.16) into (5.13), the generalized stability parameter can be written

$$\zeta_c = \frac{\nu_{tc}}{|\vec{u}_{*c}|^2 \, |-\overline{\vec{u}'w'}|} \left[\frac{g}{\rho}\overline{\rho'w'} + \sum_n g\,(s_n-1)\,\overline{C_n'w'}\right] \qquad z > \delta_w \tag{5.17}$$

Equations (4.17), (4.20) and (5.7) then can be substituted for the turbulent fluxes in (5.17). Assuming $\rho \sim \rho_m$ and since the turbulent flux components associated with the periodic variables are negligible above the wave boundary layer, (5.17) becomes

$$\zeta_c = \frac{\nu_{tc}}{|\vec{u}_{*c}|^2} \left(\frac{1+\beta\zeta_c}{\left|\frac{\partial \vec{u}_c}{\partial z}\right|}\right) \frac{\left[-\frac{g}{\rho_m}\frac{\partial \rho_m}{\partial z} - \sum_n g\,(s_n-1)\frac{\partial C_{nm}}{\partial z}\right]}{(\gamma+\beta\zeta_c)} \qquad z > \delta_w \tag{5.18}$$

or

$$\frac{\zeta_c\,(\gamma+\beta\zeta_c)}{(1+\beta\zeta_c)} = R \tag{5.19}$$

where

$$R = \frac{\nu_{tc}}{|\vec{u}_{*c}|^2} \frac{\left[-\frac{g}{\rho_m}\frac{\partial \rho_m}{\partial z} - \sum_n g\,(s_n-1)\frac{\partial C_{nm}}{\partial z}\right]}{\left|\frac{\partial \vec{u}_c}{\partial z}\right|} \tag{5.20}$$

Solving (5.19) for the generalized stability parameter gives

$$\zeta_c = \frac{1}{2}\left(R - \frac{\gamma}{\beta}\right) + \left[\frac{1}{4}\left(R - \frac{\gamma}{\beta}\right)^2 + \frac{R}{\beta}\right]^{1/2} \qquad z > \delta_w \tag{5.21}$$

Substituting the eddy diffusivity model for the turbulent fluxes in the governing equations, (5.4), (5.5) and (5.6) can be written

$$\frac{\partial}{\partial t}(\vec{u}_c + \vec{u}_w) + f\,\hat{k} \times \vec{u}_c = -\frac{1}{\rho}\vec{\nabla}(p_c + p_w) + \frac{\partial}{\partial z}\left[\nu_{tm}\frac{\partial}{\partial z}(\vec{u}_c + \vec{u}_w)\right] \tag{5.22}$$

$$\frac{\partial}{\partial t}(C_{nm} + C_{np}) + w_w\frac{\partial C_{nm}}{\partial z} - w_{fn}\frac{\partial}{\partial z}(C_{nm} + C_{np}) - \frac{\partial}{\partial z}\left[\nu_{ts}\frac{\partial}{\partial z}(C_{nm} + C_{np})\right] = 0 \tag{5.23}$$

$$\frac{\partial}{\partial t}(\rho_m + \rho_w) + w_w\frac{\partial \rho_m}{\partial z} - \frac{\partial}{\partial z}\left[\nu_{tf}\frac{\partial}{\partial z}(\rho_m + \rho_p)\right] = 0 \tag{5.24}$$

where the appropriate eddy viscosity and stability parameter are used for each boundary layer. Because the eddy diffusivities are constant in time and assuming there is little variation in the current, mean concentration, and mean density over a wave period, (5.22), (5.23) and (5.24) again can be separated by averaging over a wave period. Since the resulting equations for the wave and the periodic concentration are the same as before, the solutions discussed in Sections 3.1.3 and 4.1.6 remain valid.

5.1.3 Solution for the periodic fluid density

Averaging (5.24) over a wave period and subtracting the averaged equation from the original gives the equation for the periodic density above the wave boundary layer as

$$\frac{\partial \rho_p}{\partial t} + w_w \frac{\partial \rho_m}{\partial z} = 0 \qquad z > \delta_w \tag{5.25}$$

since turbulent diffusion associated with the periodic density is negligible in this region. Similar to the periodic sediment concentration above the wave boundary layer, the periodic density change is associated with the vertical advection of the mean density gradient by the wave. Solving (5.25) for the periodic density gives

$$\rho_p = A_b \sinh kz \frac{\partial \rho_m}{\partial z} \sin (k_x x + k_y y - \omega t) \tag{5.26}$$

Because the mean fluid density gradient is assumed to be approximately zero in the bottom mixed layer, the periodic concentration also is approximately zero in this region. By the same scaling arguments used in Section 4.1.6, the periodic density is much less than the mean density and $\overline{\rho} \sim \rho_m$. Equation (5.26) also can be used to show that the nonlinear convective terms associated with the periodic density gradient,

$$\vec{u}_w \cdot \vec{\nabla} \rho_p + w_w \frac{\partial \rho_p}{\partial t} \tag{5.27}$$

do not contribute to the mean density equation because $\vec{u}_w$ is 90° out of phase with $\vec{\nabla} \rho_p$ and w_w is 90° out of phase with $\partial\rho/\partial z$.

Since the wave boundary layer is expected to be very well mixed, the periodic density is assumed to be zero for $z < \delta_w$.

5.1.4 Quasi-steady assumptions

Averaging (5.22), (5.23) and (5.24) over a wave period gives the following equations for the current, mean sediment concentrations, and mean fluid density,

$$\frac{\partial \vec{u}_c}{\partial t} + f \hat{k} \times \vec{u}_c = -\frac{1}{\rho} \vec{\nabla} p_c + \frac{\partial}{\partial z} \left(\nu_{tm} \frac{\partial \vec{u}_c}{\partial z} \right) \tag{5.28}$$

$$\frac{\partial C_{nm}}{\partial t} - \frac{\partial}{\partial z} \left(\nu_{ts} \frac{\partial C_{nm}}{\partial z} + w_{fn} C_{nm} \right) = 0 \tag{5.29}$$

$$\frac{\partial \rho_m}{\partial t} - \frac{\partial}{\partial z} \left(\nu_{tf} \frac{\partial \rho_m}{\partial z} \right) = 0 \tag{5.30}$$

Whereas the mean concentration equation has a term associated with the sediment fall velocity to balance the upward turbulent diffusion of sediment so that a concentration gradient can exist in equilibrium, the mean density equation has no such term. Above the Ekman layer, the turbulent fluxes are negligible and ρ_m is constant in time. In the Ekman layer, however, ρ_m is required to continually change with time until the fluid density gradient is zero. Changes in the mean density profile cause the stability parameter to vary. Since all three equations are coupled through the stability parameter, the Ekman layer does not reach a steady state until the fluid density is uniform throughout the Ekman layer.

To find the evolution in time of the velocity, concentration, and density profiles, (5.28), (5.29) and (5.30) must be solved simultaneously. Since these equations involve both time and space

derivatives, they can be solved by a numerical implicit difference method using central differencing in the vertical and forward differencing in time. The boundary conditions required to solve this problem are that $\vec{u}_c$, C_{nm}, and ρ_m be known for all z at time t = 0, and that $\vec{u}_c$, C_{nm}, and ρ_m be known at two values of z for all time. This solution technique, with its complex boundary conditions, however, is not in the spirit of the original objective, which was to develop a simple model for the bottom boundary layer that requires a minimum number of input parameters. Because the equations are complicated by the time derivatives, the problem would be greatly simplified if it could be considered quasi-steady.

The Ekman layer can be regarded as quasi-steady if the unsteady terms do not affect the dominant balance in (5.28) and (5.29), that is, if

$$\frac{\partial \vec{u}_c}{\partial t} \ll f \hat{k} \times \vec{u}_c \tag{5.31}$$

$$\frac{\partial C_{nm}}{\partial t} \ll w_{fn} \frac{\partial C_{nm}}{\partial z} \tag{5.32}$$

and if the stability parameter is approximately constant over the time scale of the momentum transporting turbulent eddies. In the usual case of interest on the continental shelf, the fluid density profile consists of a bottom mixed layer of nearly constant density with temperature and salinity induced density gradients above. If the pressure gradient forcing the flow remains constant, the Ekman

layer and mixed layer heights will grow with time until the Ekman layer is no longer stratified by temperature and salinity and a steady state is reached. Equations (5.28) and (5.29) are unsteady because the stability parameter varies with time as the fluid density field is modified by the flow. The time scale for velocity and concentration changes, therefore, is the same as the time scale for changes in the stability parameter. The time scale for the stability parameter can be estimated by scaling the fluid density equation for a typical condition on the continental shelf. For a typical $|\vec{u}_{*c}| = 0$ (1 cm/sec.) and $f = 0$ (10^{-4}/sec), the scale height for the Ekman layer is $l_c = 0$ (40 meters). A typical mixed layer height is $z_m = 0$ (20 meters) and typical stability parameters above the mixed layer are in the range $0\ (1) < \zeta_c < 0\ (1000)$. The order of magnitude of the local time derivative of density can be estimated from (5.30) as

$$\frac{\Delta\rho}{\Delta t} \sim 0 \left(\frac{\kappa |\vec{u}_{*c}| e^{-2.4\, z/l_c}}{\gamma + \beta \zeta_c} \frac{\Delta\rho}{\Delta z}\right) \tag{5.33}$$

Since $\Delta\rho$ is the same order of magnitude on both sides (5.33) and $\Delta z \sim 0$ (10 meters), the time scale for changes in the density profile for this case are

$$\Delta t \sim 0\ (10^5 \text{ sec}) \tag{5.34}$$

The time scale for the right hand side of (5.31) is

$$\Delta t \sim 0\left(\frac{1}{f}\right) \sim 0\ (10^4\ \text{sec}) \tag{5.35}$$

For a small fall velocity $w_{fn} \sim 0$ (0.1 cm/sec), the time scale for the left hand side of (5.32) is

$$\Delta t \sim 0\left(\frac{\Delta z}{w_{fn}}\right) \sim 0\ (10^4\ \text{sec}) \tag{5.36}$$

The time scale for the momentum transporting turbulent eddies is

$$\Delta t \sim 0\left(\frac{\nu_{tm}}{|u_{*c}|^2}\right) \sim 0\ (10^2\ \text{sec}) \tag{5.37}$$

As long as the current and mean concentrations do not change by more than an order of magnitude as the fluid density profile is mixed, the quasi-steady assumption can be applied for this case and the time derivatives in (5.28) and (5.29) can be neglected. By specifying the quasi-steady fluid density distribution, the quasi-steady stability parameter can be found and (5.28) and (5.29) can be solved for the quasi-steady current and mean concentration profiles.

5.1.5 Solution for the mean concentration

If the Ekman layer can be considered quasi-steady, the equation for the mean sediment concentration is the same as (4.40). Because the eddy diffusivity is unchanged within the wave boundary layer, the solution for the mean concentration given by (4.57) still applies for $z < \delta_w$. Above the wave boundary layer, the neutral eddy viscosity is given by (5.12) and the stability parameter by (5.21). The quasi-

steady, mean concentration equation becomes

$$\frac{\partial C_{nm}}{\partial z} + \frac{\gamma + \beta \zeta_c}{\kappa |u_{*c}| z e^{-2.4 z/l_c}} w_{fn} C_{nm} = 0 \qquad z > \delta_w \tag{5.38}$$

The solution to (5.38) is

$$C_{nm}(z) = C_{nm}(\delta_w) \left[\exp\left(-\frac{\gamma w_{fn}}{\kappa |u_{*c}|} \int_{\delta_w}^{z} \frac{e^{2.4 z/l_c}}{z} dz\right)\right]. \tag{5.39}$$

$$\cdot\left[\exp\left(\frac{-\beta w_{fn}}{u_{*c}} \int_{\delta_w}^{z} \zeta_c \frac{e^{2.4 z/l_c}}{z} dz\right)\right]$$

After evaluating the integral, the first decay factor in (5.39) can be written as

$$\exp\left\{-\frac{\gamma w_{fn}}{\kappa |u_{*c}|}\left[Ei\left(\frac{2.4 z}{l_c}\right) - Ei\left(\frac{2.4 \delta_w}{l_c}\right)\right]\right\} \tag{5.40}$$

where Ei(x) is the exponential integral function. The series expansion of Ei(x) given by Abramowitz and Stegun (1972) is

$$Ei(x) = .57721 + \ln x + \sum_{n=1}^{\infty} \frac{x^n}{n\, n!} \tag{5.41}$$

where the initial constant is Euler's constant. Since $\delta_w << l_c$, it follows that $\sum_{n=1}^{\infty} (2.4\, \delta_w/l_c)^n/n\, n! << 1$ and the first decay factor can be written

$$\left(\frac{z}{\delta_w}\right)^{\left(-\frac{\gamma w_{fn}}{\kappa |u_{*c}|}\right)} \exp\left(-\frac{\gamma w_{fn}}{\kappa |u_{*c}|} \sum_{n=1}^{\infty} \frac{(2.4\ z/l_c)^n}{n\ n!}\right) \tag{5.42}$$

This is equivalent to the constant stress layer decay rate multiplied by an exponential decay rate that increases rapidly for $z \geq 0\ (l_c/2.4)$.

The second decay factor in (5.39) is associated with the stability parameter, so temperature and salinity induced stratification also acts to reduce sediment concentrations above the mixed layer. In the constant stress layer, $\zeta_c > z/l_c$, $e^{2.4\ z/l_c} > 1$, and the second decay factor is the same as in (4.46). The mean sediment concentration profile given by (5.39) therefore is very similar to (4.46) in the constant stress layer.

5.1.6 Simplification of the stability parameter

The rapid decrease in mean sediment concentrations for $z > 0\ (l_c/2.4)$ suggests that suspended sediment may not affect the stability parameter in the upper Ekman layer. The vertical structure of the stability parameter in the constant stress layer is governed by the two factors in (4.51). The first factor causes the stability parameter to increase with z while the second factor limits the growth, causing the stability parameter to approach a constant as z increases. When the additional decay rate above the constant stress layer associated with the exponential term in (5.42) is included in the stability parameter, however, the stability parameter decreases

above the constant stress layer. Temperature and salinity induced stratification also limit the amount of sediment in suspension above the mixed layer, further reducing the suspended sediment contribution to the stability parameter. Suspended sediment induced stratification therefore is expected to be negligible above the mixed layer where stratification is dominated by temperature and salinity.

In the mixed layer, fluid density gradients are very small. While uniform mixing of the Ekman layer requires a decrease in the mixed layer fluid density with time, fluid density gradients and the induced stratification are expected to remain small in this region. Stratification in the mixed layer therefore is expected to be dominated by suspended sediment.

It therefore is proposed that the stability parameter given by (5.21) usually can be approximated by considering only the dominant source of stratification in each region. Above the mixed layer, R in (5.21) is assumed to include temperature and salinity stratification only and can be written

$$R = \frac{\nu_{tc}}{|\vec{u}_{*c}|^2} \quad \frac{N^2}{\left|\frac{\partial \vec{u}_c}{\partial z}\right|} \tag{5.43}$$

where ν_{tc} is given by (5.12) and N is the Brunt-Vaisala frequency defined as

$$N^2 = \frac{-g}{\rho_m} \quad \frac{\partial \rho_m}{\partial z} \tag{5.44}$$

Though any density distribution can be used to define the Brunt-Vaisala frequency, approximating N as a constant above the mixed layer is sufficient in most cases. In the mixed layer, R is assumed to be dominated by suspended sediment induced stratification and can be written

$$R = \frac{\nu_{tc}}{|\vec{u}_{*c}|^2} \frac{-\sum_n g\,(s_n-1)\,\frac{\partial C_{nm}}{\partial z}}{\left|\frac{\partial \vec{u}_c}{\partial z}\right|} \tag{5.45}$$

Since N in (5.43) is assumed to be given, the iterative procedure to find ζ_c above the mixed layer is to initially assume R=0, calculate $\partial \vec{u}_c/\partial z$, and evaluate (5.43) to find the next guess for R. In (5.45), however, both $\partial C_{nm}/\partial z$ and $\partial \vec{u}_c/\partial z$ are unknown. The iterative procedure to find ζ_c in the mixed layer is to initially assume R=0, calculate $\partial C_{nm}/\partial z$ and $\partial \vec{u}_c/\partial z$, and then evaluate (5.45) to find the next guess for R. Because (5.45) has unknowns in both the numerator and denominator, the convergence rate is much slower in the mixed layer.

To improve the convergence rate, it is proposed that the stability parameter can further be approximated in the mixed layer using the constant stress layer approximations to ν_{tc}, $-\overline{C'_n w'}$ and $-\overline{\vec{u}'w'}$ in (5.17). The resulting stability parameter can be written as

$$\zeta_c = \frac{z}{L_c} = \frac{\kappa\,|\vec{u}_{*c}|\,z}{|\vec{u}_{*c}|^4} \sum_n g\,(s_n-1)\,W_{fn}\,C_{mn} \tag{5.46}$$

where C_{mn} is given by (4.46). Because (5.46) is independent of $\partial \vec{u}_c/\partial z$, given $|\vec{u}_{*c}|$, (5.46) and (4.46) can be solved iteratively for ζ_c in considerably less time than (5.21) and (5.45). Using (4.46) of course will over-predict the sediment concentrations above the constant stress layer, but sediment concentrations in this region are usually insignificant for most applications. Even though C_{mn} is overestimated above the constant stress layer, the local momentum flux $\rho\ |\overrightarrow{-u'w'}|$ is also overestimated by the constant stress layer momentum flux $\rho\ |\vec{u}_{*c}|$. The stability parameter given by (5.46) and (4.46) therefore remains the correct order of magnitude unless z_m is very large. Because it is most important to properly model the stability parameter in the constant stress layer where vertical gradients are large, using (5.46) rather than the generalized stability parameter throughout the mixed layer has little effect on the current profiles. Equation (5.46) therefore is a useful approximation for the stability parameter in the mixed layer.

5.1.7 Solution for the current

For a quasi-steady Ekman layer, equation (5.28) for the current can be written in component form as

$$-f\,v_c = -\frac{1}{\rho}\frac{\partial p_c}{\partial x} + \frac{\partial}{\partial z}\left(\nu_{tm}\frac{\partial u_c}{\partial z}\right) \tag{5.47}$$

$$f\,u_c = -\frac{1}{\rho}\frac{\partial p_c}{\partial y} + \frac{\partial}{\partial z}\left(\nu_{tm}\frac{\partial v_c}{\partial z}\right) \tag{5.48}$$

The current in the wave boundary layer is in the constant stress layer where the stress divergence terms in (5.47) and (5.48) dominate the pressure and Coriolis terms. Assuming the time average bottom stress is in the x-direction, equations (5.47) and (5.48) for the current in the wave boundary layer can be written

$$\nu_{tcw} \frac{\partial u_c}{\partial z} = |\vec{u}_{*c}|^2 \qquad z < \delta_w \tag{5.49}$$

and

$$\nu_{tcw} \frac{\partial v_c}{\partial z} = 0 \qquad z < \delta_w \tag{5.50}$$

Using (4.35) for the neutral eddy viscosity and applying the no slip boundary condition at z_o, the solution for the current in the wave boundary layer is as before

$$u_c = \frac{|\vec{u}_{*c}|}{\kappa} \frac{|\vec{u}_{*c}|}{|\vec{u}_{*cw}|} \ln \frac{z}{z_o} \quad \text{and} \quad v_c = 0 \qquad z < \delta_w \tag{5.51}$$

Above the Ekman layer, the stress divergence terms are negligible and the current is in geostrophic balance with the pressure gradient,

$$-f v_g = -\frac{1}{\rho} \frac{\partial p_c}{\partial x} \qquad z > \delta_c \tag{5.52}$$

$$f u_g = -\frac{1}{\rho} \frac{\partial p_c}{\partial y} \qquad z > \delta_c \tag{5.53}$$

where (u_g, v_g) is the geostrophic current velocity and δ_c is the height of the current boundary layer. Making the usual boundary

layer assumption that the pressure gradients do not vary over the depth of the Ekman layer, (5.52) and (5.53) can be used to rewrite (5.47) and (5.48) as

$$- f (v_c - v_g) = \frac{\partial}{\partial z} \left[\nu_{tm} \frac{\partial}{\partial z} (u_c - u_g)\right] \tag{5.54}$$

$$f (u_c - u_g) = \frac{\partial}{\partial z} \left[\nu_{tm} \frac{\partial}{\partial z} (v_c - v_g)\right] \tag{5.55}$$

Equations (5.54) and (5.55) must be solved for the current velocity in the region $\delta_w \leq z \leq \delta_c$. The boundary conditions on these equations are that the current velocity approach the geostrophic velocity at the top of the Ekman layer

$$u_c \to u_g \quad \text{and} \quad v_c \to v_g \qquad \text{as } z \to \delta_c \tag{5.56}$$

and that the mean shear stress is continuous across the wave boundary layer

$$\nu_{tm} \frac{\partial u_c}{\partial z} = |\vec{u}_{*c}|^2 \quad \text{and} \quad \nu_{tm} \frac{\partial v_c}{\partial z} = 0 \quad \text{at} \quad z = \delta_w \tag{5.57}$$

Because equations (5.54) and (5.55) subject to the boundary conditions (5.56) and (5.57) must be solved numerically for the general eddy diffusivity profile considered here, the equations and boundary conditions will be rearranged into convenient forms for numerical solution. The complex velocity w can be defined as

$$w = (u_c - u_g) + i (v_c - v_g) \tag{5.58}$$

and the eddy diffusivity can be written as

$$\nu_{tm} = \kappa \left|\vec{u}_{*c}\right| z \quad F(z) \tag{5.59}$$

where

$$F(z) = \frac{e^{-2.4\, z/l_c}}{\gamma + \beta\, \zeta_c} \tag{5.60}$$

The momentum equations (5.54) and (5.55) become

$$\frac{\partial}{\partial z} \frac{\kappa \left|\vec{u}_{*c}\right|}{f} z\, F(z) \frac{\partial w}{\partial z} - iw = 0 \qquad \delta_w \leq z \leq \delta_c \tag{5.61}$$

and the respective boundary conditions (5.57) and (5.56) become

$$z\, F(z) \frac{\partial w}{\partial z} = \frac{\left|\vec{u}_{*c}\right|}{\kappa} \qquad \text{at } z = \delta_w \tag{5.62}$$

and

$$w \to 0 \qquad \text{as } z \to \delta_c \tag{5.63}$$

Defining a non-dimensional vertical coordinate ξ as

$$\xi = \frac{f}{\kappa \left|\vec{u}_{*c}\right|} z = \frac{z}{l_c} \tag{5.64}$$

equations (5.61), (5.62) and (5.63) can be written in the non-dimensional coordinate system as

$$\frac{\partial}{\partial \xi} \xi\, F(\xi) \frac{\partial w}{\partial \xi} - iw = 0 \qquad \xi_w < \xi < \xi_c \tag{5.65}$$

$$\xi\ F\ (\xi)\ \frac{\partial w}{\partial \xi} = \frac{|\overset{\rightarrow}{u_{*c}}|}{\kappa} \qquad \text{at } \xi = \xi_w \tag{5.66}$$

$$w \to 0 \qquad \text{as } \xi \to \xi_c \tag{5.67}$$

where ξ_w and ξ_c are the non-dimensional wave boundary layer and current boundary layer heights defined as

$$\xi_w = \delta_w / l_c \tag{5.68}$$

and

$$\xi_c = \delta_c / l_c \tag{5.69}$$

Because the solution to (5.65) is expected to exhibit approximately logarithmic behavior in the near bottom region, a new vertical coordinate χ is defined as

$$\chi = \ln \frac{z}{\delta_w} = \ln \frac{\xi}{\xi_w} \tag{5.70}$$

The momentum equation (5.65) and boundary conditions (5.66) and (5.67) in the logarithmic coordinate system become

$$\frac{\partial^2 w}{\partial \chi^2} + \frac{1}{F\ (\chi)}\ \frac{\partial F}{\partial \chi}\ \frac{\partial w}{\partial \chi} - i\ \frac{\xi_w\ e^{\chi}}{F\ (\chi)}\ w = 0 \qquad \chi_w \leq \chi \leq \chi_c \tag{5.71}$$

$$\frac{\partial w}{\partial \chi} = \frac{1}{F\ (\chi)}\ \frac{|\overset{\rightarrow}{u_{*c}}|}{\kappa} \qquad \text{at } \chi = \chi_w = 0 \tag{5.72}$$

$$w \to 0 \qquad \text{as } \chi \to \chi_c = \ln \frac{\xi_c}{\xi_w} \tag{5.73}$$

After transformation, F (χ) becomes

$$F(\chi) = \frac{\exp(-2.4\,\xi_w\, e^{\chi})}{1 + \beta\,\zeta_c} \tag{5.74}$$

Several forms for the stability parameter in (5.74) are available. For the simplest case of a neutral Ekman layer, $\zeta_c = 0$. In the most general case when stratification is caused by temperature, salinity, and suspended sediment throughout the Ekman layer, the stability parameter is

$$\zeta_c = \frac{1}{2}\left(R - \frac{\gamma}{\beta}\right) + \left[\frac{1}{4}\left(R - \frac{\gamma}{\beta}\right)^2 + \frac{R}{\beta}\right]^{1/2} \tag{5.75}$$

where R after transformation is given by

$$R = \frac{\kappa}{|\vec{u}_{*c}|}\,(\delta_w e^{\chi})^2 \exp(-2.4\,\xi_w e^{\chi})\,\frac{\left[N^2 - \sum_n g\,(s_n - 1)\,(\delta_w e^{\chi})^{-1}\,\frac{\partial C_{nm}}{\partial \chi}\right]}{\left[\left(\frac{\partial u_c}{\partial \chi}\right)^2 + \left(\frac{\partial v_c}{\partial \chi}\right)^2\right]^{1/2}} \tag{5.76}$$

If the Ekman layer can be divided into an upper layer where stratification is dominated by temperature and salinity and a lower mixed layer where stratification is dominated by suspended sediment, R in the upper layer is found by neglecting $\sum_n g\,(s_n - 1)\,(\delta_w e^{\chi})^{-1}\,\partial C_{nm}/\partial x$ in (5.76) while R in the mixed layer is found by neglecting N^2 in (5.76). If only the velocity profile and not the actual suspended sediment concentrations are required above the constant stress layer, or if the constant

stress layer and mixed layer heights are approximately equal, a convenient approximation to the mixed layer stability parameter after transformation is

$$\zeta_c = \frac{z}{L_c} = \frac{\kappa |\vec{u}_{*c}| \delta_w e^{\chi}}{|\vec{u}_{*c}|^4} \sum_n g (s_n - 1) w_{fn} C_{nm} (\chi) \tag{5.77}$$

The numerical implicit difference method used to solve this boundary value problem is described in Appendix I.

If $F(\chi) = 1$, corresponding to a linear eddy viscosity profile with no exponential modulation and no stratification correction, an analytic solution to the above boundary value problem exists. Since the momentum fluxes are being modeled by an eddy viscosity multiplied by a vertical velocity gradient, it is most important to model the eddy viscosity correctly where velocity gradients are large. For a neutral flow, $F(\chi) \sim 1$ in the constant stress layer where velocity gradients are large. $F(\chi)$ is significantly less than 1 only in the upper part of the Ekman layer where velocity gradients are small. The analytic solution for $F(\chi) = 1$ therefore is discussed here since it is expected to exhibit the same qualitative features as the numerical solution for the general eddy diffusivity profile.

Assuming $F(\xi) = 1$, the analytic solution to (5.65) is

$$w = A (\mathrm{Ber}\, 2\xi^{1/2} + i\, \mathrm{Bei}\, 2\xi^{1/2}) + B (\mathrm{Ker}\, 2\xi^{1/2} + i\, \mathrm{Kei}\, 2\xi^{1/2}) \tag{5.78}$$

which is similar to the wave solution in the wave boundary layer.

Applying boundary condition (5.67) requires that A = 0. The resulting solution for the complex velocity found by applying boundary condition (5.66) with F (ξ) = 1 is

$$w = \frac{|\vec{u}_{*c}|}{\kappa} \xi_w^{-1/2} \frac{\text{Ker } 2\xi^{1/2} + i \text{ Kei } 2\xi^{1/2}}{\text{Ker' } 2\xi_w^{1/2} + i \text{ Kei' } 2\xi_w^{1/2}} \tag{5.79}$$

where Ker, Kei, Ker', and Kei' are zeroth order Kelvin functions and their derivatives. Mathematically, $w > 0$ for values of ξ between 2 and 4. Using the actual F (ξ) instead of F (ξ) = 1 will cause $w > 0$ for even lower values of ξ.

Using the small argument approximations found in Abramowitz and Stegun (1972) for the Kelvin functions in (5.79), the near bottom complex velocity can be written

$$(u_c - u_g) + i\,(v_c - v_g) = \frac{|\vec{u}_{*c}|}{\kappa}(\ln \xi + 1.1544 + i\,\pi/2) \tag{5.80}$$

The geostrophic velocity can be found by matching (5.80) and (5.51) at the top of the wave boundary layer. Solving for the geostrophic velocity gives

$$u_g = \frac{|\vec{u}_{*c}|}{\kappa} \frac{|\vec{u}_{*c}|}{|\vec{u}_{*cw}|} \ln \frac{\delta_w}{z_o} - \frac{|\vec{u}_{*c}|}{\kappa}(\ln \xi_w + 1.1544) \tag{5.81}$$

and

$$v_g = -\frac{|\vec{u}_{*c}|}{\kappa} \frac{\pi}{2} \tag{5.82}$$

Note that both u_g and v_g are properly scaled by $|\vec{u}_{*c}|$ and that u_g also depends on the non-dimensional wave boundary layer height ξ_w.

Using (5.81) and (5.82) for the geostrophic velocities, the near bottom current velocities above the wave boundary layer are found from (5.80) to be

$$u_c = \frac{|\vec{u}_{*c}|}{\kappa} \ln \frac{z}{z_{oc}} \quad \text{and} \quad v_c = 0 \tag{5.83}$$

where

$$\frac{z_{oc}}{z_o} = \left(\frac{\delta_w}{z_o}\right)^{1 - |\vec{u}_{*c}| / |\vec{u}_{*cw}|} \tag{5.84}$$

For $F(\xi) = 1$, the Ekman layer velocity profile remains logarithmic near the bottom with the same definition of z_{oc} as in the near bottom models. The definition of z_{oc} is not expected to change when either the exponential modulation or the stratification correction is included in the eddy diffusivity profile since the neutral eddy viscosity will still be approximately linear near the bottom and stratification has not affected any previous definitions of z_{oc}.

5.1.8 Solution procedure

Because the Ekman layer model includes the effects of Coriolis acceleration as well as temperature and salinity stratification, the

Coriolis parameter and the Brunt-Vaisala frequency are included as input variables. Using the master velocity and length scales $|\vec{u}_b|$ and A_b, the basic dimensionless input parameters for the Ekman layer model are

$$\frac{|\vec{u}_r|}{|\vec{u}_b|}, \frac{z_r}{A_b}, \phi_r, \frac{k_b}{A_b}, \frac{g A_b}{|\vec{u}_b|^2}, \frac{f A_b}{|\vec{u}_b|} \quad \text{and} \quad \frac{N A_b}{|\vec{u}_b|} .$$

where $|\vec{u}_r|$ is the current speed specified at any height z_r and ϕ_r is the relative angle between $\vec{u}_r$ and $\vec{u}_b$. If z_r is in the current constant stress layer, $\phi_r \sim \bar{\phi}_c$. Coriolis acceleration, however, causes turning of the current velocity vector above the constant stress layer, so $\phi_r \neq \bar{\phi}_c$ in general. Since the current velocity vector always turns toward the left in the Northern Hemisphere as the bottom is approached, the value of $\bar{\phi}_c$ is different for positive and negative values of ϕ_r. Therefore, unlike $\bar{\phi}_c$, ϕ_r must be specified in the range $-90^\circ \leq \phi_r \leq 90^\circ$. The two new input parameters are the Coriolis parameter and the Brunt-Vaisala frequency nondimensionalized by the wave frequency. If suspended sediment induced stratification is to be included, additional dimensionless input parameters required for each sediment class are as before

$$s_n, S_{*n}, \frac{[(s_n-1)\, g\, d_n]^{1/2}}{|\vec{u}_b|}, \text{ and } C_{nm}(z_o) .$$

The iterative procedure used to solve the Ekman layer model equations again is similar to the method described in Section 3.1.5. In this case, however, both $|\vec{u}_a| / |\vec{u}_b|$ and $\bar{\phi}_c$ are unknowns that must be found. The initial guesses for $|\vec{u}_a| / |\vec{u}_b|$ and $\bar{\phi}_c$, as usual, are used to find ϕ_c, α, V_2, f_{cw}, $|\vec{u}_{*c}|$, $|\vec{u}_{*cw}|$, δ_w, and z_{oc}. The Ekman layer equations (5.71), (5.72), and (5.73) along with the desired stability parameter profile are then solved simultaneously for the current velocity profile. If the calculated current speed and direction at z_r do not match the known values of $|\vec{u}_r|$ and ϕ_r, the procedure is repeated for new values of $|\vec{u}_a| / |\vec{u}_b|$ and $\bar{\phi}_c$. An efficient procedure to find the proper values of $|\vec{u}_a| / |\vec{u}_b|$ and $\bar{\phi}_c$ is discussed in Appendix 1.

For a known stability parameter profile, the Ekman layer equations (5.71), (5.72) and (5.73) must be solved numerically. For the simplist case of a neutral Ekman layer, $\zeta_c = 0$ and the Ekman layer equations need only be solved once. If the general stability parameter (5.75) with R given by (5.76) is used, however, an iterative solution is required since the velocity gradients in (5.76) are not known yet. Initially assuming $\zeta_c = 0$, (5.39) is evaluated for the mean concentration profile, (5.71) is solved numerically for the current velocity profile, and a new stability parameter profile is found from (5.75) and (5.76). These steps are repeated until the correct stability parameter profile is established. For the generalized stability parameter, this solution technique is a time consuming process that must be repeated every time new values of

$|\vec{u}_a| / |\vec{u}_b|$ and $\bar{\phi}_c$ are guessed. It therefore is desirable to simplify the stability parameter as much as possible.

The stability parameter is simplified if the Ekman layer can be divided into an upper layer where stratification is dominated by temperature and salinity and a lower mixed layer dominated by suspended sediment induced stratification. Because the Brunt-Vaisala frequency is given, the only remaining unknown in the stability parameter in the upper layer is the current velocity gradient. In the mixed layer, however, both the mean sediment concentrations and the current velocity gradients in the stability parameter remain unknown, so there is little improvement in the convergence rate for the mixed layer stability parameter. If the constant stress layer approximation for the stability parameter can be used in the mixed layer, however, the stability parameter can be calculated independent of the current velocity profile. Equations (5.77) and (4.46) therefore can be solved for the stability parameter as in Section 4.1.8 before the Ekman layer equations are solved numerically for the current velocity profile. This method saves considerable time since iterations are required to find the stability parameter in the upper layer only.

5.2 Ekman Layer Model Runs

The Ekman layer model described in the previous section was run for three cases to illustrate how the Ekman layer velocity profile depends on the assumed form of the eddy viscosity. The effect of the

exponential decay factor in (5.12) and the temperature and salinity stratification correction in (5.75) and (5.76) are discussed. The dimensionless input parameters listed in Section 5.1.8 required to run the Ekman layer model are calculated using typical data collected by Grant and Williams on the northern California shelf.

Typical conditions for the wave are $|\vec{u}_b|$ = 10 cm/sec and A_b = 25 cm and for the current are $|\vec{u}_r|$ = 10 cm/sec and $\phi_r = 0^\circ$ at z_r = 100 cm. The physical bottom roughness is assumed to be k_b = 6 cm. The acceleration of gravity and the Coriolis parameter are taken as $g = 980$ cm/sec^2 and $f = 0.0001$ rad/sec. The Brunt-Vaisala frequency is assumed to be N = 3 cycles/hour = 0.005 rad/sec above the mixed layer height z_m = 15 meters and N=0 below z_m. These values are used to calculate the necessary dimensionless input parameters. For comparison, the typical Ekman layer height during the experiment was of order 40 meters.

For the first model run, stratification was neglected and the linear eddy viscosity given by (3.24) was used. This corresponds to the analytic solution (5.79) of the Ekman layer equations. The resulting Ekman layer velocity profile and turning angle are plotted in Figures 5.2 and 5.3. For comparison, the solution predicted by the neutral near bottom model is also plotted in Figure 5.2. For this case, the Ekman layer model predicted the wave boundary layer height to be δ_w = 4.8 cm. Inside the wave boundary layer, the current velocity profile is characterized by the maximum shear

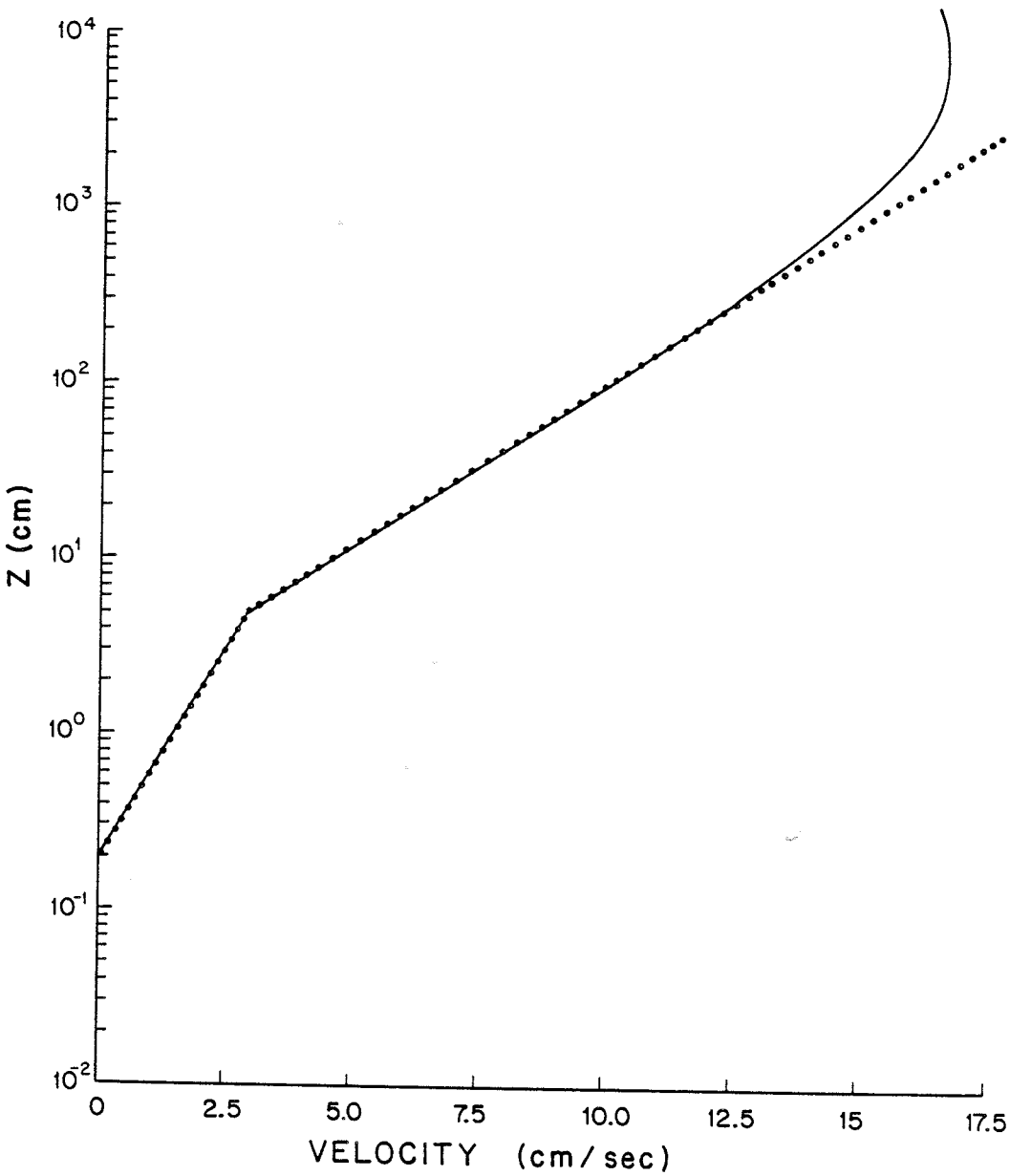

FIGURE 5.2

Current velocity profile predicted by the Ekman layer model with linear eddy viscosity and no stratification (solid line) compared to the neutral near bottom model (dotted line).

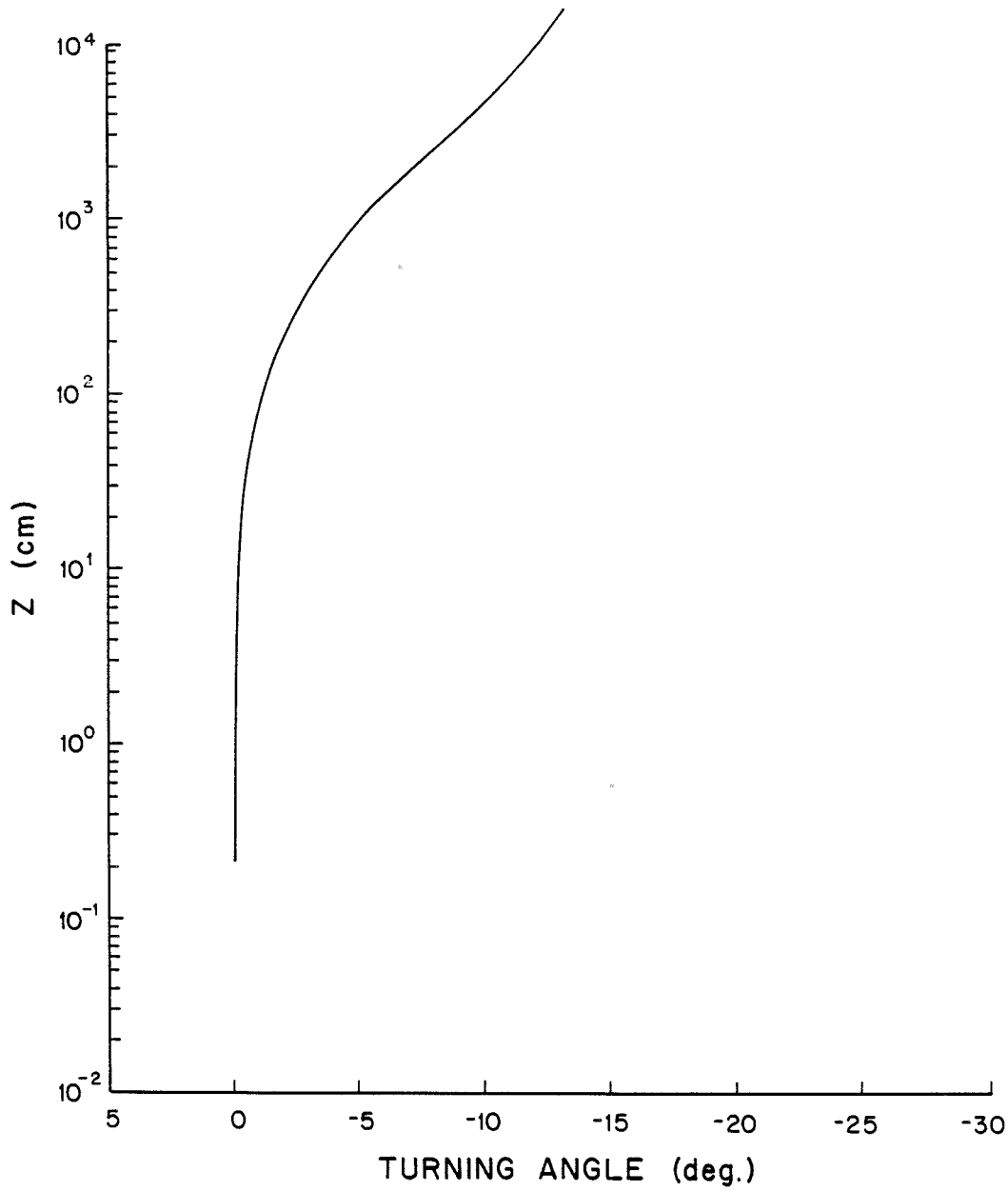

FIGURE 5.3
Current turning angle predicted by the Ekman layer model with linear eddy viscosity and no stratification.

velocity $|\vec{u}_{*cw}|$ = 2.4 cm/sec and the physical bottom roughness z_o = 0.2 cm. Above the wave boundary layer, the current is characterized by the shear velocity $|\vec{u}_{*c}|$ = 0.94 cm/sec and the apparent bottom roughness z_{oc} = 1.4 cm. From (5.11), the scale height of the Ekman layer is l_c = 38 meters. From (5.81) and (5.82), the magnitude and turning angle of the geostrophic velocity is $|\vec{u}_g|$ = 16 cm/sec and θ_g = - 13°. The current velocity profile approachs the geostrophic values for $z = \delta_c \sim 80$ meters. The Ekman layer velocity profile does not begin to deviate from the near bottom model solution until $z \sim 4$ m. The predicted turning angle below this height is less than 3°. Coriolis acceleration therefore has little effect on the velocity profiles for heights less than $z \sim 0.1\ l_c$, which is taken as the approximate height of the constant stress layer.

For the second model run, stratification again was neglected but the eddy viscosity given by (5.12) that includes the exponential decay factor was used. The velocity profile and turning angle predicted by the Ekman layer model are plotted in Figures 5.4 and 5.5. For comparison, the velocity profile and turning angle predicted using a linear eddy viscosity are also plotted. Because the current speed $|\vec{u}_r|$ was specified well within the constant stress layer ($z_r < 0.1\ l_c$) where (5.12) is still approximately linear, there is negligible change in the parameters associated with the near bottom velocity profile and in the scale height of the Ekman layer. In the upper Ekman layer, however, the reduced vertical turbulent momentum transport requires a larger geostrophic velocity

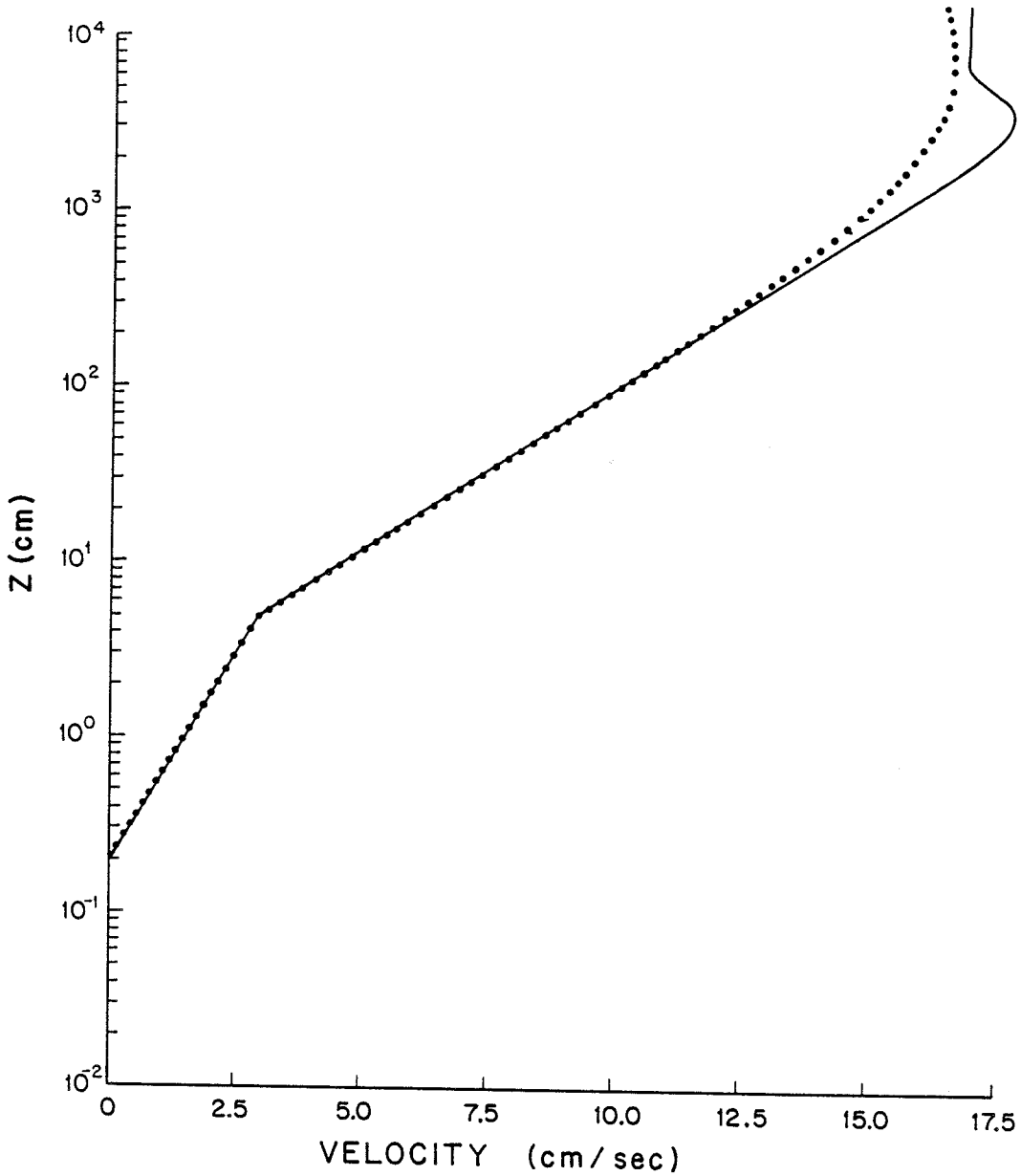

FIGURE 5.4
Current velocity profile predicted by the Ekman layer model with modulated eddy viscosity and no stratification (solid line) compared to the Ekman layer model with linear eddy viscosity and no stratification (dotted line).

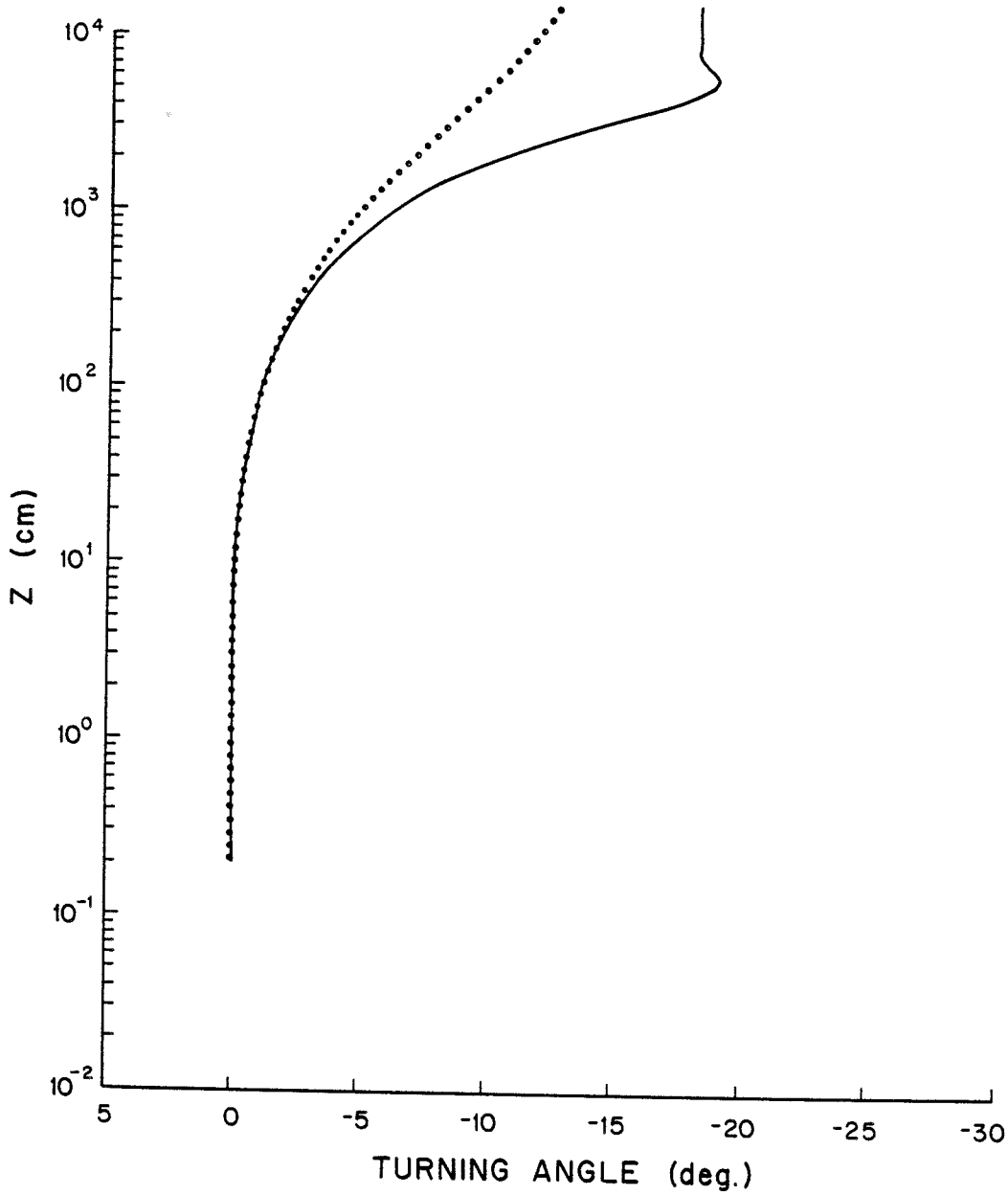

FIGURE 5.5
Current turning angle predicted by the Ekman layer model with modulated eddy viscosity and no stratification (solid line) compared to the Ekman layer model with linear eddy viscosity and no stratification (dotted line).

to give the same boundary shear stress. The magnitude and turning angle of the geostrophic velocity are $|\vec{u}_g| = 17$ cm/sec and $\theta_g = -18°$. The Ekman layer height is reduced to $\delta_c = 50$ meters, the velocity and turning angle at any given height is increased, and the velocity overshoot at the top of the Ekman layer is increased. Even though the neutral eddy viscosity in the upper Ekman layer is drastically reduced by the exponential decay factor as illustrated in Figure 5.1, the velocity profile is changed by less than 10 percent. The most significant difference caused by the exponential decay factor is the increase in the turning angle.

For the final model run, temperature and salinity stratification was included with the neutral eddy viscosity given by (5.12). The resulting velocity profile and turning angle are plotted in Figures 5.6 and 5.7 along with the results of the neutral model run. Since the current speed was specified below the mixed layer height, the near bottom flow field and the scale height of the Ekman layer are the same. Because stratification inhibits vertical turbulent transport, the geostrophic velocity again must be increased to give the same boundary shear stress. The magnitude and turning angle of the geostrophic velocity in this case are $|\vec{u}_g| = 17.5$ cm/sec and $\theta_g = -14°$. The turning angle again is increased throughout the Ekman layer, but since the Ekman layer height is reduced to $\delta_c \sim 40$ meters, the turning angle for the geostrophic velocity is reduced. The stratification correction in this case was of order 10 for

$z \sim z_m$ and of order 1000 for $z \sim \delta_c$. Even a stability parameter this large changes the velocity at any height by less than 10 percent. The major effect of stratification in this case is to reduce the Ekman layer height.

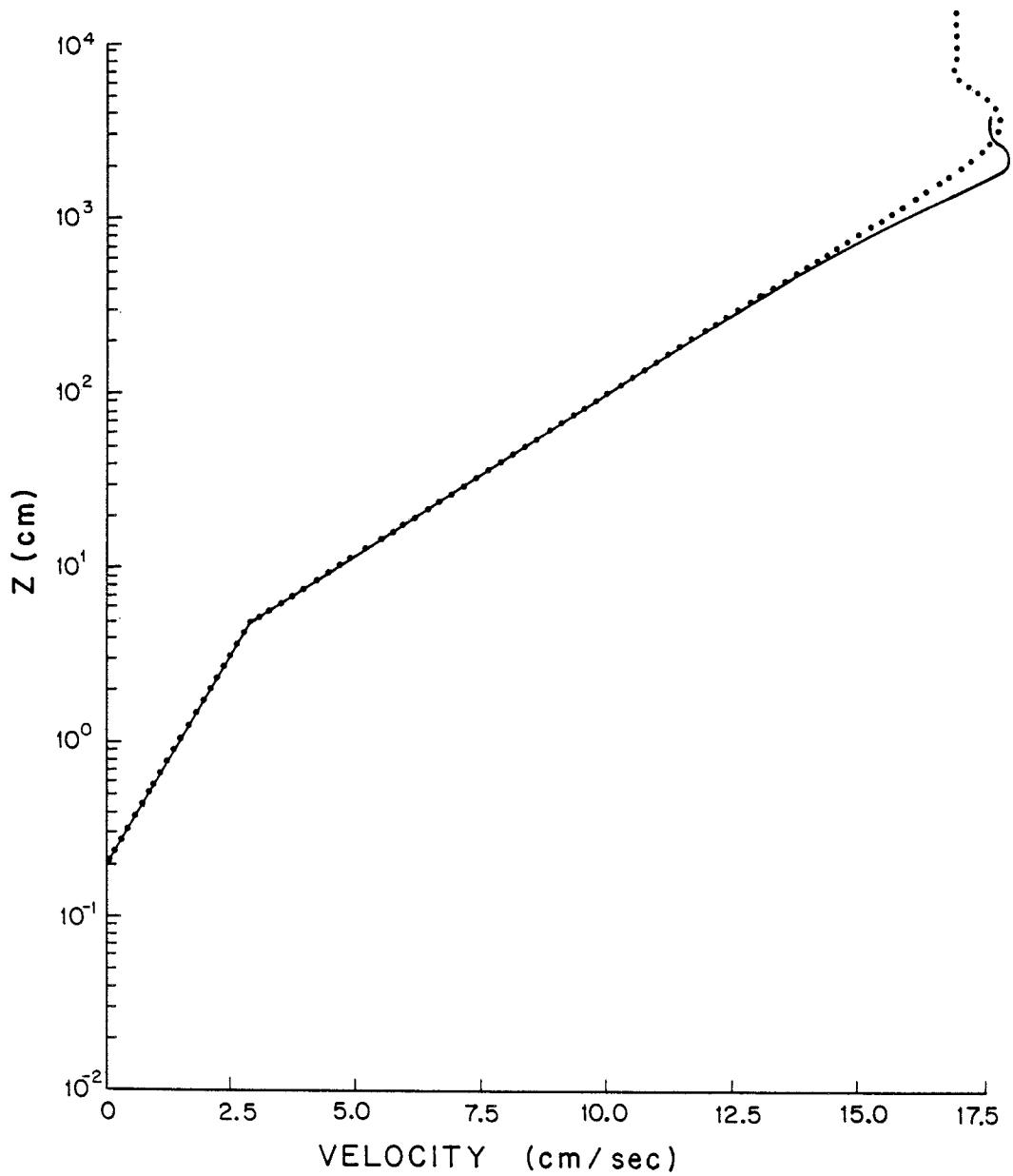

FIGURE 5.6
Current velocity profile predicted by the Ekman layer model with modulated eddy viscosity and T/S stratification (solid line) compared to the Ekman layer model with modulated eddy viscosity and no stratification (dotted line).

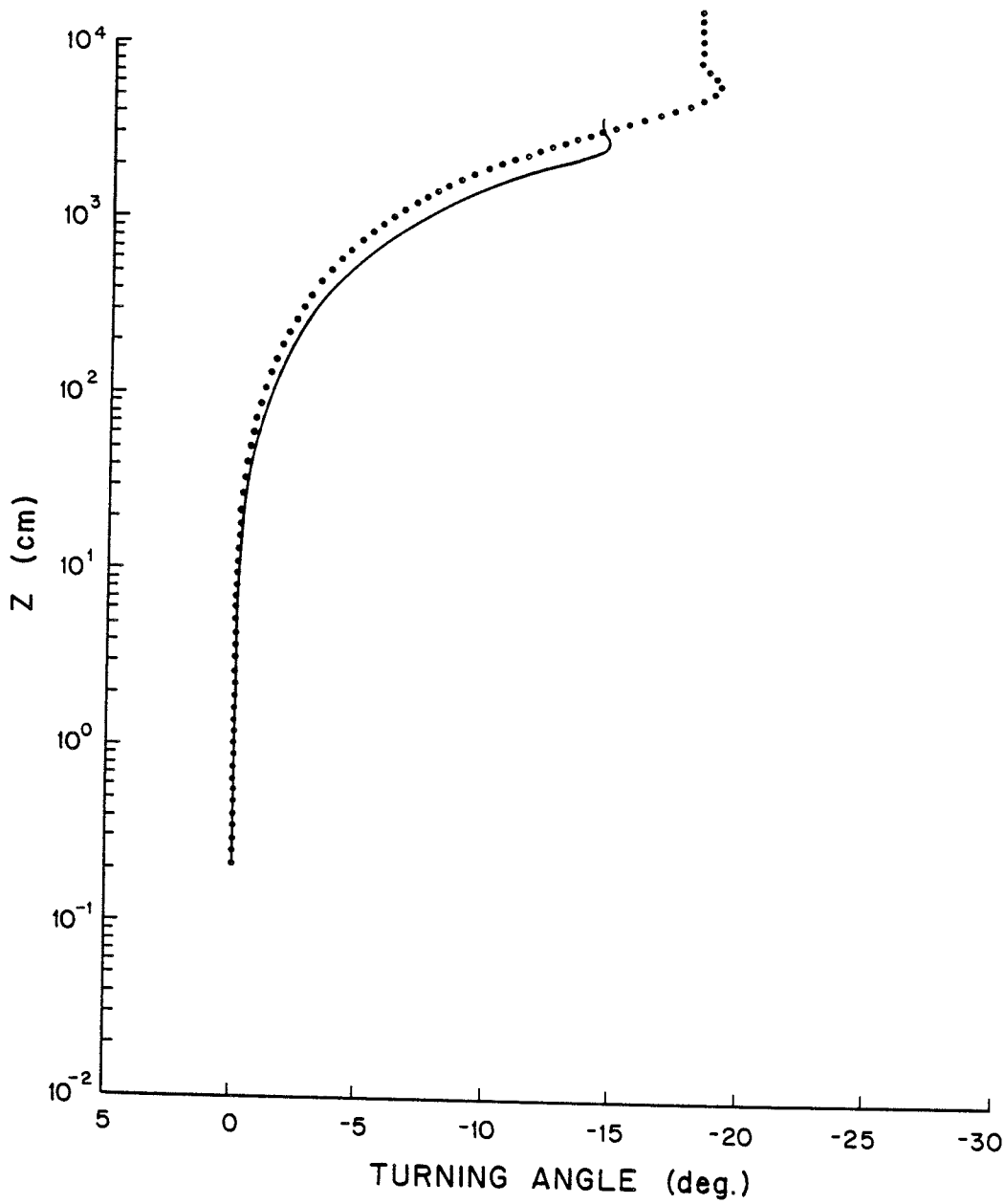

FIGURE 5.7
Current turning angle predicted by the Ekman layer model with modulated eddy viscosity and T/S stratification (solid line) compared to the Ekman layer model with modulated eddy viscosity and no stratification (dotted line).

6. MODEL COMPARISON WITH CONTINENTAL SHELF, BOTTOM BOUNDARY LAYER DATA

Two data sets have been selected for comparison with the bottom boundary layer model. Both were obtained during the recent Coastal Ocean Dynamics Experiment (CODE) on the northern California shelf between Point Arena and Point Reyes. The two data sets cover forcing conditions from strong winds to a design storm, allowing model comparisons for a wide range of flows. The first data set, designated CODE-I, contains detailed flow and support measurements made during strong wind conditions. The second data set, designated CODE Winter Storm has less detailed flow and fewer support measurements, but covers a wider range of conditions including a severe storm. The CODE-I data is from measurements made by Grant and Williams and the Winter Storm data is from measurements made by Cacchione and Drake. The data comparison discussed here is described in detail in Grant and Glenn (in press).

6.1 CODE-I Data

A bottom boundary layer experiment was conducted at the CODE site in early June, 1981 in approximately 100 meters of water. During the experiment, the current speed and direction was variable while the long waves driving the oscillatory flow were relatively constant southern ocean swell. Because the near bottom flow was not strong enough to significantly modify the sediment bed, the CODE-I data provides a test of the wave-current interaction independent of the flow-sediment interaction for a range of relative wave-current strengths and directions.

During the CODE-I bottom boundary layer experiment, near bottom velocity profiles were measured using a vertical array of four acoustic travel time current meters mounted 30, 55, 105, and 205 centimeters above the bottom on a tripod. Designed and built by Williams and Koehler (in prep.), the current meters measured the average velocity over a 15 centimeter averaging length with a precision of 0.3 cm/sec and a sensitivity of 0.06 cm/sec. A pressure sensor mounted 200 centimeters above the bottom was used as an independent measure of wave characteristics and to determine the water depth. Transmissometers mounted 75 and 175 centimeters above the bed were used to measure light attenuation. Thermisters mounted 50, 100, and 200 centimeters above the bottom were used to measure the near bottom temperature profile. A compass, pitch and roll sensor, and a bottom locater were used to determine the tripod location and orientation. All instruments on the tripod were sampled simultaneously at a rate of 5 hertz. Bottom characteristics were determined from bottom photographs, box cores, and side scan sonar. CTD profiles within 0.5 meter of the bottom were systematically taken at the tripod location to determine density profiles throughout the bottom boundary layer. The low frequency characteristics of the flow were determined by nearby vertical arrays of vector measuring current meters and a nearby NBIS acoustic current meter located 2.5 meters above the bottom.

Measurements from a typical 15 hour time period were selected for detailed analysis and comparison with the bottom boundary layer

model. The corresponding time series of flow speed and direction (sampled at 1 hertz and averaged over 3.33 minute intervals) measured by the NBIS acoustic current meter is plotted in Figure 6.1. During this time period, thermisters on the tripod and CTD profiles indicated the existence of a distinct bottom mixed layer of nearly constant density which varied in thickness from 15 to 30 meters. Transmissometers and bottom photographs indicated that less than 2 mg/l of sediment was in suspension. The extensive side scan coverage revealed no large scale topographic features on the bottom at the tripod location. In this case, the time averaged, near bottom velocity profile for a neutral, turbulent flow over a topographically simple bottom is expected to follow a logarithmic velocity law of the form

$$u = \frac{u_*}{\kappa} \ln \frac{z - \delta_D}{z_0} \tag{6.1}$$

where u is the mean velocity, u_* and z_0 are the shear velocity and bottom roughness for the mean flow, and δ_D is the displacement thickness as defined by Jackson (1981). Equation (6.1) therefore can be used to calculate u_* and z_0 from the mean velocity profiles measured by the acoustic current meters at the CODE site and the results compared to values predicted by the bottom boundary layer model.

Before calculating mean velocity profiles, the velocity data was rotated for spectral analysis into a standard turbulent coordinate

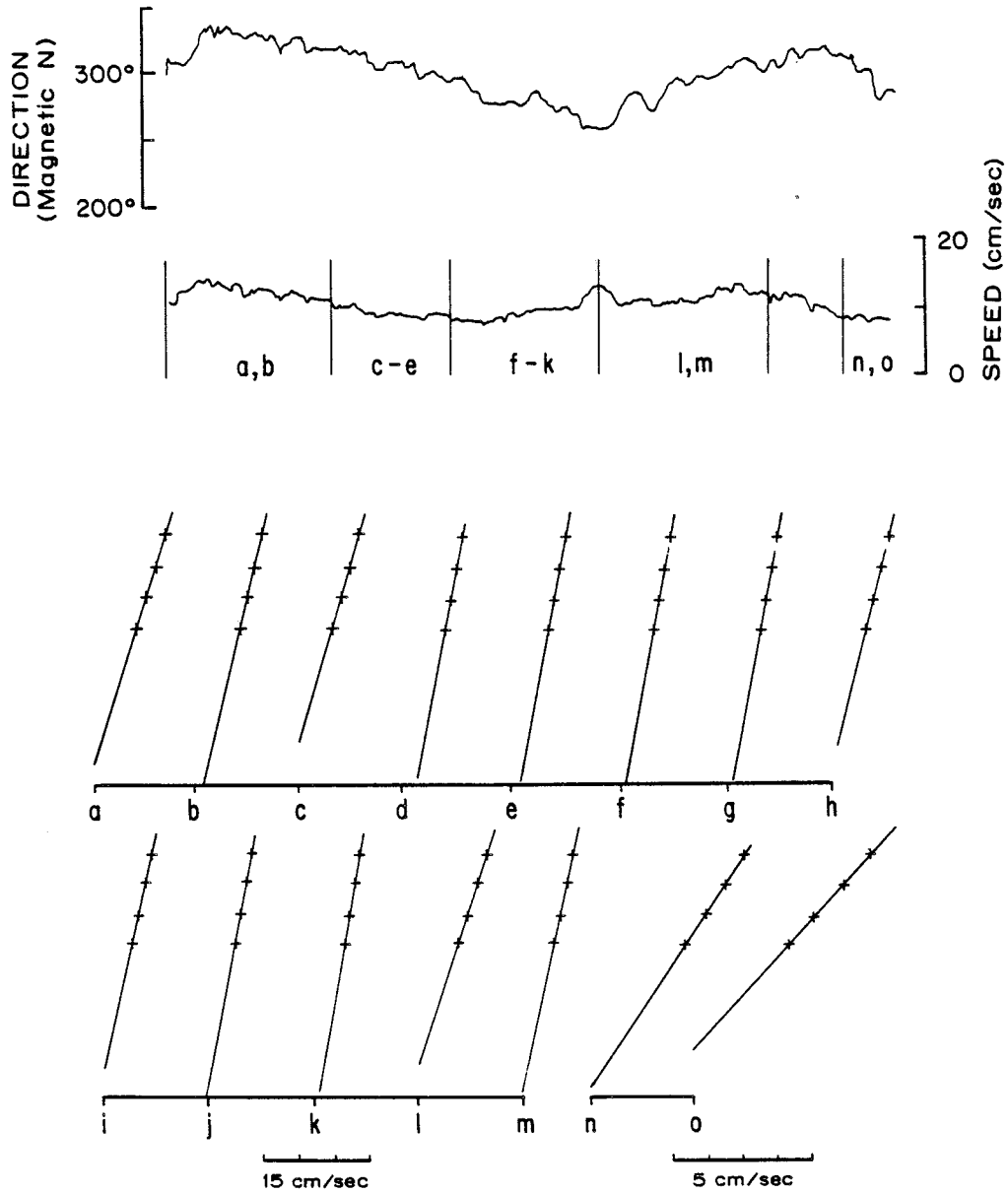

FIGURE 6.1

Measured CODE-I current velocities. Upper plots are current speed and direction measured by the NBIS acoustic current meter 2.5 meters above the bottom (sampled at 1 hertz and averaged over 3.33 minutes for 15 hours). Lower plots are current velocity profiles with log z on the vertical axis and current speed on the horizontal axis. Velocity measurements made by the acoustic current meters 28, 55, 103, and 203 centimeters above the bottom and averaged over 9.33 minutes are indicated by the (+). Also plotted are the best fit straight lines by a least squares linear regression. The approximate time locations of the profiles are indicated on the speed plot.

system such that

$$\vec{u} = (u + u', v', w') \tag{6.2}$$

where u is the time average velocity and u', v', w' are the turbulent fluctuations. Spectral analysis of the resulting velocity time series reveals that it is composed of fluctuations associated with high frequency turbulence, surface waves, internal waves, and low frequency currents. Because the flow was not stationary over time periods comparable to the internal wave period, the mean velocity in (6.2) was calculated by averaging for a time significantly greater than the surface wave period but significantly less than the internal wave period.

To find the mean velocity profiles, the velocity data from the acoustic current meters was time averaged and plotted on a semi-logarithmic scale. The best fit straight line using a least squares linear regression was drawn through the points and the regression coefficient r was calculated. To construct the semi-logarithmic plots, however, a time averaging interval for the velocity data must be selected and the average location of the bottom around the tripod must be estimated. Several averaging intervals much greater than the surface wave period, but much less than the internal wave period, were used to calculate the mean velocities. Averaging intervals between 9 and 14 minutes consistently gave the highest r values. Longer intervals resulted in lower r values due to the non-stationarity of the flow field. Because many turbulent eddies must

be averaged to establish a logarithmic velocity profile (Townsend, 1970), and because the swell had a beat period of about 2 minutes, shorter averaging intervals also resulted in lower r values. A convenient averaging interval of about 9.77 minutes therefore was used for the profile analysis to maximize the correlation coefficient.

Due to the local microtopography, the maximum uncertainty in the average bottom location around the tripod was estimated from the bottom locater and bottom photographs to be about 5 centimeters. The velocity measurements therefore were shifted up and down within the 5 centimeter range to remove any curvature in the velocity profile. The displacement thickness δ_D was estimated to be of order 1 centimeter. Because this is much less than the uncertainty in the bottom location, the zero shift introduced by the displacement thickness can be neglected. Since the profiles were not very sensitive to zero shifts, the current meter heights were chosen by maximizing the regression coefficient for the best fit straight line to the velocity profile. The final current meter heights assumed for the profile analysis were taken as 28, 53, 103, and 203 centimeters above the bottom; a zero shift of 2 centimeters.

After the appropriate time averages and zero shifts were applied, velocity profiles with $r^2 > 0.992$ and no systematic curvature were selected for comparison with the model. The selected velocity profiles and the best fit straight lines are plotted in Figure 6.1. Notice that the velocity profiles appear highly logarithmic. Because internal waves could not be removed by the averaging process, profiles

that passed this criteria correspond to time periods when the internal waves had little effect on the velocity profiles.

Neglecting the displacement thickness, the velocity profile given by (6.1) can be written as

$$\log z = \frac{\kappa}{2.3\, u_*}\, u + \log z_0, \tag{6.3}$$

which is the equation for a straight line on a plot of log z versus u. The slope and z intercept of the best fit straight line to the velocity profiles therefore can be used to determine u_* and z_0. The resulting values of u_*, z_0 and the 95 percent confidence intervals calculated by this method are listed in Table 6.1. Because only highly logarithmic ($r^2 > 0.992$) velocity profiles where chosen for analysis, the error bars on the u_* and z_0 estimates are reasonably small (of order 20 percent for u_* and a factor of 2 for z_0). Velocity profiles with smaller r^2 values result in excessively large error bars on the estimates of u_* and z_0. This suggests that velocity profiles with values of r^2 less than approximately 0.99 may not be truly logarithmic and the logarithmic profile technique should not be used to estimate u_* and z_0.

To establish that the selected profiles were measured in the constant stress layer and can be considered logarithmic, the inertial dissipation technique described by Deacon (1956) was used to calculate an independent estimate of the shear stress. Because it is relatively uncontaminated by the wave, Grant and Glenn (in press) use

Profile	u_*	z_o	R^2	$\lvert\vec{u}_{*c}\rvert$	z_{oc}	$C_{D100}\times10^{-3}$	$\lvert\vec{u}_{100}\rvert/\lvert\vec{u}_b\rvert$	$k_b/\lvert\vec{A}_b\rvert$	ϕ_c(deg)	ω (rad)
a	0.940 (+0.211) (−0.146)	1.46 (+1.6) (−0.77)	0.9963	0.815	0.80	9.0	1.89	0.53	30°	0.459
b	0.704 (+0.093) (−0.128)	0.33 (+0.43) (−0.19)	0.9975	0.852	0.86	4.8	1.76	0.43	30°	0.419
c	0.828 (+0.193) (−0.132)	2.03 (+2.11) (−1.04)	0.9960	0.704	1.0	10.2	1.46	0.46	30°	0.417
d	0.698 (+0.262) (−0.15)	1.71 (+3.22) (−1.12)	0.9920	0.797	0.32	10.1	0.36	0.13	30°	0.423
e	0.580 (+0.185) (−0.114)	0.64 (+1.43) (−0.45)	0.9936	0.650	1.18	6.4	1.13	0.39	30°	0.418
f	0.540 (+0.112) (−0.078)	0.72 (+0.89) (−0.40)	0.9968	0.571	0.97	6.6	1.42	0.54	30°	0.426
g	0.566 (+0.176) (−0.109)	0.99 (+1.79) (−0.64)	0.9940	0.563	1.05	7.7	1.18	0.48	70°	0.441
h	0.501 (+0.194) (−0.110)	0.47 (+1.49) (−0.36)	0.9920	0.562	0.94	5.8	1.35	0.55	70°	0.451
i	0.674 (+0.124) (−0.090)	2.15 (+1.67) (−0.94)	0.9974	0.555	0.90	10.5	1.42	0.55	70°	0.421
j	0.674 (+0.150) (−0.103)	1.91 (+1.90) (−0.95)	0.9964	0.557	0.79	9.9	1.67	0.62	70°	0.423
k	0.530 (+0.041) (−0.033)	0.71 (+0.29) (−0.21)	0.9940	0.607	1.32	6.4	0.91	0.35	70°	0.419
l	0.537 (+0.179) (−0.107)	0.60 (+1.45) (−0.43)	0.9934	0.603	0.98	5.9	1.29	0.46	70°	0.420
m	0.915 (+0.120) (−0.095)	1.83 (+1.00) (−0.65)	0.9986	0.747	0.70	9.6	1.97	0.57	70°	0.449
n	0.602 (+0.158) (−0.103)	0.89 (+1.39) (−0.54)	0.9953	0.630	1.16	7.3	1.14	0.41	30°	0.425
o	0.359 (+0.121) (−0.073)	1.14 (+2.15) (−0.75)	0.9933	0.382	1.42	7.7	0.76	0.48	30°	0.435
p	0.421 (+0.138) (−0.088)	1.55 (+3.02) (−1.44)	0.9950	0.431	1.52	8.6	0.73	0.40	30°	0.413
q	0.391 (+0.167) (−0.089)	1.06 (+2.79) (−0.77)	0.9905	0.584	4.45	7.3	0.19	0.11	30°	0.427

TABLE 6.1

CODE-I DATA

the w' spectra calculated from the acoustic current meter velocity data to estimate the shear velocity at the height of each current meter. For those profiles that the inertial dissipation technique was applied to, calculated shear velocities at each current meter height where within the error bars on the estimates from the velocity profiles and varied between adjacent current meters by less than 10 percent. This confirms that for the selected profiles ($r^2 > 0.992$), the velocity measurements were made in the current constant stress layer and that the assumed logarithmic form for the current velocity profile is consistent.

To compare the values of u_* and z_o calculated from the velocity profiles to those predicted by the neutral near bottom model, the four model input parameters

$$\frac{|\vec{u}_r|}{|\vec{u}_b|}, \frac{z_r}{A_b}, \bar{\phi}_c, \text{ and } \frac{k_b}{A_b}$$

must be specified for the time periods associated with each profile. The input current conditions are taken as the average current speed $|\vec{u}_r|$ measured by the current meter located at z_r = 103 cm for each time period. Assuming a normal distribution for the directional spreading function (Borgman, 1976), directional wave spectra were calculated from the pressure and the two horizontal components of velocity measured by the top current meter to determine the relative direction of the current $\bar{\phi}_c$ with respect to the wave. One dimensional wave spectra calculated from the pressure sensor and

transformed by linear wave theory also agree well with wave spectra calculated from the current meters. While the velocity records contained fluctuations associated with turbulence, surface waves, internal waves, and currents, the pressure record was dominated by the surface waves. Wave input conditions therefore were determined from the pressure record.

A typical pressure record is plotted in Figure 6.2. The wave period is observed to be approximately constant while the amplitude varies over a beating period of about 2 minutes. By keeping track of zero crossings in the pressure records, the average wave period was calculated for each profile. Water depth was calculated from the average pressure. Linear wave theory and the maximum pressure difference then was used to calculate $|\vec{u}_b|$ and A_b. For comparison, the period and pressure difference was found for each wave so that $|\vec{u}_b|$ and A_b could be calculated on a wave by wave basis. The neutral near bottom model was run for each wave and the resulting values of the shear velocity and bottom roughness were averaged together. Compared to the shear velocity and bottom roughness calculated from the mean period and maximum pressure difference, the average values calculated using the wave by wave approach changed the shear velocity by about 10-20 percent and the bottom roughness by about 20-40 percent, having little effect on the velocity profile. This result is expected since the wave envelope is relatively flat. The average wave period and the maximum pressure difference therefore was used for simplicity to calculate $|\vec{u}_b|$ and

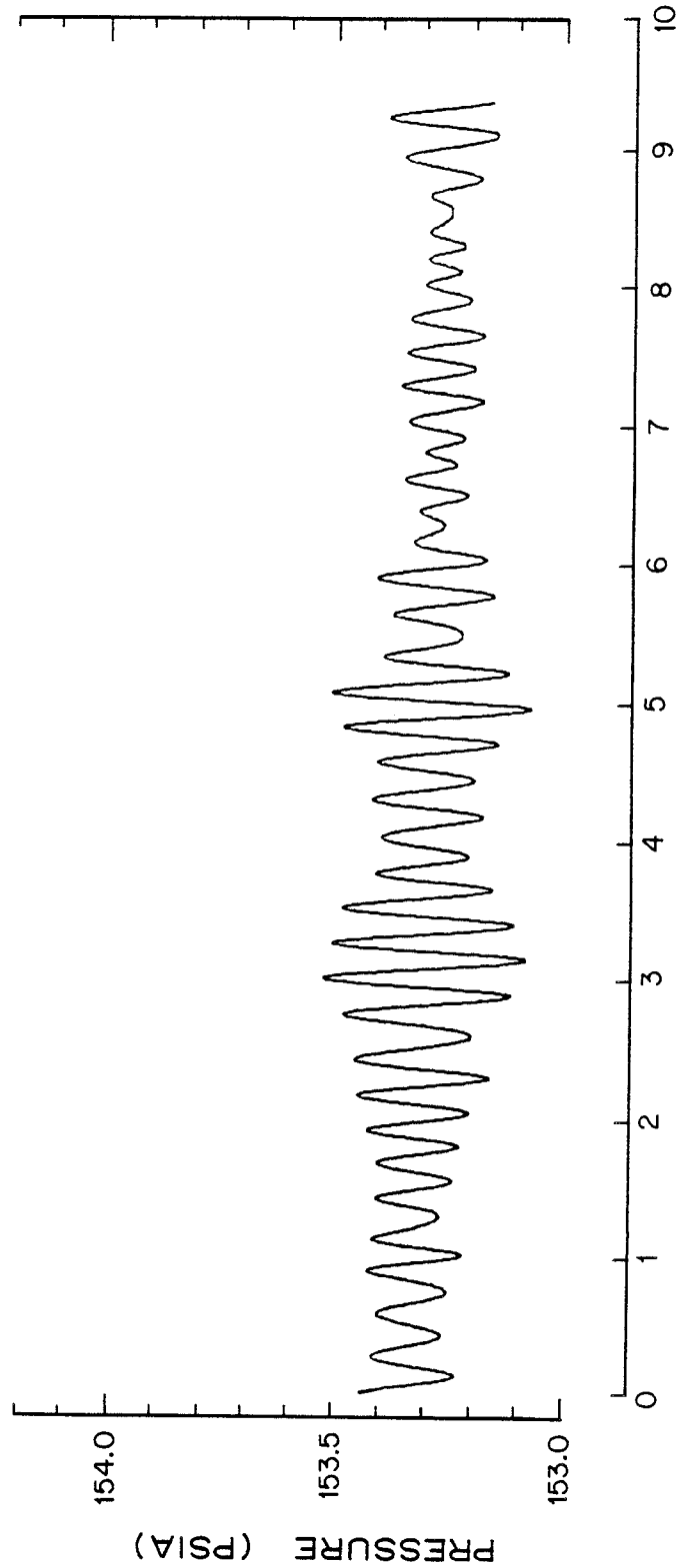

FIGURE 6.2
Typical CODE-I pressure record measured 2 meters above the bottom. This case corresponds in time to profile d.

A_b for the model comparison.

The remaining input condition that must be specified is the physical bottom roughness k_b. Bottom photographs and box cores at the CODE site during the experiment reveal that the bottom was highly bioturbated and sediment transport was negligible. The physical bottom roughness associated with the animal generated mounds and furrows therefore is expected to be constant and can be estimated by the method discussed in Section 3.2.2 for general distributed bedforms. The observed bed features were about 1-4 centimeters high and spaced about 10-20 centimeters apart. The roughness length z_o associated with the bedforms is estimated from (3.66) to be in the range

$$z_o \sim k_h \, (k_h/k_L) \sim (0.1 - 0.5) \text{ cm}. \tag{6.4}$$

The near bottom model was run for different values of z_o in this range. A value of $z_o = 0.2$ cm was selected for the model comparison and held constant for all fifteen profiles.

The input parameters for the neutral near bottom model runs are listed in Table 6.1. In all cases, the wave boundary layer was found to be less than 5 centimeters thick, well below the lowest current meter. The scale height of the Ekman layer, calculated using (5.11) and $f = 9 \times 10^{-5}$ is found to be of order 20-40 meters, so the current meters were within the predicted constant stress layer height of 2-4 meters. The parameters u_* and z_o in (6.3) calculated from the velocity profiles therefore correspond to the model parameters $|\vec{u}_{*c}|$

and z_{oc} in equation (3.59) for the current velocity above the wave boundary layer. The predicted values of $|\vec{u}_{*c}|$ and z_{oc} also are listed in Table 6.1.

The values of u_*, z_o, and the 95 percent confidence intervals estimated from the velocity profiles are plotted in Figure 6.3. Also plotted are the values of $|\vec{u}_{*c}|$ and z_{oc} predicted by the neutral near bottom model. The predicted shear velocity generally was within 10-15 percent of the estimated shear velocity and within the 95 percent confidence intervals. Though estimates of the apparent bottom roughness from velocity profiles are inherently noisy, the model predictions are again in good agreement with the estimates. The constant physical bottom roughness $z_o = 0.2$ is usually well below the error bars on z_{oc}. Because the side scan indicated there were no large scale topographic features, the increased magnitude and variability of the apparent bottom roughness cannot be explained by upstream topography and variable current directions.

The usual nonlinear drag law used on the continental shelf to predict the bottom stress is

$$\tau = \rho C_D (u_{100})^2 \tag{6.5}$$

where C_D is the drag coefficient and u_{100} is the current velocity 1 meter above the bottom. The drag coefficient is usually assumed to be constant and equal to 1.5×10^{-3}. The shear velocity was calculated from (6.5) using $C_D = 1.5 \times 10^{-3}$ and the current measured at $z_r = 103$ centimeters for u_{100}. For comparison, the

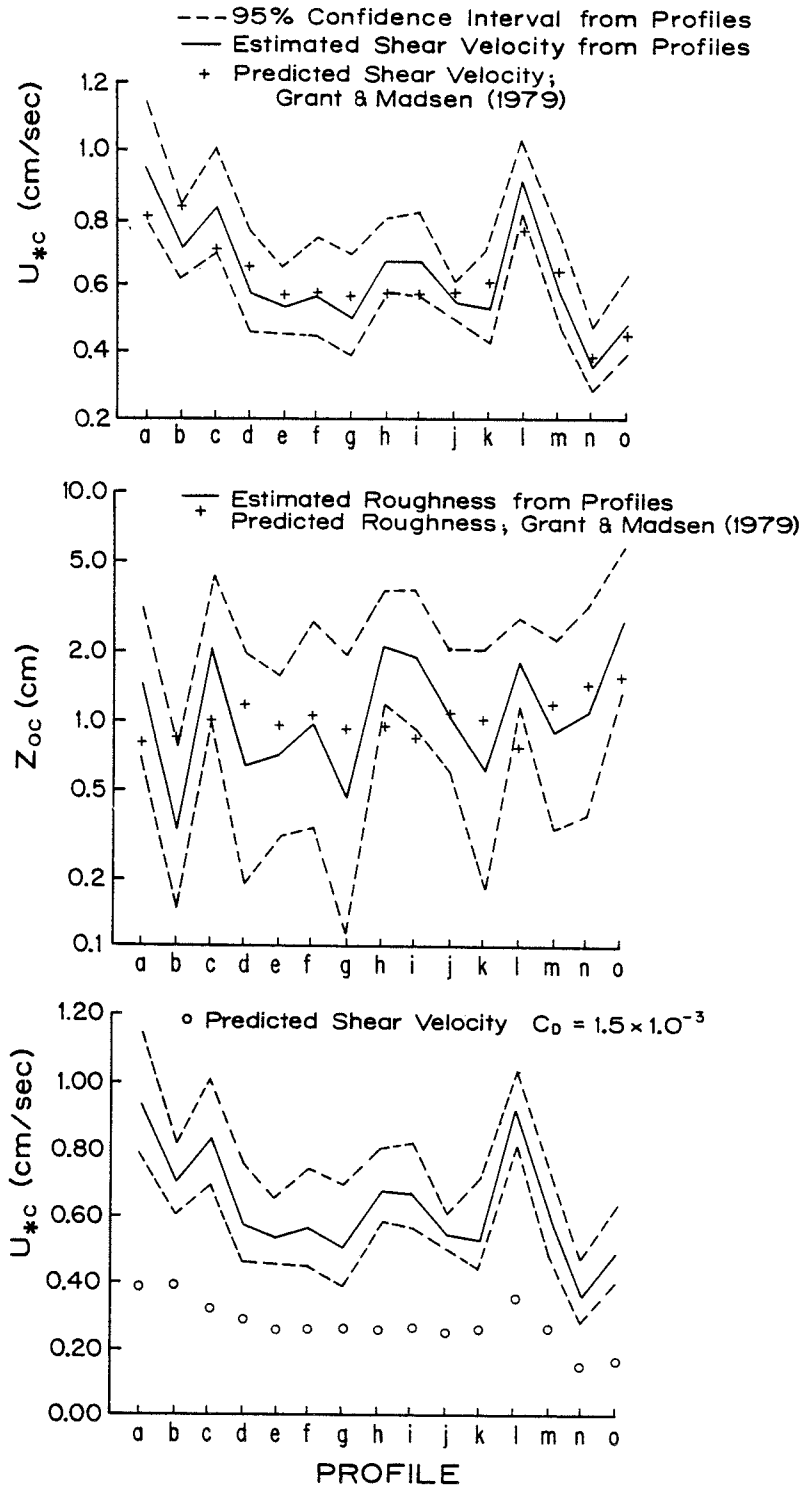

FIGURE 6.3

CODE-I data/model comparison, shear velocity and bottom roughness estimated from measured velocity profiles and predicted by the neutral near bottom model. Also shown is the shear velocity calculated from (6.5) with $C_D = 1.5 \times 10^{-3}$.

resulting values of u_* are plotted in Figure 6.3. Not only is it immediately obvious that this drag coefficient is too low, but even if C_D is arbitrarily increased, a constant drag coefficient still does not predict the observed variability in the shear velocity. The only remaining physical process that can account for the magnitude and variability of the estimated shear velocity and apparent bottom roughness is the surface waves. The ability of the neutral near bottom model to predict the observed values within the estimate error bars is strong support for the theoretical approach used to model a combined wave and current flow field. The actual drag coefficient calculated from the measured velocity at z_r = 103 centimeters and the value of u_* estimated from the profiles is listed in Table 6.1. Clearly, the drag coefficient must be allowed to vary to reflect the influence of the waves when stress estimates are made on the continental shelf.

6.2 CODE Winter Storm Data

Because there was little sediment transport associated with the CODE-I data analyzed in the previous section, confidence was gained in the wave-current interaction portion of the theory independent of the flow-sediment interaction. During the 1981 winter storm at the CODE site, however, significant sediment transport was observed. The CODE Winter Storm data collected by Cacchione and Drake therefore can be compared to the model for the full wave-current-moveable bed interaction.

Data both before and during the storm was analyzed to provide a wide range of flow and sediment transport conditions for comparison. Before the storm, waves and currents were relatively weak, little sediment transport occurred, and the bottom micro-topography was similar to the CODE-I animal generated bedforms. During the storm, strong flow conditions caused intense sediment transport and wave generated ripples dominated the bottom micro-topography.

A detailed description of the data collected during the winter storm using the USGS GEOPROBE tripod can be found in Cacchione et al. (in prep.). Using a vertical array of electromagnetic current meters, the GEOPROBE measured the two components of horizontal velocity 20.3, 51.4, 66.7, and 98.4 centimeters above the bottom. Pressure, temperature, and light transmission were also measured 2 meters above the bottom. Every two hours, the GEOPROBE collected 272 seconds of data sampled at 0.5 hertz and took a bottom photograph. Box cores, water samples, high frequency seismics, and an underwater television camera were also used to define the bottom and suspended sediment characteristics.

The CODE Winter Storm data was analyzed similar to the CODE-I data. Mean velocity profiles were found by averaging the current meter data over each 272 second burst and plotting the result on a semi-logarithmic scale. Only data from the lowest three current meters was used since the top current meter was not functioning properly during the storm. A straight line was fit to the data by a linear least squares regression and the regression coefficient was

calculated. As with the CODE-I data, the uncertainty in the average bottom location around the GEOPROBE was assumed to be 5 centimeters, again, much greater than the displacement thickness. The data therefore was zero shifted in the 5 centimeter range to maximize the regression coefficients for the best fit straight line. The final heights above the average bottom adopted for the lowest three current meters were 17.8, 48.9, and 64.2 centimeters, a zero shift of 2.5 centimeters.

From the data supplied by Cacchione and Drake, 17 profiles with high regression coefficients ($r^2 > 0.99$) were selected for further analysis. Three of the profiles are from data bursts measured approximately 12 hours before the storm (hours 43-47) and 14 profiles are from data bursts measured during the storm (hours 57-83). The estimates of u_* and z_0 calculated from the best fit straight lines to these profiles are listed in Table 6.2 along with the 90 percent confidence intervals and the regression coefficients. Suspended sediment concentrations measured by the transmissometer 2 meters above the bottom also are listed in Table 6.2. Even during the storm peak (hours 65 and 67) when suspended sediment concentrations were largest, the high regression coefficients indicate that the velocity profiles were highly logarithmic. This suggests that suspended sediment induced stratification, which is expected to cause curvature in the velocity profiles, is not significant in the region measured by the GEOPROBE.

Because all 17 velocity profiles appear logarithmic, the data will

Profile Hour	u_* (cm/sec)	z_0 (cm)	R^2	u_{*c} (cm/sec)	z_{0c} (cm)	Cx10^{-5} (2m)	η/A_b	η/λ	u_{50}/u_b	k_b/A_b	z_r/A_b	ϕ_c (deg)	ω (rad)
43	2.95 (+0.77) (-0.50)	1.17 (+1.26) (-0.61)	0.9989	2.63	0.725	0.26			1.96	0.19	1.58	20	0.456
45	2.71 (+0.48) (-0.35)	1.49 (+0.96) (-0.58)	0.9994	2.44	0.988	0.455			1.37	0.18	1.45	0	0.515
47	2.25 (+0.76) (-0.45)	1.83 (+2.19) (-1.00)	0.9984	1.76	0.715	0.325			1.94	0.30	2.41	30	0.474
57	2.57 (+3.65) (-0.95)	3.56 (+11.58) (-2.72)	0.9914	1.91	1.31	0.131			0.99	0.14	1.15	10	0.411
59	1.60 (+0.12) (-0.11)	2.40 (+0.53) (-0.44)	0.9999	1.75	3.15	0.780			0.36	0.069	0.56	30	0.383
61	3.59 (+1.73) (-0.88)	4.33 (+4.75) (-2.27)	0.9974	4.48	7.21	1.81	0.21	0.16	0.79	0.92	0.75	30	0.411
63	5.65 (+1.46) (-0.96)	5.92 (+2.99) (-1.98)	0.9989	4.41	3.38	1.56	0.55	0.065	0.65	0.11	0.39	20	0.360
65	5.41 (+5.05) (-1.76)	4.69 (+8.90) (-3.07)	0.9942	4.64	2.99	3.25	0.50	0.061	0.69	0.092	0.37	30	0.349
67	3.1 (+4.79) (-1.17)	3.24 (+12.08) (-2.55)	0.9908	3.45	4.01	5.19	0.033	0.046	0.36	0.054	0.34	20	0.417
69	4.04 (+1.62) (-0.90)	5.48 (+4.40) (-2.44)	0.9979	3.81	4.61	1.36	0.073	0.079	0.52	0.17	0.46	20	0.408
71	3.48 (+1.54) (-0.82)	6.77 (+5.22) (-2.95)	0.9976	3.87	8.03	1.56	0.15	0.13	0.51	0.52	0.55	0	0.381
73	4.74 (+0.44) (-0.37)	4.42 (+0.94) (-0.77)	0.9998	5.33	5.72	2.01	0.21	0.16	1.16	0.90	0.80	10	0.401
75	3.77 (+4.05) (-1.29)	5.52 (+10.43) (-3.61)	0.9933	3.74	5.13	1.23	0.085	0.087	0.52	0.21	0.49	10	0.411
77	4.88 (+0.46) (-0.39)	5.67 (+1.09) (-0.91)	0.9998	5.08	6.10	2.01	0.19	0.15	0.97	0.78	0.72	10	0.399
79	4.5 (+0.98) (-0.68)	5.85 (+2.50) (-1.75)	0.9992	3.75	3.94	1.23	0.064	0.715	0.53	0.13	0.48	10	0.438
81	4.13 (+0.64) (-0.49)	6.22 (+1.84) (-1.42)	0.9995	4.30	6.84	1.95	0.21	0.16	0.85	0.93	0.79	0	0.405
83	3.29 (+1.99) (-0.90)	3.29 (+5.29) (-2.03)	0.9964	4.57	6.80	1.49	0.21	0.16	0.88	0.92	0.77	10	0.402

TABLE 6.2

CODE WINTER STORM DATA

be compared to the neutral near bottom model initially. As before, input parameters for the neutral model are

$$\frac{|\vec{u}_r|}{|\vec{u}_b|}, \frac{z_r}{A_b}, \bar{\phi}_c, \text{ and } \frac{k_b}{A_b}.$$

Current conditions for the model runs are specified by the current speed $|\vec{u}_r|$ measured by the middle current meter at z_r = 48.9 centimeters. As with the CODE-I data, linear wave theory and the pressure records were used to calculate the wave conditions $|\vec{u}_b|$ and A_b from the average wave period and the maximum pressure difference. Because the burst samples were so short, the relative direction of the current with respect to the wave $\bar{\phi}_c$ could not be determined by the directional spectral analysis technique used for the CODE-I data. Instead, a histogram of the wave direction was made for each crest and trough in the velocity record. The peak in the histogram was taken as the direction of the wave, which was compared to the direction of the current to find $\bar{\phi}_c$. For all 17 logarithmic velocity profiles, the peak in the wave direction histogram was narrow and well defined. The non-logarithmic velocity profiles (hours 49-55) correspond to data bursts with little or no peak in the wave direction histogram, suggesting that other physical processes may be influencing these velocity measurements. The remaining parameter that must be specified to run the neutral near bottom model is the physical bottom roughness k_b.

Before the storm, bottom photographs indicated that the bottom was

covered with animal generated mounds and furrows as at the CODE-I site. Box cores also indicated that the same types of animals were present at each site. The constant physical bottom roughness used in the CODE-I data analysis, z_o = 0.2 centimeters, therefore was used for pre-storm model runs when little sediment transport was observed.

During the storm, the boundary shear stress was sufficient to erode the bioturbated sandy-silt bottom and force large amounts of silt into suspension. Bottom photographs, however, reveal that fine sand was transported mainly as bedload because ripples were observed to form. The physical bottom roughness during the storm therefore will be calculated using the expressions developed by Grant and Madsen (1982) for the roughness associated with ripples and near bed transport.

Additional nondimensional input parameters required to calculate ripple geometry or the height of the near bed transport layer are

$$\frac{d}{A_b}, \; s, \; S_* \quad \text{and} \quad \left[\frac{(s-1)\, gd}{|\vec{u}_b|}\right]^{1/2} .$$

From box cores, the sediment was found to have a bimodal size distribution with a primary peak at about d = 0.003 centimeters (silt) and a secondary peak at about d = 0.01 centimeters (fine sand). Assuming the fine sand dominates the ripples and near bed transport, d is taken as 0.01 centimeters. Assuming the fine sand is quartz, s = 2.65. For the observed bottom temperature of about

$T = 12°C$, the kinematic viscosity of seawater is approximately $\nu = 0.013\ cm^2/sec$ and (3.63) gives $S_* = 0.773$.

Which form is used for the physical bottom roughness in the model runs depends on the relative values of the maximum Shields parameter based on skin friction ψ'_m, and the critical Shields parameter for initiation of motion ψ_c. For $S_* = 0.773$, Shields diagram gives $\psi_c = 0.11$ for an aseptic sediment. Grant et al. (1982) show that a factor of two increase in ψ_c can occur in fine sand due to adhesion induced by benthic organisms. Since the sediment around the GEOPROBE was highly bioturbated, the critical Shields parameter is expected to be in the range $0.11 < \psi_c < 0.22$.

For hours 43-47, the model was run assuming $z_o = 0.2$ centimeters. For these cases, it was found that ψ'_m was well below the assumed range for ψ_c. For hours 63-83, the model was run assuming the bottom roughness was due to ripples and near bed transport. For these cases, it was found that ψ'_m generally was well above the assumed range for ψ_c. Since ripple geometry and the height of the near bed transport layer also depend on ψ_c, the actual value of which is unknown, the model was run for different values of ψ_c within the expected range. Although the model agreed well with the data for all values of ψ_c in this range, the agreement was best for a 20 percent increase in the aseptic value of Shields parameter to $\psi_c = 0.13$. This increase approaches the error bars on ψ_c for laboratory studies of aseptic fine sand as found by Grant et al. (1982).

For hours 59-61, the model was run for both types of bottom roughness. The value of ψ'_m in both cases was in the expected range for ψ_c, but was above the value $\psi_c = 0.13$ assumed for hours 63-83. The predicted values of $|\vec{u}_{*c}|$ and z_{oc} agreed with the profile estimates best when the bottom roughness was based on $z_o = 0.2$ cm for hour 59 and on ripples and near bed transport for hour 61. Because hour 59 agrees better with the pre-storm conditions, the critical Shields parameter for the fine sand may have been as much as twice the aseptic value before the storm. The storm flow conditions, however, were strong enough to mix the sediment and disturb the biologically induced adhesion, probably causing the critical Shields parameter to approach, with time, the aseptic value for the fine sand.

The values of $|\vec{u}_{*c}|$ and z_{oc} predicted by the model are listed in Table 6.2. Predicted ripple geometry is also listed for the storm conditions. For comparison, the model predictions of $|\vec{u}_{*c}|$ and z_{oc} and the profile estimates are plotted in Figure 6.4. Even though the data was sampled for a relatively short time and only three velocity measurements were used to define the profiles, the regression coefficients were high enough that reasonable error bars could be placed on the estimates. Since the model predictions generally are within the 90 percent confidence intervals for both the pre-storm and the design storm conditions, this model comparison is strong evidence for the applicability of the theory to a wide range of conditions on the continental shelf.

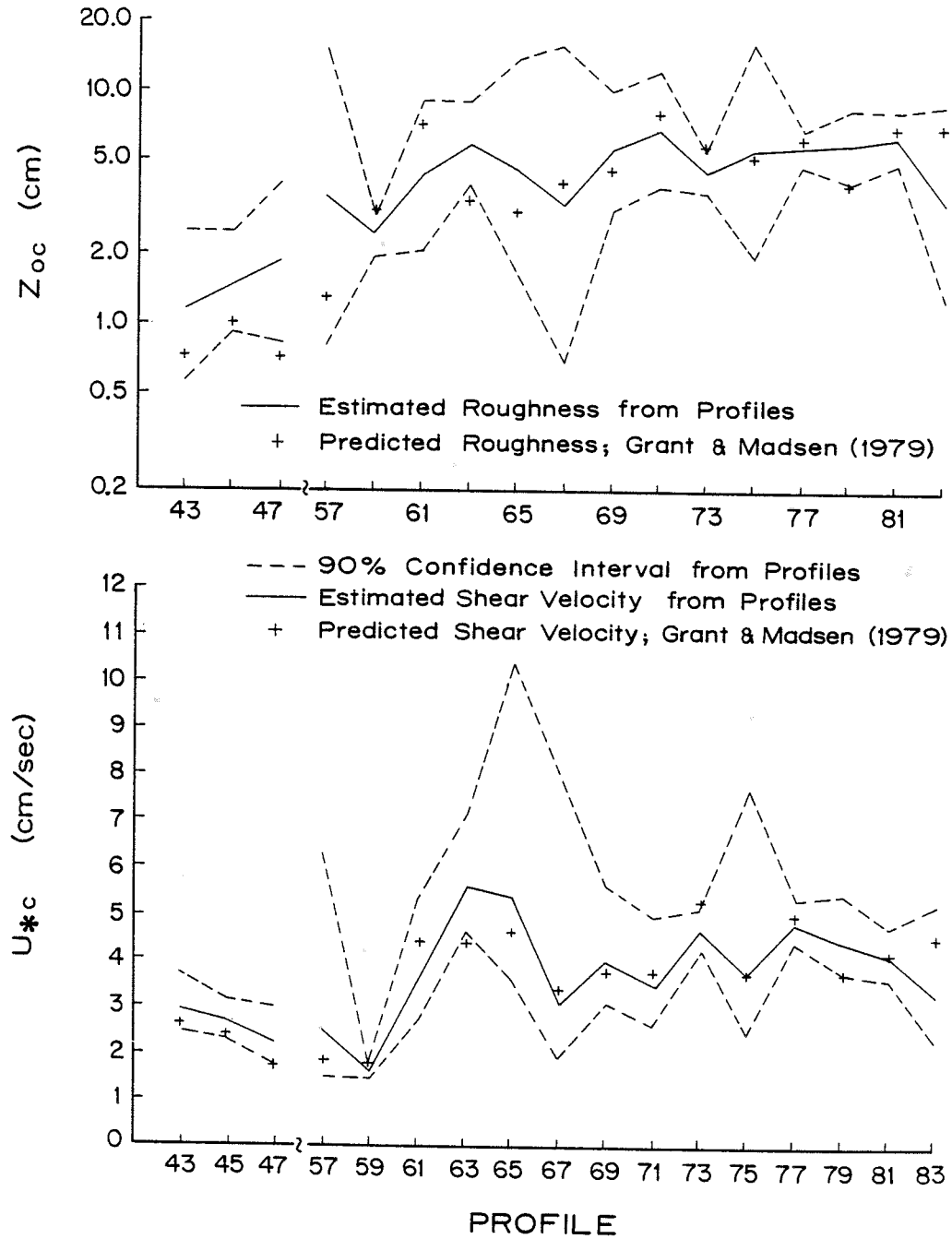

FIGURE 6.4
CODE Winter Storm data/model comparison, shear velocity and bottom roughness estimated from measured velocity profiles and predicted by the neutral near bottom model.

Since sediment concentrations were also measured by a transmissometer 2 meters above the bottom, a model comparison could be attempted for the stratified near bottom model. Initial runs of the stratified model indicate that even for the high flow conditions, the larger fine sand concentrations decrease rapidly above the bottom while the silt is mixed almost uniformly throughout the near bottom flow field. Neither type of sediment is predicted to affect the flow measured by the GEOPROBE because too little fine sand is in suspension and the silt is uniformly mixed.

The stratified model predicts that sediment concentrations measured by the transmissometer are dominated by the silts, which have a fall velocity of order 0.05 cm/sec. Since the silts can be suspended very high in the water column, the sediment concentration profile takes considerable time to adjust to changing conditions as it is advected long distances by the mean current. Because advection of the silt could be an important factor in determining the sediment concentration measured by the transmissometer, local flow conditions may not be the dominant influence. Except for the storm peak (hours 65 and 67), changes in the value of the skin friction, which controls local resuspension and deposition of sediment, are not at all correlated with changes in the measured sediment concentration. Therefore, to try to minimize the effect of advection, only hours 65 and 67 will be compared to the stratified model.

Considering that the importance of advection is unknown and that for mixtures of fine sediments, transmissometer data is not an

accurate measure of sediment concentrations, the sediment will only be divided into two size classes corresponding to the peaks in the size distribution. The sediment is assumed to be 20 percent fine sand (d = 0.01 cm, s = 2.65) and 80 percent silt (d = 0.003 cm, s = 2.65). Assuming a typical porosity of the bed of about 0.4, the bed concentration for the fine sand is 0.12 and for the silt is 0.48. The actual value of the critical Shields parameter, however, is unknown. It therefore is assumed that ψ_c before the storm is twice the aseptic value given by Shields diagram and that sediment does not begin to approach the aseptic ψ_c until it has been eroded from the bed at least once. Since hours 65 and 67 correspond to increasing flow conditions early in the storm when sediment was actively being eroded from the bed for the first time, ψ_c is taken as twice the aseptic value for the model runs.

Since the concentrations were measured at one height only, the stratified model can be used to determine the reference concentration constant by matching the observed concentrations. For these conditions and a value of $\gamma_o = 0.0005$, the concentration predicted by the model for hour 65 is slightly low (3×10^{-5}) and for hour 67 is slightly high (6×10^{-5}). The effect of stratification on $|\vec{u}_{*c}|$ and z_{oc}, however, is predicted to be negligible. Even when the critical Shields parameters are assumed to be 20 percent above the aseptic values and the adopted value for the reference concentration constant $\gamma_o = 0.002$ is used, the predicted value of $|\vec{u}_{*c}|$ is changed by only 5 percent and z_{oc} by only 10 percent.

Though the predicted sediment concentrations are a factor of 10 too high, this is not excessive considering the many assumptions and that the reference concentration neglects the effect of armoring on the bed. At a height of 2 meters, the silt concentration is an order of magnitude greater than the fine sand concentration. Armoring of the bed by the fine sand will reduce the amount of silt available for resuspension, thereby reducing the silt concentration at 2 meters. For either value of γ_0 or ψ_c, the suspended sediment stratification correction is considered to have a negligible effect on the CODE Winter Storm velocity profiles. It therefore is consistent with the stratified model results to assume that the measured velocity profiles are logarithmic and that the profile techniques can be used to estimate u_* and z_0 for comparison with the neutral model.

7. SUMMARY AND CONCLUSIONS

The continental shelf bottom boundary layer model developed here considers the interaction of waves, currents, and a moveable bed in a stratified Ekman layer. A physical description of these processes and how they affect the structure of the bottom boundary layer was presented in Chapter 2. The small scale of the wave boundary layer nested within the Ekman layer results in a large boundary shear stress, increasing the vertical turbulent transport of mass and momentum. Marine organisms and changing flow conditions can significantly modify a moveable sediment bed, changing the physical roughness of the bottom. Stable stratification associated with sediment suspended by the flow or with vertical fluid density gradients can modify the flow by inhibiting vertical turbulent transport. Mathematical models for the bottom boundary layer that included these physical processes were developed in Chapters 3, 4, and 5.

The neutral, near bottom model developed by Grant and Madsen (1979) adopts a quadratic drag law for the boundary shear stress that depends on a combined wave and current friction factor and on the instantaneous wave plus current velocity. The time average shear stress, the gradient of which balances the forces driving the current, therefore is enhanced by the wave. The unsteady momentum equation is solved using a time invariant eddy viscosity that varies linearly with distance from the bottom and depends on the characteristic shear velocity in each boundary layer. The characteristic shear velocity is assumed to depend on the maximum shear stress in the wave boundary layer and the time average shear stress above the wave boundary layer. The increased turbulent

transport in the wave boundary layer causes the current above the wave boundary layer to feel a larger apparent roughness that depends on the wave characteristics as well as the physical bottom roughness. The neutral near bottom model can be used to predict wave and current velocity profiles in the current constant stress layer in the absence of stratification.

The stratified near bottom model is an extension of the neutral model, developed by including the effect of suspended sediment induced stratification in the eddy diffusivity closure scheme. The unsteady conservation of fluid momentum and sediment mass equations, which are coupled through the stability parameter, were solved simultaneously for the wave velocity, current velocity, and sediment concentration profiles in the current constant stress layer. Suspended sediment induced stratification, which does not directly affect the wave for most conditions on the shelf, is found to increase the sediment concentration vertical decay rate and, for a given shear velocity, increase the shear in the current velocity profile. A stratified current therefore requires a lower shear velocity to match a known velocity at a given reference height. As a result, current velocities below the reference height and the skin friction are reduced by stratification. The effects of the stratification correction, which are most pronounced during storm flows when suspended sediment concentrations are largest, are found to be highly dependent on the sediment fall velocity.

To calculate velocity and sediment concentration profiles, the physical bottom roughness and reference concentration must be specified.

The bottom roughness of a moveable bed depends on both the flow and the sediment conditions. When the maximum Shields parameter based on skin friction is below critical and there is little sediment transport, the bottom roughness is usually associated with biologically generated bedforms and is calculated by the method described by Grant and Glenn (in press). When the skin friction is above critical and the bottom roughness is associated with wave generated ripples and near bed transport, the method developed by Grant and Madsen (1982) is used to calculate the bottom roughness. The bottom roughness is found to be dominated by ripples when the skin friction is below the breakoff point and is dominated by near bed transport when the skin friction is well above the breakoff point. The equations for ripple geometry and the height of the near bed transport layer were developed for homogeneous sands and have not yet been generalized to sediment mixtures. The instantaneous sediment reference concentration was assumed to be proportional to the instantaneous normalized excess skin friction when the skin friction is small, but is limited to not exceed the bed concentration. This reference concentration model does not include the effect of armoring, which may be important for some sediment mixtures. The mean reference concentration is then found by averaging the instantaneous reference concentration over a wave period.

The near bottom models were extended to the full Ekman layer by adopting Long's (1981) Ekman layer model. This model includes the effect of Coriolis acceleration in the momentum equations and uses a generalized eddy viscosity and stability parameter that includes temperature and

salinity induced stratification to solve the resulting equations. Coriolis acceleration causes the current velocity vector above the constant stress layer to turn to the right with distance from the bottom in the Northern Hemisphere. The generalized neutral eddy viscosity reduces the Ekman layer height, increases the overshoot in the current velocity profile, and increases the turning angle. The major effect of temperature and salinity stratification is to further reduce the Ekman layer height. The solution for the Ekman layer model and the near bottom models are identical in the current constant stress layer.

The Ekman layer model assumes that as the top of the Ekman layer is approached, the eddy viscosity approaches zero and the current velocity approaches the inviscid geostrophic core velocity. In the depth limited case or during storms, a geostrophic core may not exist because the surface Ekman layer and the bottom Ekman layer overlap. The best method to couple the two Ekman layers and to match the eddy viscosity profiles in the overlap region has not been established.

As shown in the examples discussed in Chapters 4 and 5, the structure of the bottom boundary layer is highly dependent on the wave, current, sediment, and fluid density characteristics. Velocity profiles predicted by the model are compared to the best available continental shelf bottom boundary layer data. The agreement between the model predictions and the data is strong support for the approach used to model the wave-current interaction and the physical bottom roughness. Even though large suspended sediment concentrations where observed during the CODE Winter Storm experiment, the stratified near bottom model predicted that the

sediment fall velocity was too small to effectively stratify the flow field measured by the GEOPROBE. Because the measured velocity profiles are highly logarithmic and show no signs of the curvature characteristic of a stratified flow, the Winter Storm data agrees well with the model predictions. Though this is not considered the best test of the stratification correction, it is the only storm data available at this time.

The near bottom models and the Ekman layer model discussed in Chapters 3, 4, and 5 were developed using an eddy viscosity profile that was linear in the wave boundary layer and discontinuous at the top of the wave boundary layer. A possible improvement in these theoretical models would be the use of a more physically realistic continuous eddy viscosity profile. A continuous profile that is judged to be physically reasonable is used in Appendix II to solve the governing equations. The shear velocity for the current and the apparent bottom roughness predicted using the continuous eddy viscosity profile are still within the error bars on the values estimated from the CODE-I data and the CODE Winter Storm data. Because changes in the physical bottom roughness and the reference concentration within the error bars on these parameters have a greater effect on the predicted shear velocity and apparent bottom roughness than the adoption of a continuous eddy viscosity profile, the simpler linear eddy viscosity was used for the data comparison presented here. Because the suspended sediment induced stratification correction is neglected in the wave boundary layer, there is no theoretical inconsistency preventing the use of the linear eddy viscosity profile in

this region. If the stratification correction could not be neglected in the wave boundary layer, it would be inconsistent to use the simple linear eddy viscosity since the stratification correction must be applied to the proper neutral profile. For this reason, it was necessary to adopt the modulated neutral eddy viscosity in the upper Ekman layer where temperature and salinity induced stratification can be significant.

Though the theoretical model presented here has been compared to the highest quality data available for a wide range of flow conditions, additional comparisons with combined wave and current data are necessary to gain further confidence in the model. Measurements during storms over beds with larger sediment (fine and medium sands) for uniform sediments and for sediment mixtures are required for comparison with the predicted ripple geometry, physical bottom roughness, reference concentrations, and suspended sediment induced stratification correction. Measurements made above the current constant stress layer could be used to establish the validity of the Ekman layer model and help determine how the surface and bottom Ekman layers are coupled. The effects of bioturbation on the bottom sediment, including the initiation of motion criteria and the physical bottom roughness should be studied in greater detail. Laboratory measurements within the oscillatory boundary layer of a combined oscillatory and steady flow could be used to help determine the best form for the eddy viscosity profile within the wave boundary layer. Clearly, the need exists for new high quality laboratory and field data on combined wave and current flows over a moveable bed. The excellent

agreement between the theoretical model developed here and available data is encouraging and hopefully will inspire future field and laboratory experiments to further test and improve this model.

REFERENCES

1. Abbott, M.B. (1979) Computational Hydraulics, Fearon-Pitman, Inc., Belmont, CA, pp. 324.

2. Abou-Seida, M.M. (1965) "Bed Load Function due to Wave Action," U. of Cal., Berkeley, Hydraulic Engineering Lab., Rep. HEL-2-11, 78pp.

3. Abramowitz, M. and I.A. Stegun (1972) Handbook of Mathematical Functions, National Bureau of Standards Applied Math Series, No. 55, pp. 1046.

4. Borgman, L.E. (1976) "Coastal Wave Hydrodynamics, Theory and Engineering Applications," MIT Summer Course.

5. Businger, J.A. and S.P.S. Arya (1974) "Height of the Mixed Layer in the Stably Stratified Planetary Boundary Layer," Advances in Geophysics, Academic Press, New York, pp. 73-92.

6. Businger, J.A., J.C. Wyngaard, Y. Izumi and E.F. Bradley (1971) "Flux-Profile Relationships in the Atmospheric Surface Layer," J. Atm. Sci., 28, pp. 181-189.

7. Cacchione, D.A., D.E. Drake, W.D. Grant, and S.M. Glenn, "Near Bottom Flow Measurements in a Winter Storm on the Northern California Shelf" (in preparation).

8. Carnahan, B., H.A. Luther and J.O. Wilkes, (1969) Applied Numerical Methods, John Wiley and Sons, Inc., New York, pp. 604.

9. Carstens, M.R., R.M. Neilson and H.D. Altinbilek, (1969) "Bed forms generated in the laboratory under oscillatory flow: Analytical and experimental study," Tech. Memo., 28, U.S. Army Corps of Eng., Coastal Eng. Res. Center.

10. Dahlquist, G. and A. Bjorck (1974) Numerical Methods, Prentice-Hall, Inc., Englewood Cliffs, N.J., pp. 573.

11. Deacon, E.L. (1959) "The Measurement of Turbulent Transfer in the Lower Atmosphere," Advances in Geophysics, Vol. 6, Academic Press, pp. 211-228.

12. Ellison, T.H. (1956) "Atmosphere Turbulence," in Batchelor, G.K. and R.M. Davies (eds.), Surveys in Mechanics, Cambridge University Press, pp. 400-30.

13. Grant, W.D. (1977) "Bottom Friction Under Waves in the Presence of a Weak Current: Its Relationship to Coastal Sediment Transport," Sc.D. Thesis, 275 pp., Massachusetts Institute of Technology, Cambridge, MA.

14. Grant, W.D. and O.S. Madsen (1979) "Combined wave and current interaction with a rough bottom," Journal of Geophysical Research, 84, (C4), 1797-1808.

15. Grant, W.D. and O.S. Madsen (1982) "Moveable bed roughness in unsteady oscillatory flow," Journal of Geophysical Research, 87, (C1), 469-481.

16. Grant, W.D., L. Boyer and L.P. Sanford (1982) "The Effect of bioturbation on the initiation of motion of intertidal sands," J. of Marine Research, 40 (3), pp. 659-677.

17. Grant, W.D. and S.M. Glenn (in press) "Continental Shelf Bottom Boundary Layer Model, Vol. II: Model/Data Comparison," WHOI Technical Report, pp. 62.

REFERENCES (cont.)

18. Grant, W.D., O.S. Madsen, and T.A. Stefanick "Prediction of bed forms in oscillatory flows," (in prep).

19. Hildebrand, F. (1965) Calculus for Applications, Prentice-Hall, Inc., Englewood Cliffs, N.J., pp. 646.

20. Hinze, J.O. (1959) Turbulence, McGraw-Hill, New York, 586 pp.

21. Hunt, J.N. (1954) "The turbulent transport of suspended sediment in open channels," Proc. Roy. Soc. London A 224, pp. 322-335.

22. Hunt, J.N. (1969) "On the turbulent transport of a heterogeneous sediment," Quart. Jour. Mech. and Applied Math., 22, (2), pp. 235-246.

23. Inman, D.L. (1957) "Wave generated ripples in nearshore sands, Tech. Memo 100, p. 41, U.S. Army Corps of Eng., Beach Erosion Board.

24. Jackson, P.S. (1981) "On the displacement height in the logarithmic velocity profile," J. Fluid Mech., 111, 15-25.

25. Kalkanis, G. (1964) "Transportation of Bed Material due to Wave Action," U.S. Army Corps of Engineers, CERC, Tech. Memo No 2, 38 pp.

26. Kennedy, J.F. and F.A. Locher (1972) "Sediment Suspension by Water Waves," In: Meyer, R.E., Ed., Waves on Beaches and Resulting Sediment Transport, Academic Press, New York, 462 pp.

27. Long, C.E. (1981) "A simple model for time-dependent stably stratified turbulent boundary layers," Special Report No. 95, Dept. of Oceanography, University of Washington, Seattle, WA, 170 pp.

REFERENCES (cont.)

28. Lumley, J.L. (1978) "Two-phase and non-Newtonian flows, Topics in Applied Physics, 12, Ed. by P. Bradshaw, pp. 289-324, Springer, New York.

29. Madsen, O.S. and W.D. Grant (1976) "Sediment transport in the coastal environment," Ralph M. Parson Laboratory, MIT Report No. 209. 105 pp.

30. Nowell, A.R.M., P.A. Jumars and R.F.L. Self (1981) "A Markov model of flow sediment-organism interactions: fluid mechanical and biological processes affecting the transition probabilities, in Proceedings International Geol. Cong. Conf., Nittrouer, Paris, France.

31. Owen, P.R. (1964) "Saltation of uniform grains in air," J. Fluid Mech., 20, (2), pp. 225.

32. Rhoads, D.C., J.Y. Yingst and W. Ullman (1978) "Seafloor stability in central Long Island Sound: Pt. 1: Temporal changes in erodibility of fine-grained sediment, in Estuarine Interactions, M.L. Wiley, ed., Academic Press, pp. 221-244.

33. Smith, J.D. (1977) "Modeling of sediment transport on continental shelves," in The Sea, 6, Wiley - Interscience, New York.

34. Smith, J.D. and S.R. McLean (1977) "Spatially averaged flow over a wavy surface," J. Geophys. Res., 82 (12), pp. 1735-1746.

35. Smith, J.D. and S.R. McLean (1977) "Boundary layer adjustments to bottom topography and suspended sediment," Bottom Turbulence, ed. by J. Nihoul, pp. 123-151, Elsevier, New York.

REFERENCES (cont.)

36. Soo, S.L. (1967) Fluid Dynamics of Multiphase Systems, Blaisdell Publishing Co., Waltham, MA.

37. Taylor, P.A. and K.R. Dyer (1978) "Theoretical models of flow near the bed and their implications for sediment transport," The Sea, 6, ed. by E.D. Goldberg et al., pp. 579-601, Wiley - Interscience, New York.

38. Townsend, A.A. (1970) "Entrainment and the structure of turbulent flow," J. Fluid Mech., 41, 13-46.

39. Williams, A.J. and R. Koehler, "An acoustic travel time current meter for ocean boundary layer measurements," (in prep.).

40. Wooding, R.A., E.F. Bradley and J.K. Marshall (1973) "Drag due to regular arrays of roughness elements of varying geometry," Boundary Layer Meteorology, 5, 285-308.

APPENDIX I: Numerical Methods

This appendix describes the numerical methods used in the bottom boundary layer models. The secant method described in Section 1 is used to improve the convergence of the iterative procedure adopted for solving the model equations. The implicit difference method described in Section 2 is used to solve the Ekman layer model equations because it is unconditionally stable and does not depend on step size.

A.I.1 Secant Newton-Raphson Method

An iterative solution technique was adopted in Sections 3.1.5, 4.1.8 and 5.1.8 to calculate near bottom and Ekman layer velocity profiles. The near bottom model solution procedure involves guessing a value of u_a/u_b, using the model to calculate u_r/u_b, and comparing the calculated result with the given value of u_r/u_b. The Ekman layer solution procedure requires guessing both u_a/u_b and $\bar{\phi}_c$, calculating u_r/u_b and ϕ_r from the model, and comparing the calculated results with the given values of u_r/u_b and ϕ_r. Vector notation has been dropped for convenience. The secant method, which is just the discrete version of the Newton-Raphson method, was found to be a very efficient procedure for finding the proper values of u_a/u_b and $\bar{\phi}_c$.

The Newton-Raphson method can be used to find the solution of the equation $f(x) = 0$. Given an initial guess for the solution x_n, the next guess calculated by the Newton-Raphson method is

$$x_{n+1} = x_n - \frac{f(x_n)}{\frac{\partial f}{\partial x}(x_n)} \tag{I.1}$$

The secant method is the same as the Newton-Raphson method except that a discrete approximation is made for the derivative in (I.1). The equation for the next guess by the secant method can be written

$$x_{n+1} = x_n - f(x_n) \frac{x_n - x_{n-1}}{f(x_n) - f(x_{n-1})} \tag{I.2}$$

Though the secant method requires two initial guesses to find x_{n+1}, it has the advantage that the derivative does not have to be evaluated explicitly. For the near bottom model, the function to be evaluated is

$$f\left(\frac{u_a}{u_b}\right) = \frac{u_r}{u_b} - \left(\frac{u_r}{u_b}\right)_G = 0 \tag{I.3}$$

where $(u_r/u_b)_G$ is the given value, and u_r/u_b is the value calculated by the model from u_a/u_b. Given two initial guesses for u_a/u_b and the resulting values of u_r/u_b, the next guess by the secant method is

$$\left(\frac{u_a}{u_b}\right)_{n+1} = \left(\frac{u_a}{u_b}\right)_n - \left[\left(\frac{u_r}{u_b}\right)_n - \left(\frac{u_r}{u_b}\right)_G\right] \frac{\left[\left(\frac{u_a}{u_b}\right)_n - \left(\frac{u_a}{u_b}\right)_{n-1}\right]}{\left[\left(\frac{u_r}{u_b}\right)_n - \left(\frac{u_r}{u_b}\right)_{n-1}\right]} \tag{I.4}$$

The Newton-Raphson method can also be generalized to find the solution to the simultaneous equations $f(x,y) = 0$ and $g(x,y) = 0$.

Given an initial guess (x_n, y_n) for the solution, the next guess calculated by the Newton-Raphson method is

$$x_{n+1} = x_n - \frac{A\,(x_n, y_n)}{J\,(x_n, y_n)} \tag{I.5}$$

and

$$y_{n+1} = y_n - \frac{B\,(x_n, y_n)}{J\,(x_n, y_n)} \tag{I.6}$$

where

$$A\,(x_n, y_n) = \left(f \frac{\partial g}{\partial x} - g \frac{\partial f}{\partial y}\right) \Big|_{x_n, y_n} \tag{I.7}$$

$$B\,(x_n, y_n) = \left(g \frac{\partial f}{\partial x} - f \frac{\partial g}{\partial y}\right) \Big|_{x_n, y_n} \tag{I.8}$$

$$J\,(x_n, y_n) = \left(\frac{\partial f}{\partial x} \frac{\partial g}{\partial y} - \frac{\partial f}{\partial y} \frac{\partial g}{\partial x}\right) \Big|_{x_n, y_n} \tag{I.9}$$

The secant method uses the following discrete approximations to the derivatives in (I.7), (I.8), and (I.9)

$$\frac{\partial f}{\partial x}\,(x_n, y_n) = \frac{f\,(x_n, y_n) - f\,(x_{n-1}, y_n)}{x_n - x_{n-1}} \tag{I.10}$$

$$\frac{\partial f}{\partial y}\,(x_n, y_n) = \frac{f\,(x_n, y_n) - f\,(x_n, y_{n-1})}{y_n - y_{n-1}} \tag{I.11}$$

$$\frac{\partial g}{\partial x}\,(x_n, y_n) = \frac{g\,(x_n, y_n) - g\,(x_{n-1}, y_n)}{x_n - x_{n-1}} \tag{I.12}$$

$$\frac{\partial g}{\partial y}(x_n, y_n) = \frac{g(x_n, y_n) - g(x_n, y_{n-1})}{y_n - y_{n-1}} \tag{I.13}$$

The functions to be solved for the Ekman layer model are

$$f\left(\frac{u_a}{u_b}, \bar{\phi}_c\right) = \frac{u_r}{u_b} - \left(\frac{u_r}{u_b}\right)_G = 0 \tag{I.14}$$

and

$$g\left(\frac{u_a}{u_b}, \bar{\phi}_c\right) = \phi_r - (\phi_r)_G = 0 \tag{I.15}$$

where $(u_r/u_b)_G$ and $(\phi_r)_G$ are the given values, and u_r/u_b and ϕ_r are calculated by the model from u_a/u_b and $\bar{\phi}_c$. Given two initial guesses for u_a/u_b and $\bar{\phi}_c$, the next guess for the solution to (I.14) and (I.15) by the secant method is

$$\left(\frac{u_a}{u_b}\right)_{n+1} = \left(\frac{u_a}{u_b}\right)_n - \frac{A_n}{J_n} \tag{I.16}$$

and

$$(\phi_r)_{n+1} = (\phi_r)_n - \frac{B_n}{J_n} \tag{I.17}$$

where

$$A_n = \left[\left(\frac{u_a}{u_b}\right)_n - \left(\frac{u_a}{u_b}\right)_{n-1}\right] \cdot \tag{I.18}$$

$$\cdot \left\{\left[\left(\frac{u_r}{u_b}\right)_{n,n} - \left(\frac{u_r}{u_b}\right)_G\right] \left[(\phi_r)_{n,n} - (\phi_r)_{n,\,n-1}\right]\right.$$

$$- [(\phi_r)_{n,n} - (\phi_r)_G] \left[\left(\frac{u_r}{u_b}\right)_{n,n} - \left(\frac{u_r}{u_b}\right)_{n,n-1}\right] \}$$

$$B_n = [(\bar{\phi}_c)_n - (\bar{\phi}_c)_{n-1}] \cdot \tag{I.19}$$

$$\cdot \{[(\phi_r)_{n,n} - (\phi_r)_G] \left[\left(\frac{u_r}{u_b}\right)_{n,n} - \left(\frac{u_r}{u_b}\right)_{n-1,n}\right]$$

$$- \left[\left(\frac{u_r}{u_b}\right)_{n,n} - \left(\frac{u_r}{u_b}\right)_G\right] [(\phi_r)_{n,n} - [(\phi_r)_{n-1,\,n}] \}$$

and $J_n =$

$$= \{\left[\left(\frac{u_r}{u_b}\right)_{n,n} - \left(\frac{u_r}{u_b}\right)_{n-1,\,n}\right] [(\phi_r)_{n,n} - (\phi_r)_{n,\,n-1}]$$

$$- \left[\left(\frac{u_r}{u_b}\right)_{n,n} - \left(\frac{u_r}{u_b}\right)_{n,\,n-1}\right] [(\phi_r)_{n,n} - (\phi_r)_{n-1,\,n}] \} \tag{I.20}$$

The calculated values for u_r/u_b and ϕ_r in (I.18), (I.19), and (I.20) have two subscripts; the first subscript denotes the value of u_a/u_b and the second subscript denotes the value of $\bar{\phi}_c$ used by the Ekman layer model to find u_r/u_b and ϕ_r. To use equations (I.16) through (I.20), the Ekman layer model must be run three times; for $(u_a/u_b)_n$ and $(\bar{\phi}_c)_n$, for $(u_a/u_b)_n$ and $(\bar{\phi}_c)_{n-1}$, and for $(u_a/u_b)_{n-1}$ and $(\bar{\phi}_c)_n$.

A.I.2 Implicit Difference Method

This section describes the double sweep implicit difference method used to solve numerically the boundary value problem

$$\frac{\partial^2 w}{\partial \chi^2} + \frac{1}{F(\chi)} \frac{\partial F}{\partial \chi} \frac{\partial w}{\partial \chi} - i \xi_w \frac{e^{\chi}}{F(\chi)} w = 0 \quad \text{for } 0 \leq \chi \leq \chi_c \tag{I.21}$$

$$\frac{\partial w}{\partial \chi} = \frac{1}{F(\chi)} \frac{|\vec{u}_{*c}|}{\kappa} \qquad \text{at } \chi = 0 \tag{I.22}$$

$$w = 0 \qquad \text{at } \chi = \chi_c \tag{I.23}$$

described in Section 5.1.7. Defining the step size $\Delta = \chi_c/N$ where N is the number of steps, the boundary value problem can be written in discrete form as

$$\frac{w_{n+1} - 2w_n + w_{n-1}}{\Delta^2} + A_n \frac{w_{n+1} - w_{n-1}}{2\Delta} - i B_n w_n = 0 \quad \text{for } 0 \leq n \leq N \tag{I.24}$$

$$\frac{w_2 - w_{-1}}{2\Delta} = \frac{1}{F(\chi_0)} \frac{|\vec{u}_{*c}|}{\kappa} \qquad \text{at } n = 0 \tag{I.25}$$

$$w_N = 0 \qquad \text{at } n = N \tag{I.26}$$

where

$$A_n = \frac{1}{F(\chi_n)} \left(\frac{\partial F}{\partial \chi}\right)_n , \quad B_n = \xi_w \frac{e^{\chi_n}}{F(\chi_n)} \tag{I.27}$$

and

$$\chi_n = n\,\Delta \quad . \tag{I.28}$$

The governing equation (I.24) can be rewritten in the form

$$(1 + \tfrac{\Delta}{2} A_n)\, w_{n+1} - (2 + i\,\Delta^2 B_n)\, w_n + (1 - \tfrac{\Delta}{2} A_n)\, w_{n-1} = 0 \tag{I.29}$$

By combining the boundary condition at (I.25) with (I.29) applied at $n = 0$, w_{-1} can be eliminated to give the following boundary condition at n=0

$$2\, w_1 - (2 + i\,\Delta^2 B_o)\; w_o = (1 - \tfrac{\Delta}{2} A_o)\, \frac{2\,\Delta}{F(\chi_o)}\, \frac{|\vec{u}_{*c}|}{\kappa} \tag{I.30}$$

The governing equation (I.29) again can be rewritten as

$$w_{n+1} + C_n\, w_n + D_n\, w_{n-1} = 0 \tag{I.31}$$

where

$$C_n = \frac{(1 - \frac{\Delta}{2} A_n)}{(1 + \frac{\Delta}{2} A_n)} \qquad \text{and} \qquad D_n = \frac{(2 + i\,\Delta^2 B_n)}{(1 + \frac{\Delta}{2} A_n)} \tag{I.32}$$

It then is assumed that a new variable E can be defined such that

$$w_{n+1} = E_n\, w_n \tag{I.33}$$

or

$$w_n = E_{n-1}\, w_{n-1} \tag{I.34}$$

Substituting (I.33) for w_{n+1} in (I.31) gives

$$w_n = \frac{-D_n}{E_n + C_n} \; w_{n-1} \tag{I.35}$$

By comparison with the second definition of E in (I.34), it is seen that E_{n-1} and E_n are related by the equation

$$E_{n-1} = \frac{-D_n}{E_n + C_n} \tag{I.36}$$

The w_1 term can be eliminated from the boundary condition (I.30) by using the equation $w_1 = E_o w_o$. Solving for w_o gives the condition that

$$w_o = \frac{(1 - \frac{\Delta}{2} A_o) \; \frac{2\Delta}{F(x_o)} \frac{|\vec{u}_{*c}|}{\kappa}}{2 E_o - (2 \quad + i \, \Delta^2 B_o)} \tag{I.37}$$

The boundary condition at n = N requires

$$w_N = 0 = E_{N-1} \, w_{N-1} \tag{I.38}$$

Since it is assumed that $w_{N-1} \neq 0$, it follows that $E_{N-1} = 0$. Since D_n and C_n are known for all n, $E_{N-1} = 0$ and (I.36) can be used to find all values of E_n from E_{N-2} to E_o on the first sweep. The value of E_o can be used to calculate w_o from (I.37). Finally, w_o, the known values of E_n, and (I.33) are used to calculate all values of w_n from w_1 to w_N on the second sweep.

APPENDIX II: Continuous Eddy Viscosity Profile

The eddy viscosity profile used in the theoretical models developed in Chapters 3, 4, and 5 is discontinuous at the top of the wave boundary layer. In this section, a more physically realistic continuous eddy viscosity profile is proposed. Since the continuous eddy viscosity profile directly influences the wave boundary layer only, the governing equations are solved just for the near bottom flow.

A.II.1 Turbulent closure scheme

Both the near bottom model and the Ekman layer model assume the neutral eddy viscosity is a linear function of z in both the wave boundary layer and the constant stress region of the current boundary layer

$$\nu_{tcw} = \kappa \, |\vec{u}_{*cw}| \, z \qquad z < 2\, l_{cw} \tag{II.1}$$

$$\nu_{tc} = \kappa \, |\vec{u}_{*c}| \, z \qquad 2\, l_{cw} < z \lesssim 0.1\, l_c \tag{II.2}$$

where l_{cw} and l_c are the scale heights of the wave boundary layer and the current boundary layer defined as

$$l_{cw} = \frac{\kappa \, |\vec{u}_{*cw}|}{\omega} \tag{II.3}$$

$$l_c = \frac{\kappa \, |\vec{u}_{*c}|}{f} \tag{II.4}$$

This eddy viscosity profile is discontinuous at the top of the wave boundary layer, assumed to be located at $z = 2\, l_{cw}$. It can be argued that a linear eddy viscosity should apply only to the constant stress region of the wave boundary layer and that (II.1) actually overestimates the eddy viscosity in the upper wave boundary layer. Just as (II.2) was modified to apply to the full Ekman layer, (II.1) should be modified to apply to the full wave boundary layer. Similar to the Ekman layer eddy viscosity given by (5.12), the eddy viscosity in the wave boundary layer can be taken as a linear function of z modulated by an exponential decay factor

$$\nu_{tcw} = \kappa\, |\vec{u}_{*cw}|\, z\, e^{-2.4\, z/l_{cw}} \qquad \text{(II.5)}$$

The eddy viscosity defined by (II.5) is approximately linear for small z/l_{cw}, reaches a maximum value

$$\nu_{tcw} = \kappa\, |\vec{u}_{*cw}|\, \frac{l_{cw}}{2.4}\, e \qquad \text{(II.6)}$$

at $z = l_{cw}/2.4$, and decays exponentially for large z/l_{cw}. This form for the eddy viscosity was applied to a pure wave boundary layer by Long (1981) and was found to improve agreement with pure wave data for the wave phase and the velocity overshoot in the upper boundary layer. Equation (II.5) is plotted in Figure (A.1) for comparison with the linear eddy viscosity given by (II.1).

Since the eddy viscosity profiles defined by (II.5) and (II.2) cross at

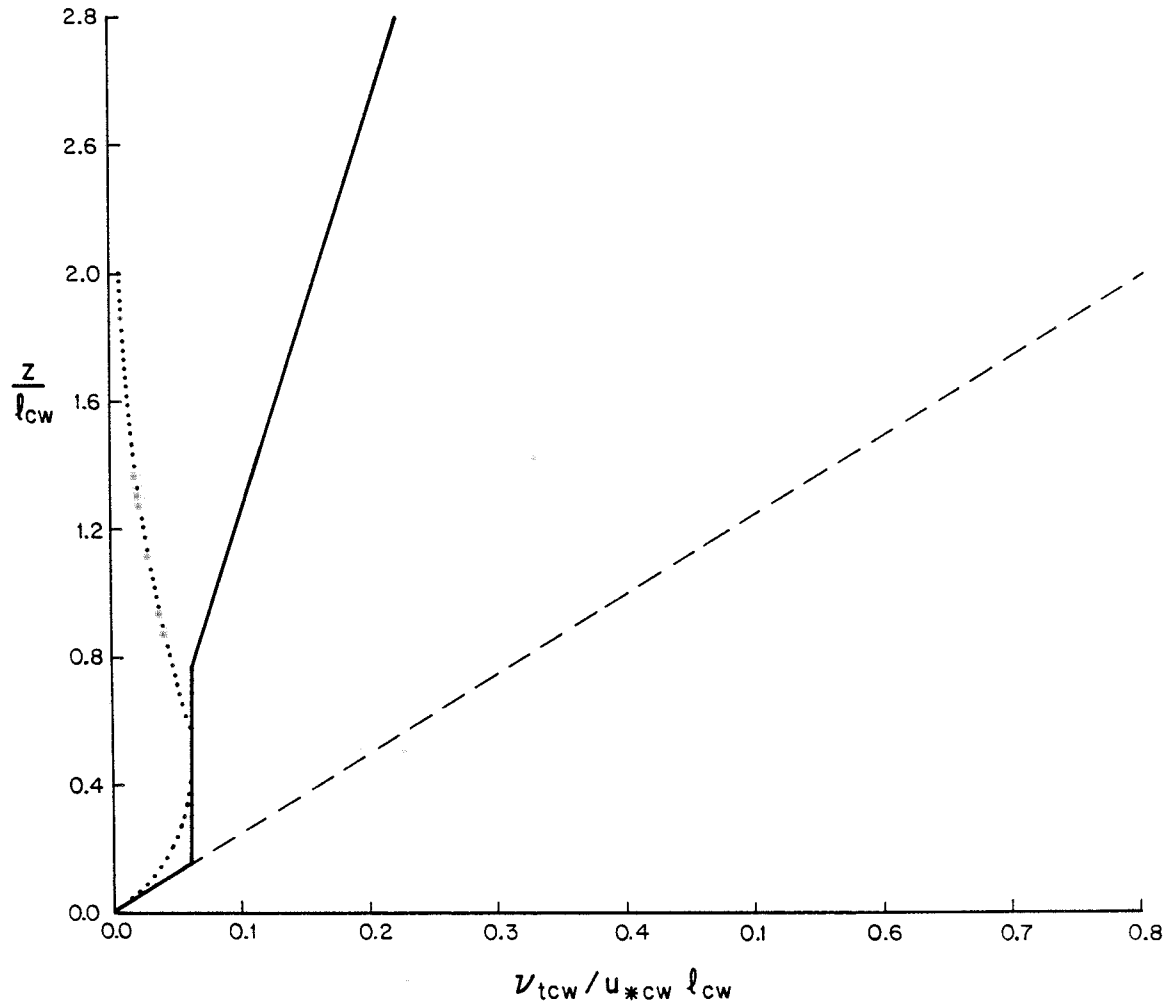

FIGURE A.1

Dimensionless eddy viscosity $\nu_{tcw}/u_{*cw}\, l_{cw}$ in the wave boundary layer as a function of z/l_c; linear eddy viscosity (dashed line) given by II.1 and modulated eddy viscosity (dotted line) given by II.5 compared to continuous eddy viscosity profile (solid line) given by (II.9), (II.10) and (II.11) for $|\vec{u}_{*c}| \,/\, |\vec{u}_{*cw}| = 1/5$.

$$z = z_c = \frac{l_{cw}}{2.4} \ln \frac{|\vec{u}_{*cw}|}{|\vec{u}_{*c}|} \tag{II.7}$$

a possible form for a continuous profile could be defined using (II.5) for $z < z_c$ and (II.2) for $z > z_c$. This implies that the characteristics of the largest momentum transporting turbulent eddies are dominated by the enhanced wave for $z < z_c$ and by the enhanced current for $z > z_c$. Unless

$$\frac{|\vec{u}_{*c}|}{|\vec{u}_{*cw}|} < e^{-4.8} \sim .0082 \tag{II.8}$$

which corresponds to an extremely weak current, $z_c < 2\, l_{cw}$ and the matching height is within the wave boundary layer.

The solution in the wave boundary layer, however, is no longer analytic when the eddy viscosity is defined by (II.5). To avoid going to a numerical solution in the wave boundary layer, the eddy viscosity can be approximated as a linear function of z up to a height z_1 and as a constant above z_1.

$$\nu_t = \kappa |\vec{u}_{*cw}| z \qquad z < z_1 \tag{II.9}$$

$$\nu_t = \kappa |\vec{u}_{*cw}| z_1 \qquad z_1 < z < z_2 \tag{II.10}$$

$$\nu_t = \kappa |\vec{u}_{*c}| z \qquad z_2 < z \leq 0.1\, l_c \tag{II.11}$$

For this eddy viscosity profile to be continuous, the value of the matching height z_2 can be found by evaluating (II.11) at z_2 and matching the result to (II.10). Solving for z_2 gives

$$z_2 = \frac{|\vec{u}_{*cw}|}{|\vec{u}_{*c}|} \, z_1 \tag{II.12}$$

The problem now is to choose appropriate values for the matching heights z_1 and z_2.

One possibility is to choose z_1 such that the constant eddy viscosity given by (II.10) equals the maximum of the eddy viscosity given by (II.5). Equating (II.6) to (II.10) gives

$$z_1 = l_{cw}/2.4\ e \tag{II.13}$$

From (II.12), the matching height z_2 is

$$z_2 = \frac{|\vec{u}_{*cw}|}{|\vec{u}_{*c}|} \, \frac{l_{cw}}{2.4\ e} \tag{II.14}$$

which is in the wave boundary layer if

$$\frac{|\vec{u}_{*c}|}{|\vec{u}_{*cw}|} > \frac{1}{4.8\ e} \sim 0.077 \tag{II.15}$$

For very weak currents, (II.15) is not satisfied and $z_2 > 2\ l_{cw}$. To avoid overestimating the eddy viscosity above the wave boundary layer for the weak current case, it is proposed that the constant

eddy viscosity only extend to the top of the wave boundary layer, that is

$$z_2 = 2\, l_{cw} \qquad \text{for} \qquad \frac{|\vec{u}_{*c}|}{|\vec{u}_{*cw}|} < \frac{1}{4.8\, e} \tag{II.16}$$

The proposed neutral eddy viscosity profile therefore is given by (II.9), (II.10), and (II.11) with z_1 given by (II.13). When (II.15) is satisfied, z_2 is given by (II.14) and the eddy viscosity profile is continuous. For the weak current case, z_2 is given by (II.16) and the eddy viscosity profile remains discontinuous. The proposed eddy viscosity profile is plotted in Figure A-1 for $|\vec{u}_{*c}|/|\vec{u}_{*cw}| = 1/5$. As the current gets weaker and the value of $|\vec{u}_{*c}|/|\vec{u}_{*cw}|$ decreases, the difference between the linear and the modified eddy viscosity profiles increases. Because (II.15) is usually satisfied for most cases of interest on the continental shelf, the weak current solution will not be discussed here.

In Section 4.1.4 it was noted that the stability parameter in the wave boundary layer given by (4.37) was of order 10^{-2} or less. For this stability parameter to affect the flow, it would have to be more than an order of magnitude larger. Equation (4.37), however, is the constant stress layer form for the stability parameter, which also should be generalized to apply to the full wave boundary layer. One possibility is to apply the generalized stability parameter proposed by Long (1982) to suspended sediment induced stratification in the wave boundary layer

$$\zeta_{cw} = \frac{\nu_t}{|\vec{u}_{*cw}|^2 \; |\overline{-\vec{u}'w'}|} \sum_n g\,(s_n - 1)\,\overline{c'_n w'} \tag{II.17}$$

for $z < z_2$ and use (4.47) for $z > z_2$. Because the eddy viscosity is small near the bed, the stability parameter given by (II.17) is expected to be largest when z_2 is near the top of the wave boundary layer. The turbulent fluxes at the top of the wave boundary layer are dominated by the derivatives of the mean variables

$$|-\overline{\vec{u}'w'}| \sim \nu_{tm} \left|\frac{\partial \vec{u}_c}{\partial z}\right| = |\vec{u}_{*c}|^2 \tag{II.18}$$

$$-\overline{c'_n w'} \sim \nu_{ts} \frac{\partial C_{nm}}{\partial z} \tag{II.19}$$

and the neutral eddy viscosity at the top of the wave boundary layer from (II.11) is

$$\nu_t = \kappa \, |\vec{u}_{*c}| \; 2\, l_{cw} \tag{II.20}$$

The maximum stability parameter from (II.17) when z_2 is near the top of the wave boundary layer becomes

$$(\zeta_{cw})_{max} = \frac{\kappa \, |\vec{u}_{*c}| \; 2\, l_{cw}}{|\vec{u}_{*cw}|^2 \; |\vec{u}_{*c}|^2} \sum_n g\,(s_n - 1)\,\left(-\nu_{ts} \frac{\partial C_{nm}}{\partial z}\right) \tag{II.21}$$

Comparing (II.21) with (4.53), the initial factor associated with turbulent kinetic energy production in the stability parameter has been increased by the amount $|\vec{u}_{*cw}| / |\vec{u}_{*c}|$. For the problem considered here, it is assumed that $|\vec{u}_{*cw}| / |\vec{u}_{*c}| <$ (4.8 e) and the production term is only increased by a factor of about 13 in the worst case. Since the sediment flux given by (II.19) is also decreased by the reduced eddy viscosity, the stability parameter is still expected to be small for $z < z_2$. It therefore is assumed that the stability parameter for $z > z_2$ is given by (4.47) and the stability parameter for $z < z_2$ is zero.

A.II.2 Solution for the mean concentration

The equation to be solved for the mean concentration profile in the wave boundary layer is

$$\nu_{ts} \frac{\partial C_{mn}}{\partial z} + w_{fn} C_{mn} = 0 \qquad \text{(II.22)}$$

The solution for the mean concentration using the eddy viscosity profile defined by (II.9), (II.10), and (II.11) is

$$C_{nm}(z) = C_{nm}(z_o) \left(\frac{z}{z_o}\right)^{-\frac{\gamma w_{fn}}{\kappa |u_{*cw}|}} \qquad z_o < z < z_1 \qquad \text{(II.23)}$$

$$C_{nm}(z) = C_{nm}(z_1)\, e^{\left(-\frac{\gamma w_{fn}}{\kappa |u_{*cw}|} \frac{z}{z_1}\right)} \qquad z_1 < z < z_2 \qquad \text{(II.24)}$$

$$C_{nm}(z) = C_{nm}(\delta_w)\left(\frac{z}{\delta_w}\right)^{-\frac{\gamma w_{fn}}{\kappa |u_{*c}|}} \exp\left(-\frac{\beta w_{fn}}{\kappa |u_{*c}|}\int_{z_2}^{z}\frac{dz}{L_c}\right) \quad z_1 < z \tag{II.25}$$

where z_1 and z_2 are defined by (II.13) and (II.14). Using (II.23), (II.24), and (II.25), the solution for the mean concentration at the top of the wave boundary layer can be written

$$C_{nm}(\delta_w) =$$

$$= C_{nm}(z_o)\left(\frac{z_1}{z_o}\right)^{-\frac{\gamma w_{fn}}{\kappa |u_{*cw}|}} e^{\left(-\frac{\gamma w_{fn}}{\kappa |u_{*cw}|}\frac{z_2}{z_1}\right)} \left(\frac{\delta_w}{z_2}\right)^{-\frac{\gamma w_{fn}}{\kappa |u_{*c}|}} \cdot$$

$$\cdot \exp\left(-\frac{\beta w_{fn}}{\kappa |u_{*c}|}\int_{z_2}^{\delta_w}\frac{dz}{L_c}\right) \tag{II.26}$$

The solution for $C_{mn}(\delta_w)$ derived using the linear eddy viscosity profile can be written from (4.57) as

$$C_{nm}(\delta_w) = \tag{II.27}$$

$$= C_{nm}(z_o)\left(\frac{z_1}{z_o}\right)^{-\frac{\gamma w_{fn}}{\kappa |u_{*cw}|}} \left(\frac{z_2}{z_1}\right)^{-\frac{\gamma w_{fn}}{\kappa |u_{*cw}|}} \left(\frac{\delta_w}{z_2}\right)^{-\frac{\gamma w_{fn}}{\kappa |u_{*cw}|}}$$

From z_1 to z_2 the exponential decay rate in (II.26) is faster

than the decay rate in (II.27). Since $|\vec{u}_{*c}| < |\vec{u}_{*cw}|$ and because of the stratification correction, the decay rate from z_2 to δ_w also is faster in (II.26). The continuous eddy viscosity profile therefore reduces the sediment concentration at the top of the wave boundary layer. As a result, less sediment is available above the wave boundary layer to stratify the near bottom flow field.

A.II.3 Solution for the current

The governing equation for the current in the wave boundary layer is

$$\nu_{tm} \frac{\partial \vec{u}_c}{\partial z} = |\vec{u}_{*c}| \vec{u}_{*c} \tag{II.28}$$

Using the eddy viscosity given by (II.9), integrating (II.28), and applying the no slip boundary condition at z_o gives

$$\vec{u}_c(z) = \frac{\vec{u}_{*c}}{\kappa} \frac{|\vec{u}_{*c}|}{|\vec{u}_{*cw}|} \ln \frac{z}{z_o} \qquad z_o < z < z_1 \tag{II.29}$$

Using (II.10) and integrating (II.28) gives

$$\vec{u}_c(z) - \vec{u}_c(z_1) = \frac{\vec{u}_{*c}}{\kappa} \frac{|\vec{u}_{*c}|}{|\vec{u}_{*cw}|} \left(\frac{z - z_1}{z_1}\right) \qquad z_1 < z < z_2 \tag{II.30}$$

Evaluating (II.29) at z_1 and substituting for $u_c(z_1)$ in (II.30) gives

$$\vec{u}_c(z) = \frac{\vec{u}_{*c}}{\kappa} \frac{|\vec{u}_{*c}|}{|\vec{u}_{*cw}|} \left(\ln \frac{z_1}{z_o} + \frac{z}{z_1} - 1\right) \qquad z_1 < z < z_2 \tag{II.31}$$

Using (II.11) and (4.47), integrating (II.28), and applying the apparent no slip condition at z_{oc} gives

$$\vec{u}_c = \frac{\vec{u}_{*c}}{\kappa} \left(\ln \frac{z}{z_{oc}} + \beta \int_{z_2}^{z} \frac{dz}{L_c}\right) \qquad z_2 < z \tag{II.32}$$

The current profile in the wave boundary layer therefore is logarithmic near the bottom, linear in the middle, and similar to (4.77) near the top.

Matching (II.31) and (II.32) at $z = z_2$ gives the equation for the apparent roughness as

$$\frac{z_{oc}}{z_o} = \frac{z_2}{z_o}\left[\frac{z_1}{z_o} \exp\left(\frac{z_2}{z_1} - 1\right)\right] \tag{II.33}$$

$$- |\vec{u}_{*c}|/|\vec{u}_{*cw}|$$

This definition of z_{oc}, and therefore the current velocity profile, is independent of the definition of the wave boundary layer height. From (II.12) and the definitions of $|\vec{u}_{*cw}|$ and $|\vec{u}_{*c}|$, it follows that $z_2/z_1 > 1$ and $\exp(z_2/z_1 - 1) > 1$. Since $z_1/z_0 > 1$ also, it follows that $z_{oc} < z_2$.

Equation (II.33) can be rewritten in the form

$$\frac{z_{oc}}{z_o} = \left(\frac{2\,l_{cw}}{z_o}\right)^{1 - |\vec{u}_{*c}|/|\vec{u}_{*cw}|} \left(\frac{z_2}{2\,l_{cw}}\right)^{-|\vec{u}_{*c}|/|\vec{u}_{*cw}|} \left[\frac{z_1}{2\,l_{cw}} \exp\left(\frac{z_2}{z_1} - 1\right)\right] \qquad \text{(II.34)}$$

Comparing (II.34) with equation (4.78) for z_{oc} and using the definitions (II.13) and (II.14) for z_1 and z_2, the continuous eddy viscosity profile introduces the correction factor

$$C_1 = \left(\frac{|\vec{u}_{*cw}|}{|\vec{u}_{*c}|}\right)^{1 - |\vec{u}_{*c}|/|\vec{u}_{*cw}|} \left(\frac{1}{4.8\ e^2}\right) \qquad \text{(II.35)}$$

into the original definition of z_{oc}. Taking the derivative of (II.35) with respect to $|\vec{u}_{*c}| / |\vec{u}_{*cw}|$, it is found that the greatest correction occurs when

$$\frac{|\vec{u}_{*c}|}{|\vec{u}_{*cw}|} = \frac{1}{\ln\,(4.8\ e^2)} \sim 0.28 \qquad \text{(II.36)}$$

Combining (II.35) and (II.36), the maximum correction is $C_1 = 0.27$. Since it is the logarithm of z_{oc} that appears in (II.32), the effect of this correction factor on the velocity profile is reduced significantly.

A.II.4 Solution for the wave

The Ekman layer model runs discussed in Section 5.2 show that the

Ekman layer velocity profile is relatively insensitive to order of magnitude changes in the eddy viscosity in the upper Ekman layer. While including the exponential decay factor in the neutral eddy viscosity increased velocities by about 10-20 percent, including the stratification correction in the upper Ekman layer changed the velocity profile by less than 10 percent. The main effect of stratification was to reduce the height of the Ekman layer. The stratification correction for this example was of order 10 near $z = z_m$ and of order 1000 near $z = l_c$. Because current velocity gradients are very small in the upper Ekman layer, even very large stability parameters have little effect on the current profile.

In the upper wave boundary layer ($z_2 < z < \delta_w$), maximum stratification corrections due to suspended sediment induced stratification from (4.47) are usually of order 0.1 to 1. Because current velocity and mean concentration gradients are large in this region, this stability parameter can have significant effects on the current and mean concentration profiles. Similar to the current velocity gradient in the upper Ekman layer, however, the wave velocity gradient is very small in the upper wave boundary layer. A stability parameter of order 1 therefore is expected to have very little effect on the wave velocity profile. The stratification correction may reduce the wave boundary layer height, but since the current velocity and mean concentration profiles no longer depend on the definition of the wave boundary layer height, this effect is insignificant. The suspended sediment stratification correction

therefore is neglected for simplicity in the solution for the wave.

The governing equation for the wave in the wave boundary layer is

$$\frac{\partial}{\partial z}\left(\frac{\nu_t}{\omega}\frac{\partial \vec{w}}{\partial z}\right) - i\vec{w} = 0 \tag{II.37}$$

where $\vec{w}$ is the velocity deficit defined as

$$\vec{w}\, e^{i\omega t} = \vec{u}_w - \vec{u}_b\, e^{i\omega t} \tag{II.38}$$

Defining the non-dimensional coordinate ζ as

$$\zeta = z/l_{cw} \tag{II.39}$$

z_o and the matching heights can be nondimensionlized as

$$\zeta_o = z_o/l_{cw}, \quad \zeta_1 = z_1/l_{cw}, \quad \text{and } \zeta_2 = z_2/l_{cw} \tag{II.40}$$

Using the eddy viscosity defined by (II.9), equation (II.37) for the wave in the lower region becomes

$$\frac{\partial}{\partial \zeta}\left(\zeta \frac{\partial \vec{w}}{\partial \zeta}\right) - i\vec{w} = 0 \qquad \zeta_o < \zeta < \zeta_1 \tag{II.41}$$

The solution to (II.41) is

$$\vec{w} = a\,(\mathrm{Ber}\ 2\zeta^{1/2} + i\,\mathrm{Bei}\ 2\zeta^{1/2}) + b\,(\mathrm{Ker}\ 2\zeta^{1/2} + i\,\mathrm{Kei}\ 2\zeta^{1/2}) \qquad \zeta_o < \zeta < \zeta_1 \tag{II.42}$$

Using (II.10), equation (II.37) for the wave in the central region becomes

$$\zeta_1 \frac{\partial^2 \vec{w}}{\partial \zeta^2} - i \vec{w} = 0 \qquad \zeta_1 < \zeta < \zeta_2 \tag{II.43}$$

The solution to (II.43) is

$$\vec{w} = c \exp\left[(1+i)\left(2\,\zeta_1^{-1/2}\right)\right] + d \exp\left[-(1+i)\left(2\,\zeta_1^{-1/2}\right)\right] \qquad \zeta_1 < \zeta < \zeta_2 \tag{II.44}$$

Using (II.11), equation (II.37) for the wave in the upper region becomes,

$$\frac{\partial}{\partial \zeta}\left(\frac{|\vec{u}_{*c}|}{|\vec{u}_{*cw}|}\,\zeta\,\frac{\partial \vec{w}}{\partial \zeta}\right) - i \vec{w} = 0 \qquad \zeta_2 < \zeta \tag{II.45}$$

Defining ξ as

$$\xi = \frac{|\vec{u}_{*cw}|}{|\vec{u}_{*c}|}\,\zeta \tag{II.46}$$

equation (II.45) can be written

$$\frac{\partial}{\partial \xi}\left(\xi \frac{\partial \vec{w}}{\partial \xi}\right) - i \vec{w} = 0 \qquad \zeta_2 < \zeta \tag{II.47}$$

The solution to (II.47) is

$$\vec{w} = g\left[\mathrm{Ber}\,2\left(\frac{|\vec{u}_{*cw}|}{|\vec{u}_{*c}|}\zeta\right)^{1/2} + i\,\mathrm{Bei}\,2\left(\frac{|\vec{u}_{*cw}|}{|\vec{u}_{*c}|}\zeta\right)^{1/2}\right] \tag{II.48}$$

$$+ f\left[\mathrm{Ker}\,2\left(\frac{|\vec{u}_{*cw}|}{|\vec{u}_{*c}|}\zeta\right)^{1/2} + i\,\mathrm{Kei}\,2\left(\frac{|\vec{u}_{*cw}|}{|\vec{u}_{*c}|}\zeta\right)^{1/2}\right] \qquad \zeta_2 < \zeta$$

The boundary conditions that must be applied to (II.42), (II.44) and (II.48) are the no slip condition at z_o

$$\vec{w} = \vec{w}_o = -\vec{u}_b \qquad \text{at} \quad \zeta = \zeta_o \tag{II.49}$$

that the velocity $(\vec{w})$ and the stress $(\partial\vec{w}/\partial z)$ are continuous at z_1 and z_2, and the velocity deficit goes to zero at the top of the wave boundary layer

$$\vec{w} \to 0 \qquad \text{as} \quad \zeta \to \infty \tag{II.50}$$

The final boundary condition (II.50) requires that g = o in (II.48). The remaining boundary conditions can be used to construct the following system of equations that must be solved for the 5 unknowns a, b, c, d, and f

$$\vec{w}_o = a\,B_o + b\,K_o \qquad \text{at } \zeta_o \tag{II.51}$$

$$a\,B_1 + b\,K_1 = c\,G_1 + d\,D_1 \qquad \text{at } \zeta_1 \tag{II.52}$$

$$a\,B'_1 + b\,K'_1 = c\,G'_1 + d\,D'_1 \qquad \text{at } \zeta_1 \qquad \text{(II.53)}$$

$$c\,G_2 + d\,D_2 = f\,Q_2 \qquad \text{at } \zeta_2 \qquad \text{(II.54)}$$

$$c\,G'_2 + d\,D'_2 = f\,Q'_2 \qquad \text{at } \zeta_2 \qquad \text{(II.55)}$$

where

$$B_o = \text{Ber } 2\,\zeta_o^{1/2} + i\,\text{Bei } 2\,\zeta_o^{1/2}$$

$$K_o = \text{Ker } 2\,\zeta_o^{1/2} + i\,\text{Kei } 2\,\zeta_o^{1/2}$$

$$B_1 = \text{Ber } 2\,\zeta_1^{1/2} + i\,\text{Bei } 2\,\zeta_1^{1/2} \qquad \text{(II.56)}$$

$$K_1 = \text{Ker } 2\,\zeta_1^{1/2} + i\,\text{Kei } 2\,\zeta_1^{1/2}$$

$$B'_1 = \zeta_1^{-1/2}\,(\text{Ber}'\ 2\,\zeta_1^{1/2} + i\,\text{Bei}'\ 2\,\zeta_1^{1/2})$$

$$K'_1 = \zeta_1^{-1/2}\,(\text{Ker}'\ 2\,\zeta_1^{1/2} + i\,\text{Kei}'\ 2\,\zeta_1^{1/2})$$

$$G_1 = \exp\left[(1+i)\,(2\,\zeta_1)^{-1/2}\,\zeta_1\right]$$

$$D_1 = \exp\left[-(1+i)\,(2\,\zeta_1)^{-1/2}\,\zeta_1\right]$$

$$G'_1 = (1+i)\,(2\,\zeta_1)^{-1/2}\exp\left[(1+i)\,(2\,\zeta_1)^{-1/2}\,\zeta_1\right]$$

$$D'_1 = -(1+i)\,(2\,\zeta_1)^{-1/2}\exp\left[-(1+i)\,(2\,\zeta_1)^{-1/2}\,\zeta_1\right]$$

$$G_2 = \exp\left[(1+i)\,(2\,\zeta_1)^{-1/2}\,\zeta_2\right]$$

$$D_2 = \exp\left[-(1+i)(2\zeta_1)^{-1/2}\zeta_2\right]$$

$$G'_2 = (1+i)(2\zeta_1^{-1/2})\exp\left[(1+i)(2\zeta_1)^{-1/2}\zeta_2\right]$$

$$D'_2 = -(1+i)(2\zeta_1^{-1/2})\exp\left[-(1+i)(2\zeta_1)^{-1/2}\zeta_2\right]$$

$$Q_2 = \mathrm{Ker}\ 2\left(\frac{|\vec{u}_{*cw}|}{|\vec{u}_{*c}|}\zeta_2\right)^{1/2} + i\,\mathrm{Kei}\ 2\left(\frac{|\vec{u}_{*cw}|}{|\vec{u}_{*c}|}\zeta_2\right)^{1/2}$$

$$Q'_2 = \left(\frac{|\vec{u}_{*cw}|}{|\vec{u}_{*c}|}\right)^{1/2}\zeta_2^{-1/2}\left[\mathrm{Ker}'\ 2\left(\frac{|\vec{u}_{*cw}|}{|\vec{u}_{*c}|}\zeta_2\right)^{1/2} + i\,\mathrm{Kei}'\ 2\left(\frac{|\vec{u}_{*cw}|}{|\vec{u}_{*c}|}\zeta_2\right)^{1/2}\right.$$

The solution procedure is to eliminate f from (II.54) and (II.55) to give an equation involving c and d. Equations (II.52) and (II.53) can be used to eliminate c and d to give an equation involving a and b only. Equation (II.51) then can be used to find a and b. The final solution to this system of equations is

$$a = \frac{\vec{w}_o\ T_b}{B_o T_b - K_o T_a} \tag{II.57}$$

$$b = \frac{\vec{w}_o\ T_a}{-B_o T_b + K_o T_a} \tag{II.58}$$

$$c = a \frac{(B_1 D'_1 - B'_1 D_1)}{(G_1 D'_1 - G'_1 D_1)} + b \frac{(K_1 D'_1 - K'_1 D_1)}{(G_1 D'_1 - G'_1 D_1)} \tag{II.59}$$

$$d = a \frac{(B_1 G'_1 - B'_1 G_1)}{(D_1 G'_1 - D'_1 G_1)} + b \frac{(K_1 G'_1 - K'_1 G_1)}{(D_1 G'_1 - D'_1 G_1)} \tag{II.60}$$

$$f = \frac{c}{2} \left(\frac{G_2}{Q_2} + \frac{G'_2}{Q'_2} \right) + \frac{d}{2} \left(\frac{D_2}{Q_2} + \frac{D'_2}{Q'_2} \right) \tag{II.61}$$

where

$$T_a = \frac{(B_1 D'_1 - B'_1 D_1)}{(G_1 D'_1 - G'_1 D_1)} \left(\frac{G_2}{Q_2} - \frac{G'_2}{Q'_2} \right) + \frac{(B_1 G'_1 - B'_1 G_1)}{(D_1 G'_1 - D'_1 G_1)} \left(\frac{D_2}{Q_2} - \frac{D'_2}{Q'_2} \right) \tag{II.62}$$

$$T_b = \frac{(K_1 D'_1 - K'_1 D_1)}{(G_1 D'_1 - G'_1 D_1)} \left(\frac{G_2}{Q_2} - \frac{G'_2}{Q'_2} \right) + \frac{(K_1 G'_1 - K'_1 G_1)}{(D_1 G'_1 - D'_1 G_1)} \left(\frac{D_2}{Q_2} - \frac{D'_2}{Q'_2} \right) \tag{II.63}$$

Solving (II.38) for u_w, the wave velocity in the wave boundary layer is given by

$$\vec{u}_w = (\vec{u}_b - \vec{w}) e^{i\omega t} \tag{II.64}$$

where $\vec{w}$ is given by (II.42), (II.44) or (II.48).

Using the small argument approximations to the Kelvin functions given by Abromowitz and Stegun (1972), (II.64) and (II.42) can be used to write the wave velocity for small ζ as

$$\vec{u}_w = [\vec{u}_b + a - \frac{b}{2}(\ln \zeta + 1.154 + i\frac{\pi}{2})] \tag{II.65}$$

The maximum shear stress associated with the enhanced wave is defined as

$$\frac{\vec{\tau}_{w,\,max}}{\rho} = \lim_{z \to 0} (\kappa |\vec{u}_{*cw}|\, z \frac{\partial \vec{u}_w}{\partial z})_{max} = \kappa |\vec{u}_{*cw}| (-\frac{b}{2} e^{i\omega t})_{max} \tag{II.66}$$

Substituting (II.58) for b gives

$$\frac{\vec{\tau}_{w,\,max}}{\rho} = \frac{\kappa |\vec{u}_{*cw}| \vec{u}_b \zeta_o^{1/2} |K_o|}{2 \zeta_o^{1/2} |K_o|} \left| \frac{T_a}{K_o T_a - B_o T_b} \right| \tag{II.67}$$

Comparing (II.67) with (3.47), the continuous eddy viscosity profile has introduced the correction factor

$$C_2 = |K_o| \left| \frac{T_a}{K_o T_a - B_o T_b} \right| \tag{II.68}$$

to the original definition of the maximum shear stress associated with the enhanced wave. The equation for the friction factor again is found using (3.49). Recalling the original definition of K given by (3.48)

$$K = \frac{1}{2 \zeta_o^{1/2} |K_o|} \tag{II.69}$$

the resulting equation for the friction factor is the same as (3.50)

with the new difinition of K

$$K = \frac{1}{2\,\zeta_o^{1/2}} \left| \frac{T_a}{K_o T_a - B_o T_b} \right| \tag{II.70}$$

A.II.5 Model comparison

The model developed here can be compared to the neutral near bottom model discussed in Chapter 3 to determine how sensitive the flow field is to the assumed eddy viscosity profile. Characteristic values for the input parameters will be chosen from typical CODE data. Assuming $|\vec{u}_b|$ = 10 cm/sec. A_b = 25 cm, z_r = 100 cm, $\overline{\phi}_c = 0°$, and k_b = 6 cm, the models can be run for a range of $|\vec{u}_r|$. This allows a comparison to be made for different values of $|\vec{u}_{*c}|/|\vec{u}_{*cw}|$. The model predictions of $|\vec{u}_{*c}|$ and z_{oc} are compared in Table A.1. The continuous eddy viscosity is found to reduce $|\vec{u}_{*c}|$ by about 10 to 25 percent while it reduces the apparent roughness z_{oc} by a factor of 2 to 3. Changes in the model parameters caused by the continuous eddy viscosity are greatest for weak currents and large waves.

Because the physical bottom roughness at the CODE site is unknown within a factor of 2 or possibly more, the linear eddy viscosity model was run with a factor of 2 decrease in k_b and the modified eddy viscosity model was run with a factor of 2 increase in k_b. From the model results listed in Table A.1, the same order of magnitude variation is observed in $|\vec{u}_{*c}|$ and z_{oc} for both models. Because values of $|\vec{u}_r|/|\vec{u}_b|$ for the CODE-I data are

TABLE A.I

$\lvert\vec{u}_r\rvert$ (cm/sec)	$\lvert\vec{u}_{*c}\rvert$ (cm/sec)				z_{oc} (cm)			
	Linear		Continuous		Linear		Continuous	
	$z_o = 0.2$	$z_o = 0.1$	$z_o = 0.4$	$z_o = 0.2$	$z_o = 0.2$	$z_o = 0.1$	$z_o = 0.4$	$z_o = 0.2$
30	2.35	2.10	2.26	2.06	0.601	0.330	0.498	0.296
25	2.01	1.80	2.07	1.74	0.691	0.386	0.806	0.322
20	1.67	1.49	1.64	1.51	0.823	0.470	0.762	0.503
15	1.31	1.18	1.21	1.12	1.03	0.610	0.697	0.477
10	0.938	0.844	0.791	0.738	1.04	0.875	0.638	0.443
5	0.522	0.475	0.407	0.380	2.17	1.48	0.735	0.520

Model Comparison:
Linear Eddy Viscosity versus Continuous Eddy Viscosity
Typical CODE-I data: $\lvert\vec{u}_b\rvert$ = 10 cm/sec, A_b = 25 cm,
z_r = 100 cm, $\phi_c = 0^\circ$, $\lvert\vec{u}_r\rvert$ and z_o allowed to vary.

generally greater than 1, model predictions for this data set are not very sensitive to which eddy viscosity profile is used. Uncertainties in the values of z_o and $C_{nm}(z_o)$ can cause the same order of magnitude changes in the velocity profiles as the corrections for a continuous eddy viscosity profile. The simpler linear eddy viscosity profile therefore was used for the model comparison in Chapter 6. It is not necessary to use the more complicated continuous profile until more confidence is gained in the physical bottom roughness and reference concentration models. After the models for z_o and $C_{nm}(z_o)$ have been tested in combined wave and current flows and improved, use of the continuous eddy viscosity profile may be warranted.

It should be noted that the assumed form for the continuous eddy viscosity used here was chosen by analogy with a pure wave eddy viscosity with maximum shear velocity $|\vec{u}_{*cw}|$ and a pure current eddy viscosity with shear velocity $|\vec{u}_{*c}|$. It was assumed that the turbulent momentum transport was controlled by the largest eddies, which are dominated by the enhanced wave for $z < z_2$ and by the enhanced current for $z > z_2$. The validity of this assumption remains to be confirmed by experimental evidence. The linear eddy viscosity profile used in Chapter 3 is most likely an overestimate of the actual eddy viscosity in the wave boundary layer. If the continuous eddy viscosity used here is found to be incorrect, it is most likely an underestimate of the actual eddy viscosity in the wave boundary layer. The actual eddy viscosity therefore is probably in the range defined by

the two forms used here. If a more realistic form for the continuous eddy viscosity is found in the future, it can easily be incorporated in the bottom boundary layer model as outlined in this Appendix.